CONTROL OF HIERARCHICAL NANOSTRUCTURES IN POLYMER

NANOCOMPOSITES VIA SCALABLE SPINNING AND SPRAYING PROCESESS

A Dissertation

Presented to the Faculty of the Graduate School

of Cornell University

In Partial Fulfillment of the Requirements for the Degree of

Doctor of Philosophy

by

Yevgen Zhmayev

May 2017

CONTROL OF HIERARCHICAL NANOSTRUCTURES IN POLYMER

NANOCOMPOSITES VIA SCALABLE SPINNING AND SPRAYING PROCESESS

Yevgen Zhmayev, Ph. D.

Cornell University 2017

Over the past several decades, polymer nanocomposites have been of increasing scientific and industrial interest due to their potential applications in filtration, energy storage, and biomedical engineering. Although the addition of various nanofillers makes them viable for high-tech applications, the control of spatial distribution and orientation of functional nanoinclusions remains a great challenge. There is a plethora of methods for nanoparticle surface modification to improve the enthalpic interaction between the polymer matrix and the filler, but often it results in deterioration of catalytic, magnetic and electrical properties of the composites. Therefore, it is desirable to develop a reliable and scalable method for the control of dispersion of nanoinclusions in polymer nanocomposites, without compromising their fundamental properties.

The work presented in this thesis aims to investigate the effect of additional extensional deformation provided by a sheath layer of controlled air flow during gas-assisted electrospinning (GAES) and air-controlled electrospray (ACES) on dispersion and spatial orientation of various nanoparticles in polymer matrix. Both spherical and anisotropic nanoparticles were employed in this study. First, we developed a robust post-process methodology to analyze transmission electron microscopy (TEM) images of microtomed longitudinal sections of nanoparticle-loaded PVA nanofibers, which provides a unique opportunity to investigate the details of the deformation-induced dispersion behavior. To demonstrate the material application perspective, we utilized

GAES in the fabrication of a fibrous silicon anode material for Li-ion batteries, and observed a significant enhancement in both capacity and activity of active nanoinclusions at the same composition, which is attributed to improved dispersion. Coarse-grained molecular dynamics study confirms these experimental observations.

We further extended our knowledge to conventional electrospray and novel air-controlled electrospray methods, to overcome the limitations due to non-uniform deposition and poor dispersion of fillers in functional coatings. Due to the precise control of atomization via extensional deformation and viscoelasticity, we successfully utilized new spraying processes for coatings with precisely controllable nanoscale topology, morphology, deposition thickness, and spatial distribution of unfunctionalized nanoinclusions. In order to demonstrate the industrial potential, we employed air-controlled electrospray for mass-production of micro/nano-scale encapsulates, and further fabrication of polymer composites with in situ indication of mechanical damage.

Finally, to overcome scalability constraints and ensure viability for industrial utilization, we investigated a novel centrifugal spinning process. The focus was on the experimental visualization of the fluid flow and examination of the effects of viscoelasticity, polymer flow rate and driving force on the initial thinning and the contour shaper and radii of the polymer jet. High-speed camera imaging was utilized to visualize the flow of viscoelastic Boger fluid during centrifugal spinning process, and experimental results including intital jetting behavior were compared with the simulation results predicted by the discretized modeling.

The current work provides an array of robust, economic and efficient single-step methods to fabricate hierarchical nanocomposites with controllable functionalities, topologies, morphologies, and spatial distribution of active nanoinclusions. The added benefit of experimental visualization and further comparison with computer simulation provides valuable insights and

more rigorous understanding of the process.  The successful advancement and utilization of these novel techniques will offer more comprehensive studies of nanocompsoites and lead to the next-generation functional materials.

BIOGRAPHICAL SKETCH

Yevgen Zhmayev was born on December 29, 1989, to Robert Dorfman and Nataliia Zhmaieva in Kyiv, Ukraine. In 2007, he graduated from the UNESCO associated specialized school # 211 in Kyiv and received a "gold medal" for scholastic achievements. Thanks to excellent guidance of his parents, from early childhood he was involved in a number of extracurricular activities, including basketball, martial arts, music (theory, violin, piano, and orchestra), English speech and debate, as well as academic Olympiads in sciences and arts. He has earned first places in the district Chemistry Olympiads, and participated in the Kyiv finals. In his senior year, he was awarded with a Diploma of Distinction from the mayor of Kyiv, for prominent academic, social and athletic achievements. He continued his studies in the Faculty of Chemical Technology of National Technical University of Ukraine "Igor Sikorsky Kyiv Polytechnic Institute", where he joined the Department of Chemical Technology of Ceramics and Glass in 2007. In 2011, he graduated with honors and received a Bachelor of Science degree in Chemical Technology. During his undergraduate studies, he became involved in various research projects, and in 2011 completed a military service with a rank of Junior Lieutenant of the Armed Forces of Ukraine. In the summer of 2010 he did a research internship at the School of Chemical and Biomolecular Engineering at Cornell University, working on enabling "green" cellulosic ethanol bio-fuel production via enzymatic and alkaline hydrolysis, under the supervision of Prof. Y. L. Joo. Excitement over this research led him to continue as a doctorate student in Joo Research Group at the Robert Frederick Smith School of Chemical and Biomolecular Engineering at Cornell University. He defended his Ph.D. thesis in January 2017, and is moving to Muenster, Germany, to join the Coatings Division of the BASF Group.

To my dear mother, Natasha, for giving me all the love in the world and for being my life example.

To my late father, Robert, for being a paragon of manliness and intelligence.

To my elder brother, Eddie, for being my role model and inspiration.

To Natasha, Eddie and all other family and friends, who are always there to fill my life with joy, love and happiness, to believe in me, to support my every decision and fulfill my dreams, and to provide help, optimism, and encouragement.

ACKNOWLEDGEMENTS

First and foremost, I would like to express gratitude to my thesis advisor, Prof. Yong L. Joo, for his support, motivation, help and exceptional mentorship throughout my Ph.D. work. His broad and deep knowledge, as well as his careful, creative and extraordinary approach to solve scientific problems were an inspiration. His professionalism, enthusiasm, perfectionism and devotion in both research and teaching were the main encouragement and catalyst in my Ph.D. research.

I would also like to acknowledge my committee members, Prof. Claude Cohen and Prof. Margaret Frey, for taking the time to discuss my research and for providing valuable advice, feedback, encouragement and constructive criticism. I also would like to thank other Chemical Engineering faculty for their contribution in teaching, research advice, and career planning. In particular, I would like to acknowledge Professors Hanrath, Stroock, Koch and Daniel for valuable suggestions and discussions about my research, and Prof. Louge for being my mentor and for helping me to develop my teaching skills while I was his teaching assistant.

I would like to thank the members of the Joo research group for their advice, help and constant support. Special acknowledgements to Ghazal Shoorideh, Shubham Pinge, Mounica Divvela and George Shebert for their valuable input to my research, and Jay Park for his experimental and theoretical expertise, as well as for the training that he provided. I would also like to thank my research assistants: Prabhleen Kaur, Hongshen Liu, Yi-Chen Chiang, Limin Li and Grace Lin, who have done a remarkable job, and helped me to develop my leadership skills. Glenn Swan has helped remarkably in the design and machining of various parts for spinning and spraying setups. Shelby Clark-Shevalier, Stephanie Palcich, Johanna Tuttle, Carol Casler, Celia

TABLE OF CONTENTS

LIST OF FIGURES

# LIST OF TABLES

**CHAPTER 1**

**INTRODUCTION**

## 1.1. Introduction

Polymeric composites are essential components of the modern technology due to their unique properties, therefore a wide range of products and applications that became a vital part of our daily routine. For instance, polymeric fibers with various active inclusions, are utilized in such areas as advanced electronics, catalysis, protective clothing, filtration, and biomedical engineering. However, traditional manufacturing schemes, such as mechanical drawing, preclude precise control of dimensions and productivity. [1–11] Likewise, functional polymer coatings are utilized in fabrication of superhydrophobic materials, biomedical devices, and energy storage media. [12–23] Their deposition via conventional methods suffers from poor control of surface topology, low deposition efficiency, as well as difficulty to cover large and complicated architectures. [15, 20] Finally, encapsulation technology has recently gained a lot of attention in mechanical damage indication, pharmaceutical, food and textile industries, where capsules can be utilized solely or incorporated in nanocomposites to provide functionality. Nevertheless, standard fabrication techniques require tedious multi-step synthesis procedures, and offer little control of dimensions and size distribution of fabricated capsules. [24–30] As a result, in recent years there was a lot of attention to development and refinement of alternative techniques that allow fabrication of high surface area to mass ratio submicron-sized fibers, capsules and efficient coating deposition.

Conventional electrospinning and electrospraying are the most auspicious techniques and received a lot of attention due to their attractiveness for industrial applications. In these processes, a charged polymeric jet or droplet is drawn by a strong electric field and fibers or films can be

1

collected on the grounded collector. Polymer electrospinning and electrospraying have been studied extensively in the past. However, the challenges associated with productivity, scalability and precise control of resulting composite dimensions, topology, morphology as well as deposition efficiency hindered the integration of these techniques in large-scale manufacturing. [2, 6, 10, 31] To overcome the foregoing challenges we have recently developed two novel processes that employ a circumferentially uniform air flow through the sheath layer of the concentric coaxial nozzle and utilize both high electric field and controlled air flow to effectively produce nanofibers, coatings and capsules. These techniques are referred to as gas-assisted electrospinning (GAES) and air-controlled (AC) electrospraying, respectively.

Novel air-controlled techniques presented in this thesis offer a ten-fold increase in production rate per spinneret, rigorous control of dimensions, topologies and morphologies of resulting nanocomposites, as well as a possibility to uniformly coat convoluted architectures, which makes them much more attractive and promising for industrial applications. In composite materials, individual constituents stay discrete within fabricated architecture, however the interaction between them enables modification and control of chemical and physical properties. With the application of additional extensional deformation through the sheath-layer air flow one can effectively control the placement and spatial distribution of various active nanoinclusions, which obviates both nanoparticle functionalization and multi-step process for desired nanocomposite fabrication. [11, 32–34] Such process optimization led to fabrication of Li-ion Battery anode with superior performance.

Gas-assisted electrospinning and air-controlled electrospraying can be scaled-up to a large manufacturing process by increasing the number and dimensions of spinnerets, which is not feasible for some applications. To overcome such scalability constraints and to ensure viability for

industrial utilization, we developed a novel centrifugal spinning process. In this technique, the centrifugal force is utilized to accelerate and elongate a fluid jet, increasing productivity hundredfold and decreasing the size of a setup. Empirical observations in conjunction with computer simulation methods were utilized to provide valuable insights into understanding the process, that may lead to further optimization.

## 1.2. The scope of the Investigated Problems

The work presented in this thesis describes the effect of circumferentially uniform sheath layer air flow, employed during gas-assisted electrospinning and air-controlled electrospraying processes, on the single-step fabrication of various hierarchical polymer nanostructures. The novel methodology was formulated based on the effect of extensional and shear deformations applied to polymer melts with nanoinclusions, theoretically investigated by Kalra and Park [11, 32–34]. However, significant modifications had to be made to account for various empirical process aspects and disparities between solutions and melts. In particular, careful deliberation was given to the continuity of the effect of assisting air flow, interplay between process parameters, and effect of material properties.

The detailed explanation and discussion of the novel methodology are provided in Chapter 2, where GAES technique was utilized to control the spatial distribution of unfunctionalized spherical $SiO_2$ and $Si$ nanoparticles (NPs) in polyvinyl alcohol (PVA) nanofibers. Our results demonstrate that the application of high but controlled air flow provided additional extensional deformation at the onset of fiber spinning, and therefore enhanced dispersion and orientation of various nanofillers. Resulting fibers were analyzed using transmission electron microscopy, and dispersion was quantified utilizing novel image analysis techniques. Our results revealed a

significant improvement in dispersion area and a substantial decrease in the most probable separation between individual particles, due to strain-induced rupture of NP-agglomerates. A rigorous time-scale analysis was performed to confirm that extension is a homogenizing force, and deformation-induced rupture mechanism dominates. Furthermore, a Li-ion battery anode was fabricated via scalable GAES, and superior performance was attributed to enhancement of spatial distribution of active nanoinclusions.

However, electrochemical performance depends on the synergistic effect of the accessibility of Si active sites, and effective charge/mass transport in the system. Carbon nanotubes (CNTs) and their unzipped counterparts – graphene nanoribbons (GNRs) were incorporated in the fibrous anode material to enhance battery performance and facilitate electron transport. Therefore, the control of spatial distribution and orientation of unfunctionalized anisotropic nanoinclusions is crucial, and the extension of our robust methodology is presented in Chapter 3. Our results confirmed that additional extensional deformation supplied by the sheath layer air flow during GAES enhances dispersion and alignment of 1-D nanofillers in resulting polymer fibers. It has been observed that CNTs require higher extensional deformations to disperse, compared to GNRs, which can be explained by increased stiffness and stronger cohesive forces. On the other hand, alignment analysis results show that CNTs easily orient along the fiber axis with the increase of the air flow, while GNRs undergo alignment worsening at higher elongation, potentially due to inhomogeneous response to deformation. All the results were qualitatively confirmed with a non-equilibrium coarse-grained molecular dynamics simulations, to reinforce the idea that tuning extensional deformation by using sheath layer air flow is an effective strategy to precisely control the placement and orientation of various nanofillers in polymer nanocomposites.

We further extended our knowledge to manufacturing of functional polymer coatings, where the control of surface topology, morphology, deposition efficiency, as well as dispersion of active nanoinclusions plays a crucial role. There is a myriad of methods that are currently being investigated, however conventional electrospraying technique received a lot of attention due to its controllability, facility and high deposition efficiency. However, significant challenges persist, especially in the efforts to increase productivity, tune nanoscale topology, control fluid atomization as well as dispersion and orientation of nanofillers in resulting coatings. In Chapter 4, we present a novel air-controlled electrospraying process, which is a powerful and efficient method to manufacture coatings with precisely controllable nanoscale topology, morphology, deposition thickness, and spatial distribution of unfunctionalized NPs. We demonstrated that the application of controlled air flow through coaxial spinneret can tune the atomization mechanism, therefore precisely control the size of ejected droplets, as well as homogeneity and efficiency of film deposition. A new methodology benefits from the synergistic effect of the droplet size reduction and strain-induced rupture of NP-agglomerates, leading to a significant improvement in spatial distribution of spherical and anisotropic NPs in deposited coatings. Furthermore, we developed a novel alternating current air-controlled ($AC^2$) electrospraying process, to ensure viability for industrial utilization and to alleviate the coating irregularity issues due to the surface-charge build-up on the substrate during direct-current (DC) electrospray.

Recently, conventional electrospraying gained a lot of attention in the fabrication of particles and micro/nano-encapsulation, due to its simplicity and robustness. However, due to some challenges associated with productivity, effective deposition and precise control of capsule dimensions it is rarely utilized for large-scale manufacturing. In Chapter 5, we utilized a new air-controlled electrospraying technique to resolve the foregoing issues, and to fabricate polymer

composites with in situ indication of mechanical damage. It has been demonstrated that capsule dimensions and morphologies can be precisely controlled by tuning the air flow rate and other process parameters. Further, air-controlled electrospraying was utilized to mass-produce nano-scale capsules, and in single-step effectively deposit them on the substrate, fabricating critical-stress sensing patches with highly distinct mechanochromic response.

Novel air-controlled spinning and spraying techniques, presented in this thesis, offer an order of magnitude increase in production rate, compared to their conventional counterparts, which is a significant enhancement for laboratory use and small-scale manufacturing. Additionally, they can be adequately scaled-up to a large-scale manufacturing process by increasing the number and dimensions of spinnerets. Nevertheless, such modifications can be inefficient, costly and impractical for some applications. In Chapter 6, we present a rigorous investigation of a novel centrifugal spinning technique that ensures economic viability and feasibility for industrial utilization. We focused on the experimental visualization of the fluid flow and examination of the effects of viscoelasticity, driving force and polymer flow rate, laying the foundation for future application of concentrated polymer solutions and melts. The experimental results were compared with the discretized element modeling, and confirmed predictive potential of the model that can potentially replace the traditional labor- and cost-intensive experimental trial-and-error techniques.

The novel fabrication techniques, as well as computational tools, presented in this thesis, provide a robust, economic and efficient single-step methodology to produce hierarchical nanocomposites with precisely controlled dimensions, topologies, morphologies, and spatial distribution of functional nanoinclusions. The successful development and utilization of these methods will revolutionize the field and lead to the next-generation functional materials.

## 1.3. Summary

In this chapter, we have provided some background information, motivation and formulation of the investigated problem. Our goal was to present a logical chain of empirical and theoretical research that was undertaken and presented in detail in the following chapters.

**REFERENCES**

[1]  A. Jaworek, A. Krupa, M. Lackowski, A. T. Sobczyk, T. Czech, S. Ramakrishna, S. Sundarrajan, and D. Pliszka, "Nanocomposite fabric formation by electrospinning and electrospraying technologies," *J. Electrostat.*, vol. 67, no. 2–3, pp. 435–438, 2009.

[2]  Z. M. Huang, Y. Z. Zhang, M. Kotaki, and S. Ramakrishna, "A review on polymer nanofibers by electrospinning and their applications in nanocomposites," *Compos. Sci. Technol.*, vol. 63, no. 15, pp. 2223–2253, 2003.

[3]  M. Bognitzki, T. Frese, M. Steinhart, A. Greiner, J. H. Wendorff, A. Schaper, and M. Hellwig, "Preparation of fibers with nanoscaled morphologies: electrospinning of polymer blends," *Polym. Eng. Sci.*, vol. 41, no. 6, pp. 982–989, 2001.

[4]  V. Thomas, X. Zhang, S. a Catledge, and Y. K. Vohra, "Functionally graded electrospun scaffolds with tunable mechanical properties for vascular tissue regeneration.," *Biomed. Mater.*, vol. 2, no. 4, pp. 224–32, 2007.

[5]  T. J. Sill and H. A. von Recum, "Electrospinning: Applications in drug delivery and tissue engineering," *Biomaterials*, vol. 29, no. 13, pp. 1989–2006, 2008.

[6]  E. Zhmayev, D. Cho, and Y. L. Joo, "Nanofibers from gas-assisted polymer melt electrospinning," *Polymer*, vol. 51, no. 18, pp. 4140–4144, Aug. 2010.

[7]  E. Zhmayev, D. Cho, and Y. Lak Joo, "Electrohydrodynamic quenching in polymer melt electrospinning," *Phys. Fluids*, vol. 23, no. 7, p. 73102, 2011.

[8]  E. Zhmayev, D. Cho, and Y. L. Joo, "Modeling of melt electrospinning for semi-crystalline polymers," *Polymer*, vol. 51, no. 1, pp. 274–290, Jan. 2010.

[9]  M. M. Hohman, M. Shin, G. Rutledge, and M. P. Brenner, "Electrospinning and electrically forced jets. II. Applications," *Phys. Fluids*, vol. 13, no. 8, pp. 2221–2236,

2001.

[10] Y. M. Shin, M. M. Hohman, M. P. Brenner, and G. C. Rutledge, "Experimental characterization of electrospinning: the electrically forced jet and instabilities," *Polymer*, vol. 42, no. 25, pp. 09955–09967, Dec. 2001.

[11] V. Kalra, J. Lee, J. H. Lee, S. G. Lee, M. Marquez, U. Wiesner, and Y. L. Joo, "Controlling nanoparticle location via confined assembly in electrospun block copolymer nanofibers," *Small*, vol. 4, no. 11, pp. 2067–2073, 2008.

[12] E. Burkarter, C. K. Saul, F. Thomazi, N. C. Cruz, L. S. Roman, and W. H. Schreiner, "Superhydrophobic electrosprayed PTFE," *Surf. Coatings Technol.*, vol. 202, no. 1, pp. 194–198, 2007.

[13] J. Bravo, L. Zhai, Z. Wu, R. E. Cohen, and M. F. Rubner, "Transparent superhydrophobic films based on silica nanoparticles," *Langmuir*, vol. 23, no. 28, pp. 7293–7298, 2007.

[14] S. T. Yohe and M. W. Grinstaff, "A facile approach to robust superhydrophobic 3D coatings via connective-particle formation using the electrospraying process.," *Chem. Commun.*, vol. 49, no. 8, pp. 804–6, 2013.

[15] Q. Guo, J. P. Mather, P. Yang, M. Boden, and P. T. Mather, "Fabrication of Polymeric Coatings with Controlled Microtopographies Using an Electrospraying Technique.," *PLoS One*, vol. 10, no. 6, pp. 1–14, 2015.

[16] L. T. De Jonge, S. C. G. Leeuwenburgh, J. J. J. P. Van Den Beucken, J. G. C. Wolke, and J. A. Jansen, "Electrosprayed enzyme coatings as bioinspired alternatives to bioceramic coatings for orthopedic and oral implants," *Adv. Funct. Mater.*, vol. 19, no. 5, pp. 755–762, 2009.

[17] M. Valvo, E. García-Tamayo, U. Lafont, and E. M. Kelder, "Direct synthesis and coating

of advanced nanocomposite negative electrodes for Li-ion batteries via electrospraying," *J. Power Sources*, vol. 196, no. 23, pp. 10191–10200, 2011.

[18] C. H. Chen, E. M. Kelder, M. J. G. Jak, and J. Schoonman, "Electrostatic spray deposition of thin layers of cathode materials for lithium battery," *Solid State Ionics*, vol. 86–88, no. 96, pp. 1301–1306, 1996.

[19] Y. Yu, J. L. Shui, Y. Jin, and C. H. Chen, "Electrochemical performance of nano-SiO2 modified LiCoO 2 thin films fabricated by electrostatic spray deposition (ESD)," *Electrochim. Acta*, vol. 51, no. 16, pp. 3292–3296, 2006.

[20] A. A. van Zomeren, E. M. Kelder, J. C. M. Marijnissen, and J. Schoonman, "The Production of Thin Films of LiMn2O4 by Electrospraying," *J. Aerosol Sci.*, vol. 25, no. 6, pp. 407–410, 1994.

[21] L. Wang, H. W. Xu, P. C. Chen, D. W. Zhang, C. X. Ding, and C. H. Chen, "Electrostatic spray deposition of porous Fe2O3 thin films as anode material with improved electrochemical performance for lithium-ion batteries," *J. Power Sources*, vol. 193, no. 2, pp. 846–850, 2009.

[22] Y. Yu, L. Gu, A. Dhanabalan, C. H. Chen, and C. Wang, "Three-dimensional porous amorphous SnO2 thin films as anodes for Li-ion batteries," *Electrochim. Acta*, vol. 54, no. 28, pp. 7227–7230, 2009.

[23] J. Schoonman and E. M. Kelder, "Thin film solid electrolytes and electrodes for rechargeable lithium-ion batteries," *J. Power Sources*, vol. 68, no. 1, pp. 65–68, 1997.

[24] B. Di Credico, G. Griffini, M. Levi, and S. Turri, "Microencapsulation of a UV-responsive photochromic dye by means of novel uv-screening polyurea-based shells for smart coating applications," *ACS Appl. Mater. Interfaces*, vol. 5, no. 14, pp. 6628–6634,

2013.

[25] S. A. Odom, A. C. Jackson, A. M. Prokup, S. Chayanupatkul, N. R. Sottos, S. R. White, and J. S. Moore, "Visual Indication of Mechanical Damage Using Core − Shell Microcapsules," *ACS Appl. Mater. Interfaces*, vol. 3, pp. 4547–4551, 2011.

[26] S. Vidinejevs, A. N. Aniskevich, A. Gregor, M. Sjoberg, and G. Alvarez, "Smart polymeric coatings for damage visualization in substrate materials," *J. Intell. Mater. Syst. Struct.*, vol. 23, no. 12, pp. 1371–1377, 2012.

[27] S. Gouin, "Microencapsulation: Industrial appraisal of existing technologies and trends," *Trends Food Sci. Technol.*, vol. 15, no. 7–8, pp. 330–347, 2004.

[28] I. G. Loscertales and A. M. Gañán-Calvo, "Micro / Nano Encapsulation via Electrified Coaxial Liquid Jets," *Science*, vol. 295, no. 2002, pp. 1695–1698, 2002.

[29] S. N. Rodrigues, I. Fernandes, I. M. Martins, V. G. Mata, F. Barreiro, and A. E. Rodrigues, "Microencapsulation of limonene for textile application," *Ind. Eng. Chem. Res.*, vol. 47, no. 12, pp. 4142–4147, 2008.

[30] S. Ghayempour and S. M. Mortazavi, "Fabrication of micro-nanocapsules by a new electrospraying method using coaxial jets and examination of effective parameters on their production," *J. Electrostat.*, vol. 71, no. 4, pp. 717–727, 2013.

[31] M. M. Hohman, M. Shin, G. Rutledge, and M. P. Brenner, "Electrospinning and electrically forced jets. II. Applications," *Phys. Fluids*, vol. 13, no. 8, p. 2221, 2001.

[32] J. H. Park, V. Kalra, and Y. L. Joo, "Controlling the dispersion and orientation of nanorods in polymer melt under shear: Coarse-grained molecular dynamics simulation study," *J. Chem. Phys.*, vol. 140, no. 12, p. 124903, 2014.

[33] V. Kalra, F. Escobedo, and Y. L. Joo, "Effect of shear on nanoparticle dispersion in

polymer melts: A coarse-grained molecular dynamics study," *J. Chem. Phys.*, vol. 132, no. 2, p. 24901, 2010.

[34]	V. Kalra and Y. L. Joo, "Coarse-grained molecular dynamics study of block copolymer/nanoparticle composites under elongational flow," *J. Chem. Phys.*, vol. 131, no. 21, 2009.

# CHAPTER 2

# CONTROLLING THE PLACEMENT OF SPHERICAL NANOPARTICLES IN ELECTRICALLY DRIVEN POLYMER JETS AND ITS APPLICATION TO LI-ION BATTERIES

## 2.1. Introduction

Dispersion of nanoparticles (NPs) in polymer matrices has a significant effect on intrinsic functionalities of advanced polymer nanocomposite materials, such as mechanical, optical, electrical and magnetic properties. [1] Such nanostructured materials have been studied for decades, however it is still challenging to obtain a homogeneous dispersion and avoid agglomeration of NPs. There is a plethora of methods for surface modification of NPs to increase the interaction between substrate and filler, but often it results in deterioration of catalytic, electrical, or magnetic properties. For instance, carbon nanotubes (CNTs) lose electrical conductivity after surface functionalization, due to disruption of $\pi$ conjugation. [2–5] Thus, the development of reliable methods for NP dispersion without tuning their fundamental properties remains a significant challenge.

In recent years there was a myriad of computational and experimental studies [2, 6–11], where mechanical stresses, such as shear or elongational flow, were applied to slow down or stop agglomeration of self-attracting NPs. For example, Kalra *et al.* [2, 9, 10] conducted a coarse-grained molecular dynamics study on the effect of shear and elongation on spherical nanoparticle placement in homopolymer and block-copolymer melts. It was shown that both shear and extension have a prominent effect on the assembly of selective NPs, which prefer one dispersion domain to another, and nonselective NPs. With the increase of elongational flow rate, the

concentration peak for both selective and nonselective NPs became much broader in the center of the corresponding dispersion domain, suggesting that extensional deformation can be used as a method to control dispersion and orientation of functional nanofillers. Mechanical deformation alters the kinetics of NP agglomeration, and can significantly increase the aggregation time scale via two mechanisms: first is the rupture of existing agglomerates due to shear, and second is the effect of deformation on the diffusion coefficient of nanoparticles. The rupture-like effect of shear or elongation is assumed to be positive and always leading to better dispersion, and is independent of the matrix chain length. Kalra and co-workers [2] conducted a rigorous analysis to compare time scales of diffusion ($t_{diff}$), shear ($t_{shear}$) and aggregation ($t_{agg}$) for self-attracting NPs in polymer melts. For the parameters used in their study, $t_{agg}$ was at least 1-2 orders of magnitude higher than $t_{diff}$ or $t_{\ hear}$. With the increase of deformation, both diffusion and shear time scales decrease, but at different rates. If $t_{diff} < t_{shear}$, then the diffusion is expected to be a homogenizing force and disperses NPs uniformly to eliminate concentration gradients. Accordingly, shear/deformation would homogenize the system via rupture-like mechanism at the time scales corresponding to shear rate ($t_{shear} < t_{diff}$).

Qualitatively similar predictions for dispersion of rod-like nanoparticles were reported by Park *et al.* [11, 12] It was observed that the dispersion and orientation of nanorods improved with increasing the shear, but it strongly depends on the size, rigidity and aspect ratio of nanofiller.

These works served as a starting point in understanding the effect of elongational deformation in electrospun nanocomposite fibers, which can form high performance materials that offer a large surface area and an open-pore structure. [13, 14] In the current study, we take a step forward and experimentally demonstrate an improved dispersion of monodisperse spherical $SiO_2$ and Si NPs in polyvinyl alcohol (PVA) nanofibers with the increase of strain imposed on the

polymer liquid during the fiber spinning process. We utilized two fiber-spinning processes, conventional electrospinning (ES) and gas-assisted electrospinning (GAES), and their schematics are depicted in Figure 2.1. Electrospinning is a well-known and versatile process that typically imposes a strong electric potential (~15-30 kV) on a polymer solution/melt that is ejected into the electric field. Once the electric charge on the liquid surface overcomes surface tension, a Taylor cone is formed and a thin polymer jet is emanated. The charged jet undergoes strong deformation (strain rate ~10,000 $s^{-1}$) imposed by electrically driven instability, and is subjected to fast solvent evaporation (~200 nL $s^{-1}$). After solidification has occurred, nano-scale fibers (50-500 nm) are deposited on the grounded collector as a non-woven mat. On the other hand, GAES utilizes circumferentially uniform air flow through the sheath layer of concentric coaxial nozzle in addition to the high electric field. [15–21] To demonstrate the ability to tailor NP dispersion in polymer jets, we produced nanofibers at different air flow rates (0, 2.5, 4, 5.5, 9 and 11 SCFH), at constant applied electric field (100 kV/m). A wide range of $SiO_2$ concentrations (1.85 - 12.98 vol. % to PVA) was used to probe the interplay between concentration and dispersion with and without additional air flow. We also employed Si NPs to examine the ability of extensional deformation to enhance dispersion of larger nanoparticles and to utilize their dispersion in energy storage applications. It has been previously shown that small selective NPs uniformly disperse in the favored domain to gain translational entropy. [10, 22] However, when the radius of NPs is commensurate to the radius of gyration of the polymer, the polymer chains can lose configurational entropy if they try to fold around the particle. As a result, chains push particles away, which may alter the dispersion pattern. [9, 23, 24] NPs are kinetically "trapped" in solidified polymer matrix, which makes it convenient for the quantitative post-process analysis. We took transmission electron microscopy (TEM) images of longitudinal sections of polymer nanofibers containing

various concentrations of NPs, which demonstrated improved distribution with the increase of the extensional force. Yazdanbakhsh *et al.* [25] summarized some dispersion quantification techniques, but none of them are universally used, and thus we devised our own characterization based on two image analysis methods for TEM images.

The first method calculates the area occupied by spherical NPs relative to the total area of the polymer nanocomposite on the 2D plane (TEM image), and referred to as dispersion area analysis (DAA). With the increase of the sheath layer airflow rate during GAES, extensional forces overcome cohesive forces between NPs and contribute to improved diffusivity [2, 3, 26–32], which leads to agglomerate rupture and enhanced nanofiller dispersion. Therefore, there is a significant improvement in the area occupied by NPs for higher extensional flow rates, which would be evident from TEM images and captured by the DAA. It should be noted that the volume occupied by NPs remains constant. The second quantification method is the Fast Fourier Transform analysis (FFT), which is utilized to determine the most probable separation distance between individual particles or agglomerates. Lower separation values resemble improved spatial distribution and enhanced agglomerate rupture. The concept of the most probable separation is similar to the pair correlation function, that is often used in coarse-grained molecular dynamics (CGMD) studies on NP dispersion, and describes how density varies as a function of distance from any reference particle. [2, 9–12]

However, from a materials application perspective, it is important to demonstrate that the proposed method for NP dispersion can be utilized in the production of novel materials, such as energy storage media. Spatial distribution of NPs is particularly important for electrode fabrication processes, since the capacity of material is usually normalized by the mass/volume of the active material. When particles aggregate, some of the surface area would be concealed, and thus there

will be some active material that does not participate in the electrochemical reaction, but is accounted for in the mass/volume normalization. Therefore, the resulting material will demonstrate low gravimetric/volumetric capacities. In this study, we utilized the strain-controlled dispersion of nanofillers in the production of fibrous silicon anode material for Li-ion batteries, and found that fibers produced via GAES show a substantial improvement in capacity and activity of functional inclusions compared to conventional ES. As-spun fibers by gas-assisted electrospinning have smaller aggregates of Si NPs and carbon nanotubes (CNTs) along the axial direction due to additional extensional force contributed by the air flow, and therefore provide a larger exposed surface area for lithium ion diffusion and electrochemical reactions. Finally, coarse-grained molecular dynamics results are presented to confirm the theoretical explanation of experimental observations in this study.
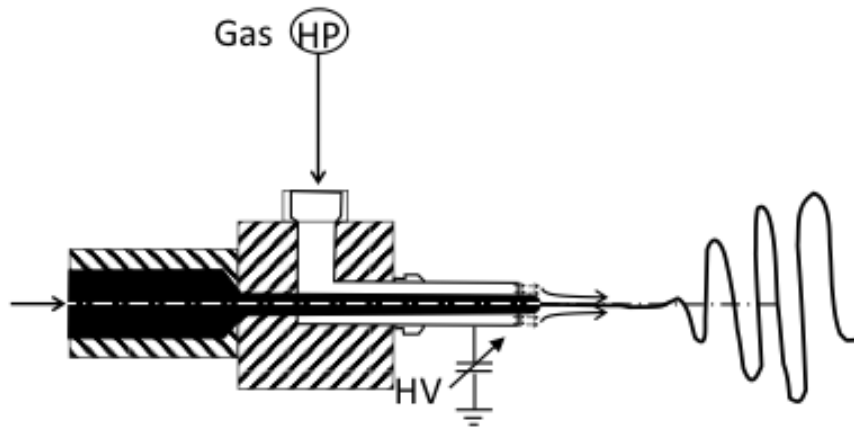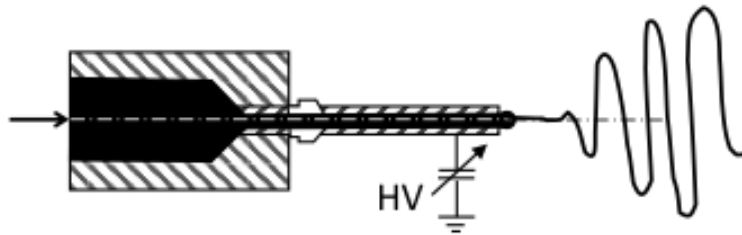
Figure 2.1. Gas-assisted electrospinning and conventional electrospinning schematics.

## 2.2. Experimental Section

*Materials:* 88 mole% Hydrolyzed Polyvinyl alcohol, with the Mw=78,000 g mol$^{-1}$ was used in this study and supplied by Polysciences, Inc. KLEBOSOL SiO$_2$ nanoparticles (12.5 nm in diameter) were provided by EMD and Si nanoparticles (82 nm in diameter) were supplied by MTI. Scanning electron microscopy and transmission electron microscopy studies were carried out to measure the average diameter of nanoinclusions.

*Nanofiber fabrication:* Nanofibers were produced by electrospinning and gas-assisted electrospinning at 2.5, 4, 5.5, 9 and 11 SCFH air flow, using a 10% PVA/water solution with different concentrations of $SiO_2$ (1.85-12.92 vol%) and Si at 6.86 vol% to PVA. The volumetric flow rates used for electrospinning and gas-assisted electrospinning were 0.003 ml $min^{-1}$ and 0.01 ml $min^{-1}$ respectively. The fibers were spun using applied electric field of 100 kV/m for both processes, and we refer the reader to our earlier publications for a more detailed overview of the experimental setup. [15, 33]

*Nanofiber characterization:* Nanofibers formed were characterized using scanning electron microscopy (Tescan Mira3 FESEM) and their diameters found to be in the range from 200 nm to 500 nm with $SiO_2$ NPs, and 400 nm to 900 nm with Si NPs. Fibers were left in the furnace at 150 $^o$C for 12 hours for crosslinking and then embedded in epoxy matrix and left at 60 $^o$C for two days. Fixed fiber mats were then microtomed into 70-nm thin sections at room temperature using a Leica Ultracut UCT. Ultrathin sections were stained in osmium tetroxide vapors overnight and were analyzed under a Tecnai T12 transmission electron microscope (TEM), which operated at 120 kV. TEM images were analyzed with MATLAB 2014R using image processing scripts developed in our laboratory.

*Dispersion area analysis:* In dispersion area analysis, gray-scale images are converted to binary and analyzed pixel-by-pixel to define nanofiber edges and NP agglomerates. The raw grayscale images generally have fibers with irregular geometries. Thus, they are divided into sub-images at the point of change in fiber orientation and subsequently aligned parallel to the horizontal axis, keeping the image quality intact. The next step involves the user selecting a region of interest to isolate the desired fiber. Consequently, another region is selected for the code to calculate the intensity threshold and convert the grayscale image to binary. The binary image is essentially an

array of ones (white region – polymer matrix) and zeroes (black region – background and nanofillers). For each column of the binary array, the difference between the maximum and minimum of the coordinates of ones gives the thickness of the fiber for that column. The integral of the fiber thickness along the length gives the total area of the fiber ($A_{fiber}$). The integral of the number of zeroes within the fiber boundary (nanofillers), along the fiber length provides the area occupied by the nanofillers ($A_{nf}$). The ratio of $A_{nf}/A_{fiber}$ gives the fractional dispersion area, an estimate of the extent to which nanofillers are dispersed. The method can be used under the assumption that on average the number of NPs per unit volume of polymer nanofiber is similar for the same nanofiller loading.

*Axial FFT analysis:* The binary image obtained from DAA is first normalized for its thickness. The process of normalizing the image can be thought of as either shrinking or stretching each of the columns in the binary array. In the process, it is ensured that the ratio and relative position of the ones and zeroes remain intact as in the original column. For each of the rows of the normalized image, the co-ordinates of the nanofillers are recorded and the Fourier transform of the data is obtained. The FFT gives the wavenumber and the amplitude corresponding to it. The wavenumber associated with the highest amplitude is considered to be predominant and the equivalent wavelength is the leading separation for that row along the fiber length. This exercise is repeated for all the rows along the radial direction and the prevalent separations are recorded. A probability distribution is then plotted for the recorded data. The separation distance corresponding to the highest probability is the most probable separation.

*Battery anode fabrication and characterization:* 0.5g of Polyvinyl alcohol (PVA, Polysciences, Mw~78,000) was dissolved in 5g of water, CNTs (7.57 vol% to PVA, Sigma) and Silicon NPs (51.1 vol% to PVA, MTI Co.) were added to the solution. A probe sonicator (Qsonica

Q500) was used to disperse the nanoparticles inside the solution. Then resultant solution was stirred for 5 hours before loading into a syringe. Water-based ES and GAES were used to spin a solution of PVA-Si-CNT fibers for lithium-ion battery anodes. The solutions were pumped at a rate of 0.008 ml/min and 0.01 ml/min for ES and GAES respectively. The fibers were spun using 15 kV voltage applied over 15 cm (measured from tip of the needle to collector). SEM (Tescan Mira3 FESEM) was used to examine fiber morphology. GAES and ES samples were used inside 2032 coin type half cells as anode, and lithium disk was used as the counter electrode. Areal loading of nanofibers on tested electrodes is 0.2-0.4 mg/cm$^2$. Half cell batteries were galvanostatically charged and discharged using a battery analyzing station (BST8-MA, MTI Co.) at different current rates in a voltage window of 0.015-1.5V vs Li/Li$^+$.

*Simulation Details*

9600 coarse-grained polymer and nanoparticle beads were simulated using molecular dynamics. Simulations were run starting from an isotropic state and continued until steady state was reached. Nanoparticle volume concentrations were chosen to be close to experimental values. To mimic the effects of electrospinning, planar elongation was applied to the simulation box. Although not identical to the uniaxial extension expected in electrospinning, planar elongation contains similar extension and compression and has the advantage of having a well-studied infinite time solution in MD.[34–36] The flow field was applied using the SLLOD equations of motion, which were integrated using a Velocity Verlet algorithm. [37] The code was validated by comparison with the results of Matin *et al.* [38]

Polymer chains of length 24 were bonded through a method of constraints used in Bruns *et al.* [39], which allows a larger integration time step by fixing the bond lengths. For polymer-polymer and polymer-nanoparticle interactions, the Weeks-Chandler-Anderson potential was used. [40] To

simulate the aggregation of nanoparticles, nanoparticle-nanoparticle interactions were modeled by a cut and shifted Lennard-Jones potential.

Normalized dispersion area was calculated by finding the $z$-$y$ projection of the nanoparticle positions, where extension occurred in the $z$ direction and compression in the $y$ direction. The normalized dispersion area was then found to be the area of the projection occupied by nanoparticle divided by the total area. Diffusion coefficients for nanoparticles in the polymer matrix were calculated by finding the mean squared displacement of nanoparticles in the $x$ dimension where no flow occurs. [2]

Table 2.1. Simulation parameters. Values in MD units are multiples of fundamental units of length, mass, and energy.

| Parameter | Value (MD units) |
|---|---|
| Temperature | 1 |
| Bead diameter | 1 |
| Chain length | 24 |
| Bead density | 0.85 |
| Number of beads | 9600 |
| MD integration time step | 0.005 |

**2.3. Results and Discussions**

*2.3.1.   The Dispersion Study of Silica Nanoparticles in PVA Nanofibers*

Figure 2.2 shows TEM images of longitudinal sections of PVA-SiO$_2$ nanofibers electrospun using different air flow rates through the sheath layer and a fixed electric field (100 kV/m). The particle surface is not functionalized, and therefore the spatial distribution is not affected by the improvement in affinity between dispersant and dispersion media. [13, 34] Silica nanoparticles are monodisperse (Figure 2.3 (a)), and kinetically trapped in the polymer matrix due to rapid solvent evaporation and fiber solidification, which allows us to access the state of the dispersion prior to complete agglomeration of nanoparticles. EDS analysis of a microtomed PVA/SiO$_2$ nanofiber was performed to confirm the chemical composition and is summarized in Figure 2.3 (b-d). SEM images of as-spun fiber mats were taken before and after temperature treatment (Figure 2.4) and there was no evidence of any changes in morphology. As can be seen from Figure 2.2, silica nanoparticles at 12.92 vol% concentration (black dots in TEM images) tend to form large agglomerates in PVA nanofibers spun using conventional electrospinning. However, with the application of a circumferentially uniform air flow, we can see a significant improvement in nanoparticle dispersion and agglomerate rupture.  Therefore, additional extensional deformation provided by air flow during GAES offers a better control over dispersion and orientation of individual nanoparticles and agglomerates. The similar behavior was observed for a wide spectrum of NP loadings, ranging from 1.85 to 12.98 vol% (with respect to PVA), and the TEM images for 1.85 vol% concentration are shown in Figure 2.5. As we demonstrate in a later section, materials with monodisperse placement of such nanoparticles can be very useful in fabrication of the energy storage media [42], [43] and water/oil repellant films. [44]
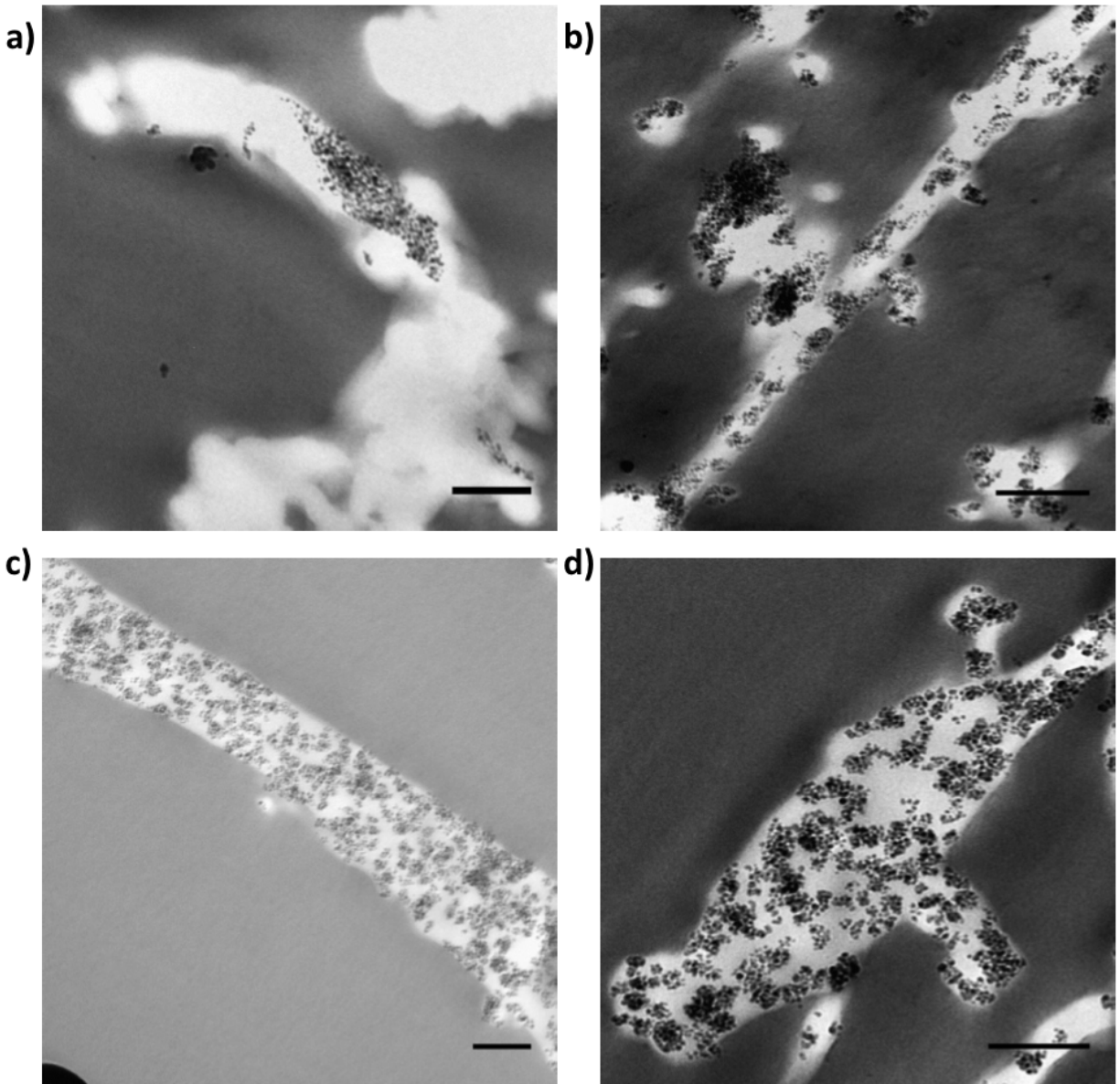
Figure 2.2. TEM images of microtomed PVA nanofibers with silica NPs (12.92 vol% to PVA) a) at 0 SCFH (conventional electrospinning), b) 5.5 SCFH, c) 9 SCFH and d) 11 SCFH air flow rate and 100 kV/m. Scale bar is 300 nm.
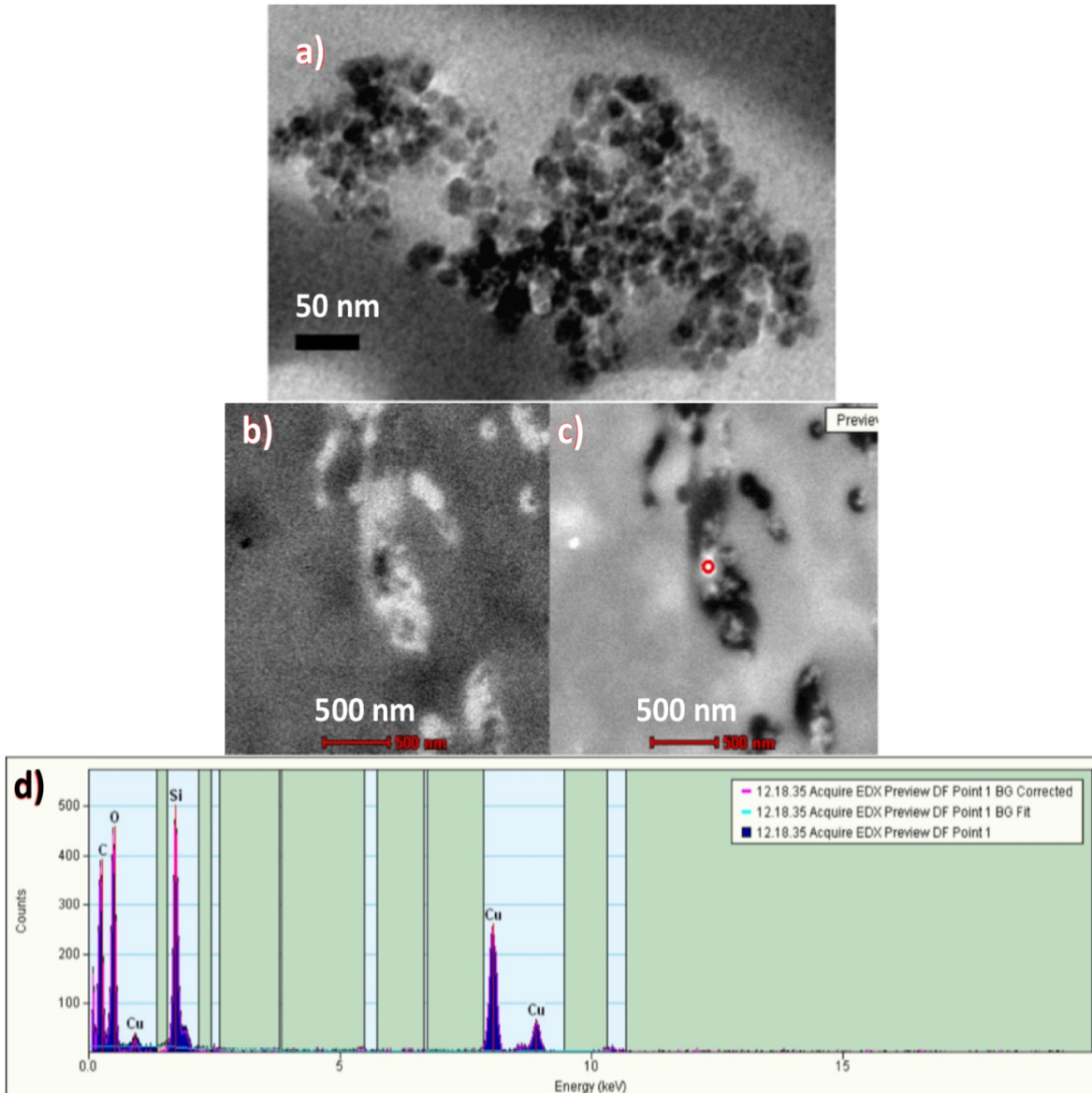
Figure 2.3 EDS analysis results of PVA fibers with silica NPs. a) TEM image of 12.5 nm monodisperse silica nanoparticles, b) TEM image (bright field) of  PVA nanofiber with 6.86 vol. % $SiO_2$ produced via ES, c) TEM image (dark field) of PVA nanofiber with 6.86 vol. %  $SiO_2$ produced via ES, d) EDS analysis spectra of a point on the NP agglomerate in PVA nanofiber with 6.86 vol. %  $SiO2$ produced via ES.
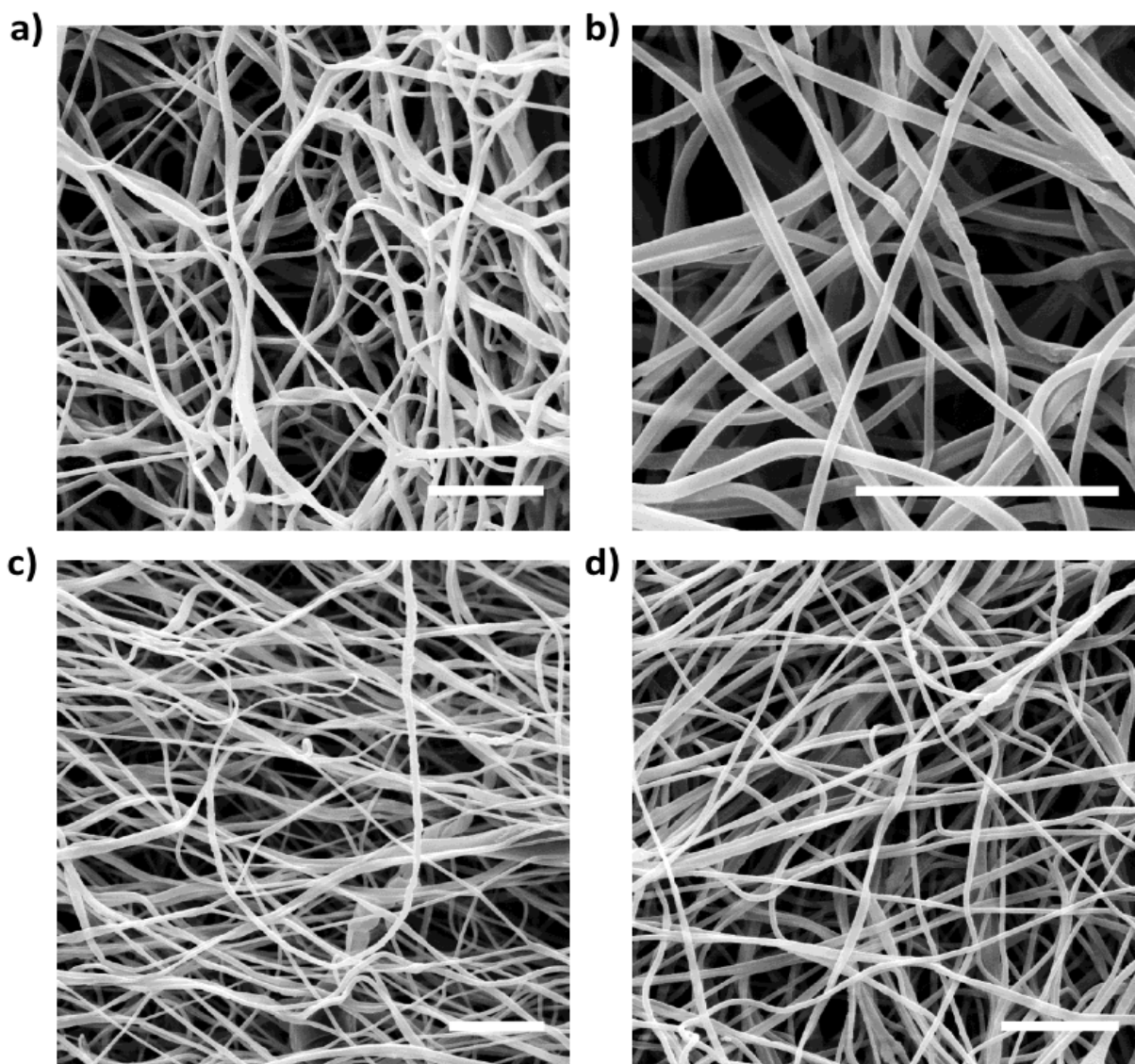
Figure 2.4. SEM images of PVA nanofibers with 6.86 vol. % SiO$_2$ spun at a) 0 SCFH – conventional ES, b) 5.5 SCFH, c) 9 SCFH and d) 11 SCFH GAES. The scale bar is 5 microns.
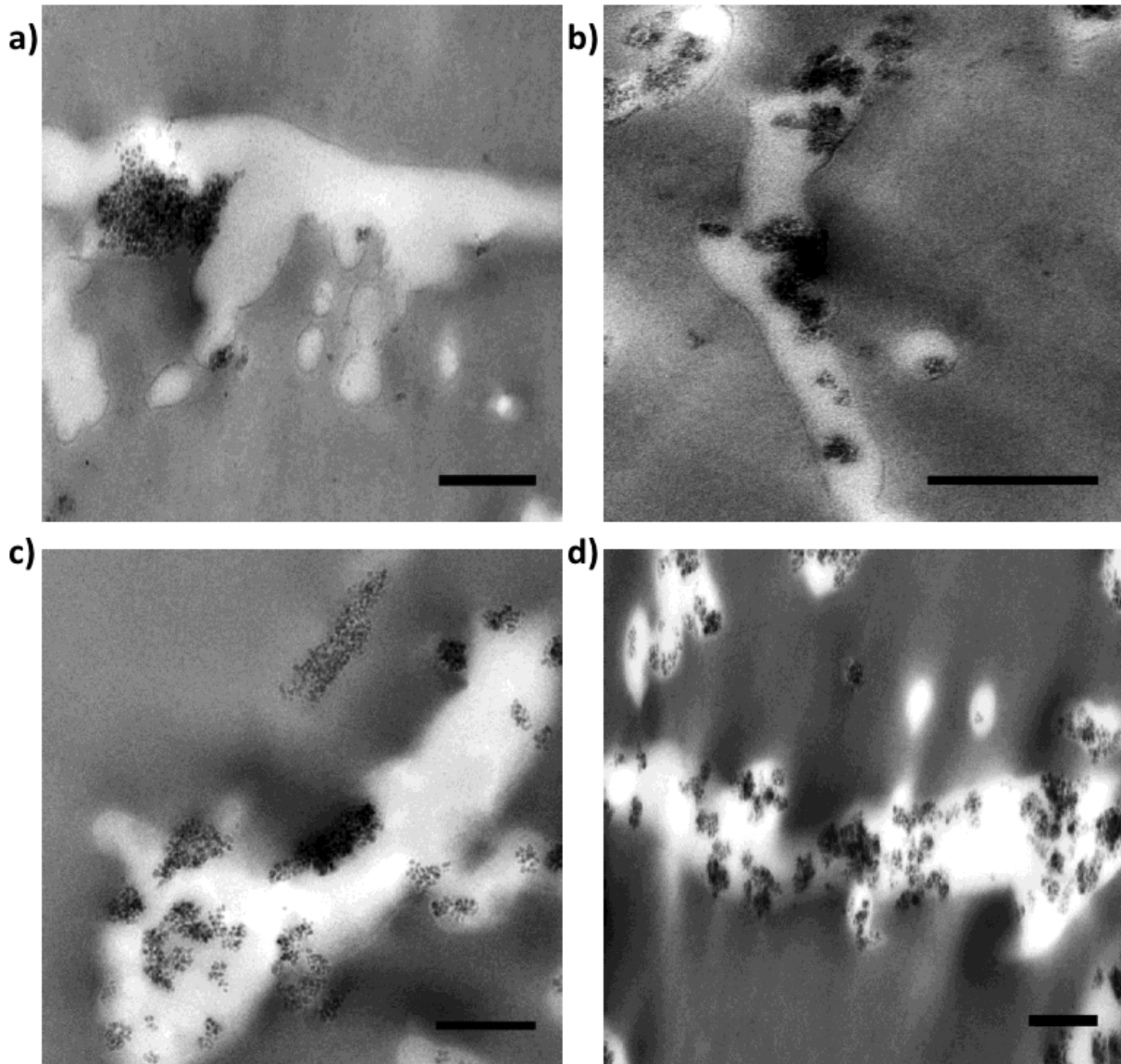
Figure 2.5. TEM images of longitudinal sections of microtomed PVA nanofibers with silica NPs (1.85 vol. % to PVA) a) at 0 SCFH (conventional electrospinning), b) 5.5 SCFH, c) 9 SCFH and d) 11 SCFH air flow rate and 100 kV/m. Scale bar is 300 nm.

In order to quantify the observed improvement in nanoparticle dispersion, we performed two types of post-process image analysis. The first technique is referred to as dispersion area analysis (DAA) which is based on determination of the area occupied by nanoincluisions relative to the total area of nanocomposite. DAA procedure is explained in more detail in the Experimental Section. Nanoparticles and particle agglomerates are expected to maximize the area of their contact with the polymer matrix to ensure the best and homogeneous dispersion, keeping the volume within the polymer matrix constant (Figure 2.6). Therefore, the ratio of the area occupied by NPs to the total area of nanocomposite should be approaching unity for the best dispersion. Figure 2.7 (a) shows the summary of DAA results for different NP loadings used in this study. It can be seen that for all NP concentrations, there is a significant improvement in the dispersion area with the application of the high air flow rate, and hence additional deformation. The effect of strong elongational flow was particularly prominent for the lowest (1.85 vol%) and the highest loadings (12.98 vol%), where dispersion area increased by almost 300 and 350% from conventional ES to the highest air flow rate GAES. To explain this behavior, we utilize the reasoning from earlier theoretical and computational works [2, 9–11], which speculate two main effects of strain/deformation on NP spatial distribution. The first effect corresponds to the deformation-induced rupture of NP agglomerates, and the second is due to the enhanced diffusion of NPs by extensional deformation. The rupture-like effect is observed when extensional forces overcome cohesive forces between self-attracting NP in agglomerates. It is expected to become more prominent with increasing deformation rate and is independent of the matrix chain length. However, the second effect requires a detailed analysis. It has been shown numerically and experimentally that with the application of high deformation, the diffusivity significantly increases for liquids [26, 27] and systems with particles suspended in liquids. [2, 28, 29]
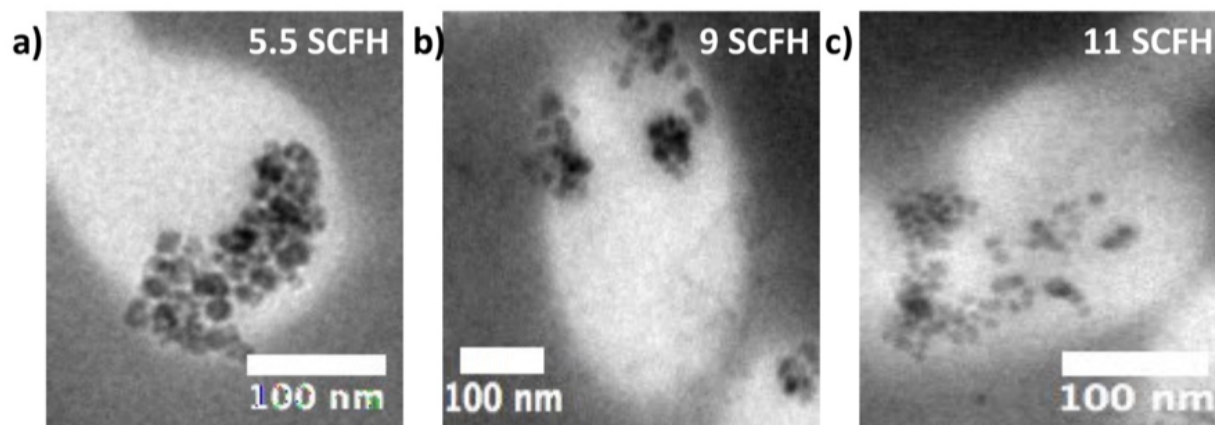
Figure 2.6. TEM images of cross-sections of microtomed PVA nanofibers with silica NPs (8.7 vol. % to PVA) a) at 5.5 SCFH, b) 9 SCFH and c) 11 SCFH air flow rate and 100 kV/m.

Brochard-Wyart and de Gennes reported that the friction experienced by a spherical colloidal particle in an entangled polymer melt would strictly depend on the size of the particle relative to the polymer tube diameter and radius of gyration. [38–40] If the particle radius is smaller than the characteristic length of the polymer chain and bigger than the polymer tube diameter, it falls in the thin viscosity regime, where it does not follow the Stokes-Einstein relation. This means that there is a significant drop in the local viscosity, due to the fact that the local friction depends only on the layer of monomers that are in contact with the particle, which makes the friction proportional to the NP area and independent of the polymer chain length. [41, 42] In both ES and GAES we start with a dilute polymer solution, but during rapid solvent evaporation and before complete solidification, the molten state is observed. Hence, we calculated two extreme cases to roughly estimate the range of polymer chain length scales. First, we calculated the radius of gyration of PVA which is equal to approximately 10 nm for PVA with Mw=78,000 g mol$^{-1}$, which is higher than the radius of SiO$_2$ NPs. Second, knowing that due to a very strong deformation during electrospinning process (as high as 10,000 s$^{-1}$), polymer chains tend to extend and align in the flow direction, and the maximum end-to-end distance for fully extended PVA chain is equal

to 400 nm. Having these values, we can conclude that the characteristic length of the polymer chain lies in the range from 10 to 400 nm and is significantly bigger than the radius of SiO$_2$ particle ($b = 6.25$ nm), which implies that NPs used in current study fall in the thin viscosity regime predicted by de Gennes *et al.* [45] However, it is clear from the TEM images that there are few cases where SiO$_2$ NPs are well dispersed and it is fair to assume that most of the agglomerates were formed prior to or in the nascent stage of fiber formation. Therefore, agglomerates must be treated as spheroidal clusters or hairy particles, which allows us to use Stokes-Einstein relation for the diffusivity. [45] Mobile chains will entangle with the "hairs" of the cluster during the flow and drastically reduce slippage. Consequently, the effective hydrodynamic radius ($R + b$) is very large, and there will be no or negligible improvement in diffusivity due to a decrease in the local viscosity. This effect is more pronounced for higher NP loadings, where there is a higher probability of forming agglomerates at the initial stage. Thus, the improvement in diffusivity is associated with the strain-enhanced diffusion, which would be a homogenizing force for NPs in short chain polymer matrix or when chains are perfectly aligned with the flow.

On the other hand, for long polymer chains, as in the current study and most of industrial applications, deformation or strain-induced rupture would be a homogenizing force. This can be verified by performing a simple time scale analysis. We define the diffusion time scale ($t_{diff}$) as $\sim b^2/D$, and the deformation time scale ($t_{strain}$) as $\sim 1/\dot{\gamma}$, where $D$ is the diffusivity of NP, and $\dot{\gamma}$ is the strain imposed on the polymer fluid by elongation. [2] The value of $D$ was calculated using Stokes-Einstein relation, and $\dot{\gamma}$ was assumed to be 10,000 s$^{-1}$. It has been calculated that for SiO$_2$ NPs in PVA solution $t_{diff}/t_{strain} = Pe \sim 6.7$, where $Pe$ is a Peclet number, which is a ratio of the rate of convection to the rate of diffusion. For this reason, it can be concluded that strain/extension is expected to be a rupture-like positive force and homogenize the location of NPs

in nanofibers. Similar results were observed in a rigorous time scale analysis performed by Kalra *et al*. [2]

It should be noted that the effect of the nanofiller loading is negligible for low concentrations. However, when high packing is approached, elongational deformation must be significantly higher to ensure good dispersion. This behavior can be observed from the 12.98 vol% case, where dispersion area for conventional electrospinning is lower than for 6.86 and 8.7 vol% concentrations at the same conditions (Figure 2.7 (a)), which is associated with increased viscosity of PVA solution at higher nanofiller loadings.
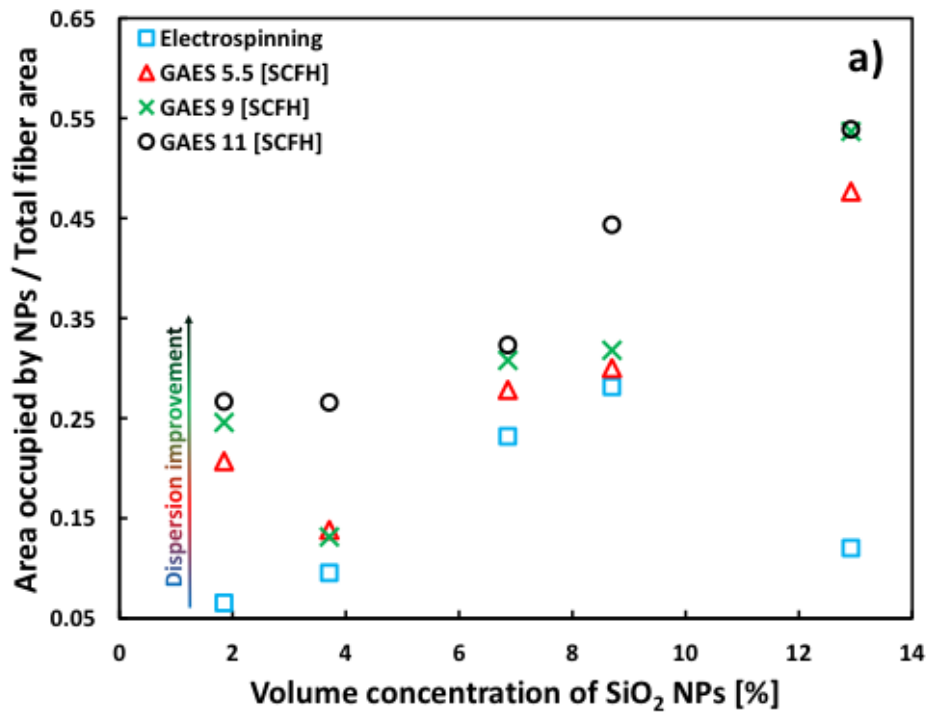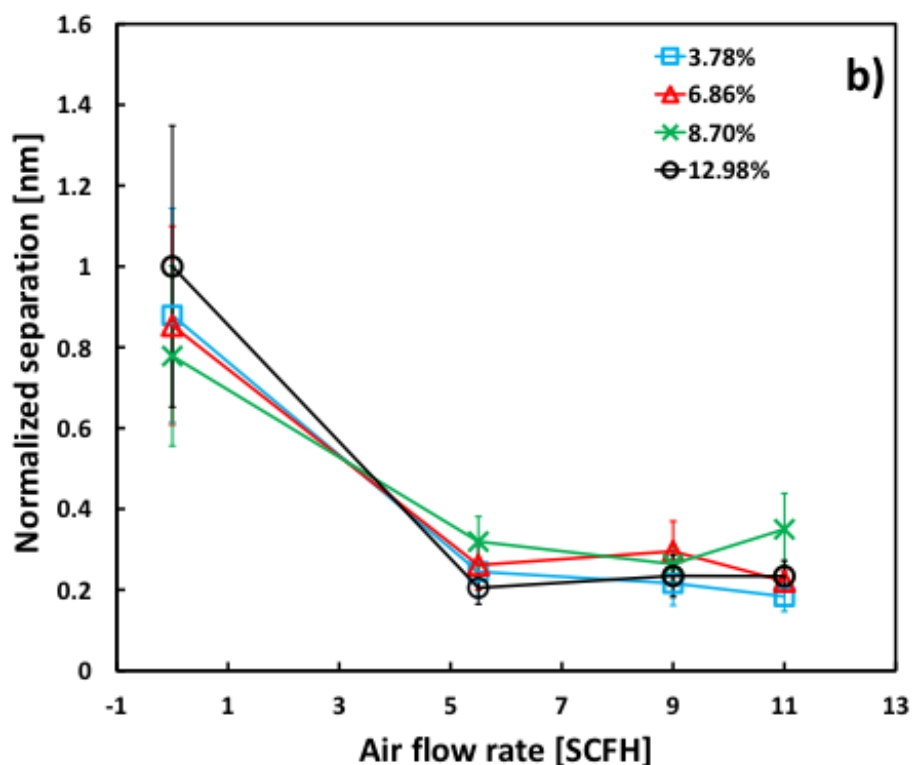
Figure 2.7. TEM image analysis results for electrospinning and gas-assisted electrospinning at different air flow rates of PVA/SiO$_2$ solutions with different SiO$_2$ nanoparticle loadings. A) Dispersion area analysis results. B) FFT results for separation between NPs and NP agglomerates.

Figure 2.7 (b) shows the results obtained from the axial Fast Fourier Transform analysis (FFT), which is summarized in more details in the Experimental Section. FFT analysis is utilized in the current study to determine the most probable separation between individual NPs and NP agglomerates in the flow direction. It is observed that for all concentrations used in the current study, there is an average of 75% decrease in separation with the application of the controlled sheath layer air flow. Lower separation values indicate improved dispersion of spherical NPs and enhanced cluster rupture. The concept of the most probable separation is similar to the pair

correlation function that describes how density varies as a function of distance from any reference particle and is often utilized in CGMD studies. [2, 9–12]

It should be noted that the most significant drop in separation was from conventional ES to the low air flow rate GAES (5.5 SCFH), suggesting that even slow circumferentially-assisting air flow can create a significant amount of strain, leading to better dispersion. Therefore, we investigated the effect of two lower air flow rates (2.5 and 4 SCFH) for two concentrations of silica NPs (6.86 and 12.98 vol%) to capture the transition that indicates a drastic dispersion enhancement. It can be seen from Figure 2.8 that there are two empirically evident regimes for the most probable separation and dispersion area due to additional deformation, which indicate a competition and a sudden change from one dispersion-enhancement mechanism to another.

To further analyze this behavior, we estimated the increase of extensional deformation by analyzing SEM images (Figure 2.4) for conventional ES and GAES at the same electric field (100 kV/m), and found that the final fiber dimensions did not show a noticeable change. However, the polymer-feeding rate for GAES was 3.34 times higher than for ES. This means that the total extensional deformation required for GAES to produce fibers of the same final dimensions has to be at least 3.34 times higher compared to ES.  If the strain rate for GAES is higher, the jet velocity is also higher compared to conventional ES. We speculate that the controlled sheath layer air flow provides additional shearing and extension at the initial stage of jet emanation. However, the effect is less pronounced in later stages of spinning once the fiber dimensions are small and jet velocity is higher than the velocity of air, that gradually dissipates at a distance from the spinneret. [50] Additional air flow assists collection of nanofibers in later stages of spinning and weakly contributes to additional acceleration and deformation.

To investigate two dispersion regimes that are evident from Figure 2.8 we conducted a time scale analysis to relate deformation and diffusion rates of the fiber spinning initiation ($Pe_0$) using previously mentioned definitions. First, it is required to calculate the initial strain rate ($\dot{\gamma}_0^{ES/GAES}$) that polymer solution experiences at the tip of the spinneret during ES or GAES at different air flow rates. This value is calculated for conventional electrospinning using Equation 2.1:

$$\dot{\gamma}_0^{ES} = u_0^{jet}/r_0 \tag{2.1}$$

where $u_0$ is the initial velocity and $r_0$ is the initial jet radius. However, for GAES it is important to account for additional initial stress associated with the sheath layer air flow ($\tau_0^{air}$) at different velocities:

$$\tau_0^{air} = \frac{u_0^{air}-u_0^{jet}}{|u_0^{air}-u_0^{jet}|}\left\{\frac{1}{2}\beta\rho_{air}^{0.39}\mu_{air}^{0.61}r_0^{-0.61}\left(\left|u_0^{air}-u_0^{jet}\right|\right)^{1.39}\right\} \tag{2.2}$$

where $\beta$ is the drag coupling parameter on a moving spinline and is equal to 0.185, $\rho_{air}$ is the air density and $\mu_{air}$ is the air viscosity. [15] Having initial stress due to air we used Equation 2.3 to calculate the initial strain rate for GAES at different air flow rates:

$$\dot{\gamma}_0^{GAES} = \dot{\gamma}_0^{ES} + \frac{\tau_0^{air}}{\mu_0} \tag{2.3}$$

where $\mu_0$ is the fluid viscosity, which was obtained from rheometry of PVA solutions with different NP loadings. Creeping flow assumption can be applied for the initial stage of fiber spinning process, which allows using the Stokes-Einstein relation for the calculation of diffusion coefficient. This quantitative analysis allows us to compute the time scales and obtain the relation between the initial convective and diffusive rates of $SiO_2$ NP dispersion, employing a correction factor that comes from a length scale difference between diffusion and convection.

It can be seen from Figure 2.8 that diffusion-enhanced dispersion is a leading mechanism at the initial stage of conventional ES ($Pe_0 = 0.2$). After addition of the sheath layer air flow, the deformation-enhanced dispersion mechanism starts competing with the diffusion-controlled one ($0.2 < Pe_0 < 6.77$), resulting in a slow improvement of NP spatial distribution, which can be seen during the first regime. It was empirically observed that at an intermediate air flow rate (5.5 SCFH) there is an apparent increase in the dispersion area and a sharp decrease of the most probable separation. Thus, the second dispersion regime ($Pe_0 > 6.77$) is the results of domination of the convective rate, responsible for the deformation-induced rupture mechanism.

It is worthy to note that our observations from DAA and FFT match computational predictions suggested by previous work [10–12], and further corroborate that application of controlled circumferentially uniform air flow in GAES results in better dispersion of nanoinclusions due to a strain enhanced agglomerate rupture and slightly from Taylor diffusion. This work provides a simple but powerful methodology to produce multifunctional nanocomposites with high surface area, where particle surface functionalization is not required. This would be particularly useful for catalytic and energy storage applications where particle surface functionalization may lead to loss of inherent material properties. Successful development of methods that control the placement and orientation of various nanofillers during fabrication of functional nanocomposites will revolutionize the field and lead to the next-generation functional materials.
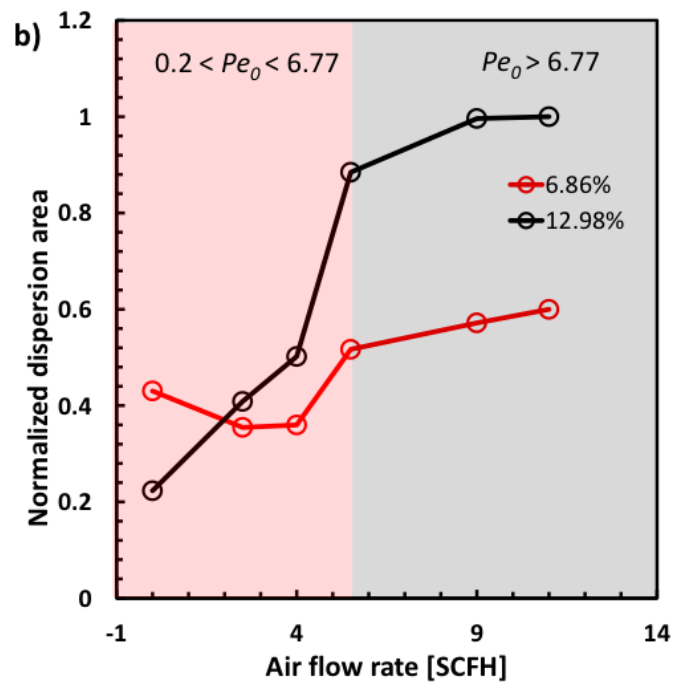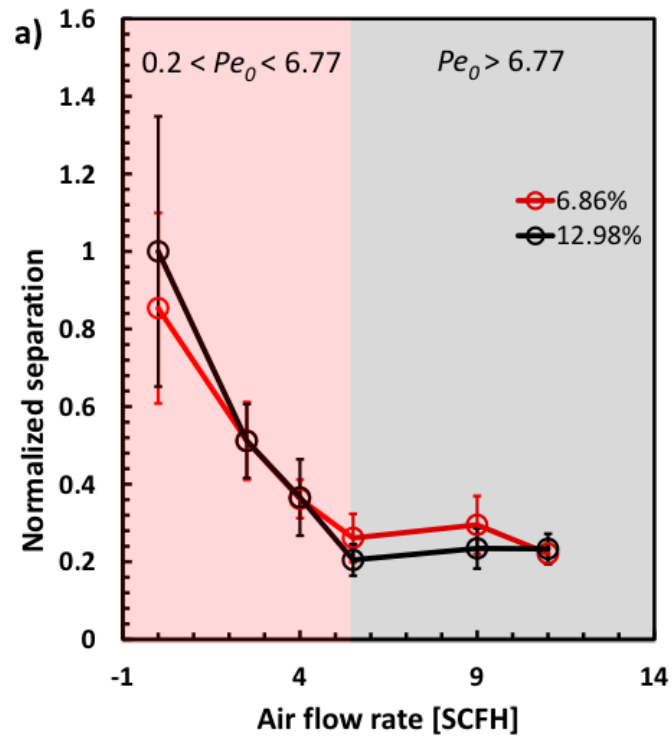
Figure 2.8. Dispersion regime analysis results from a) FFT and b) DAA of ES and GAES (2.5, 4, 5.5, 9, 11

SCFH) at the initial stage of spinning for PVA/SiO$_2$ (6.86 and 12.98 vol%) solutions.

*2.3.2. The Dispersion Study of Silicon Nanoparticles in PVA Nanofibers*

Figure 2.9 shows TEM images of longitudinal sections of PVA fibers with 6.86 vol% concentration of Si NPs. This concentration was utilized to observe the effect of elongational deformation on spatial distribution, and avoid any effects associated with nanofiller loading. It can be seen from the images that with the application and later increase of the air flow rate (and hence extensional force) in GAES, there is a slight improvement in nanoparticle dispersion and agglomerate rupture. We conjecture that the strong deformation owing to the application of controlled and circumferentially uniform air flow prevents agglomeration of individual Si NPs and ruptures existing agglomerates. Strain-induced agglomerate rupture mechanism is expected to be a homogenizing force, due to the large size of Si nanoparticles. Diffusivity will be significantly reduced, compared to small silica particles, and is expected to follow a conventional Stokes-Einstein relation with no/minor fluctuations in local viscosity. [45] Our time scale analysis reveals that $t_{diff}$ is more than 3 orders of magnitude higher than $t_{strain}$ $(t_{diff}/t_{strain} = 1650)$, confirming that extension is a homogenizing force and controls the spatial distribution of Si nanoparticles. It is important to note that the deformation time scale significantly dominates for the larger particles.

These observations were quantified using DAA and FFT analysis techniques. Figure 2.10 (a) shows that the dispersion area increased by more than 100% with the application of the high air flow rate. This result is associated with an intense rupture of spheroid-like Si agglomerates, and therefore significantly improved spatial distribution of NPs. Axial FFT analysis (Figure 2.10 (b)) shows a 35% decrease in the most probable separation between Si NPs (better dispersion) with the application of GAES. However, it can be seen that further increase in the air flow rate did not significantly affect the most probable separation, only the range of values.

Using the same reasoning and quantitative analysis as in the previous section we calculated the initial Peclet numbers ($Pe_0$) for conventional ES and GAES at different air flow rates for Si NP dispersion. It can be seen from Table S1 that there is almost an order of magnitude difference between $Pe_0^{SiO_2}$ and $Pe_0^{Si}$ due to a bigger size and therefore slower kinetics of Si particle dispersion. Thus, it can be concluded that a significant increase in extensional deformation is required to disperse large self-attracting Si particles in polymer nanofibers, and GAES proved to be a powerful and reliable method to improve and control Si spatial distribution. This work provides a robust single-step methodology to fabricate a lithium-ion battery anode with improved capacity due to enhanced dispersion of functional material, which is discussed in more details in the next section.
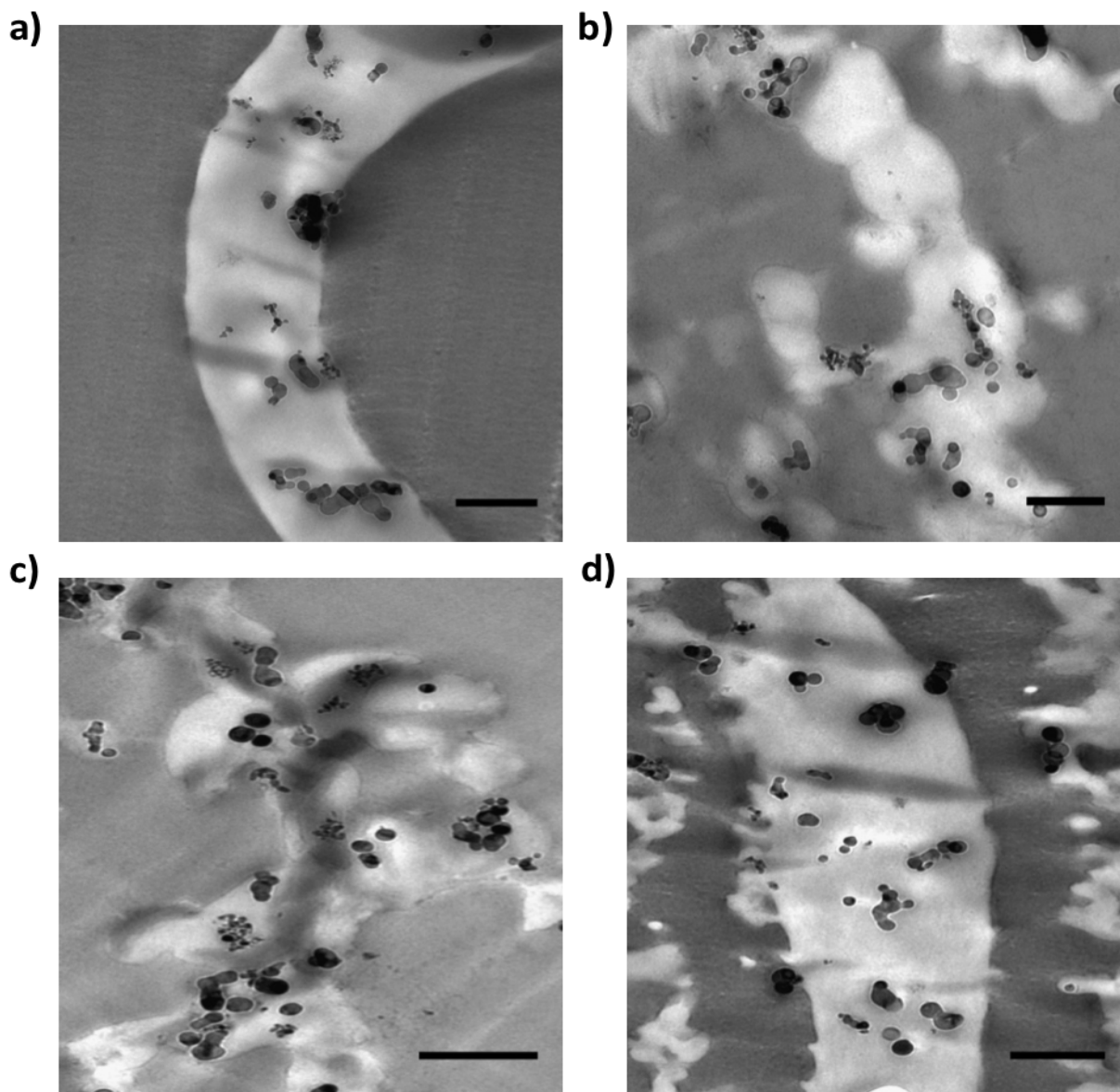
Figure 2.9. TEM images of microtomed PVA nanofibers with silicon NPs (6.86 vol% to PVA) a) at 0 SCFH (conventional electrospinning), b) 5.5 SCFH, c) 9 SCFH and d) 11 SCFH air flow rate and 100 kV/m. Scale bar is 500 nm.
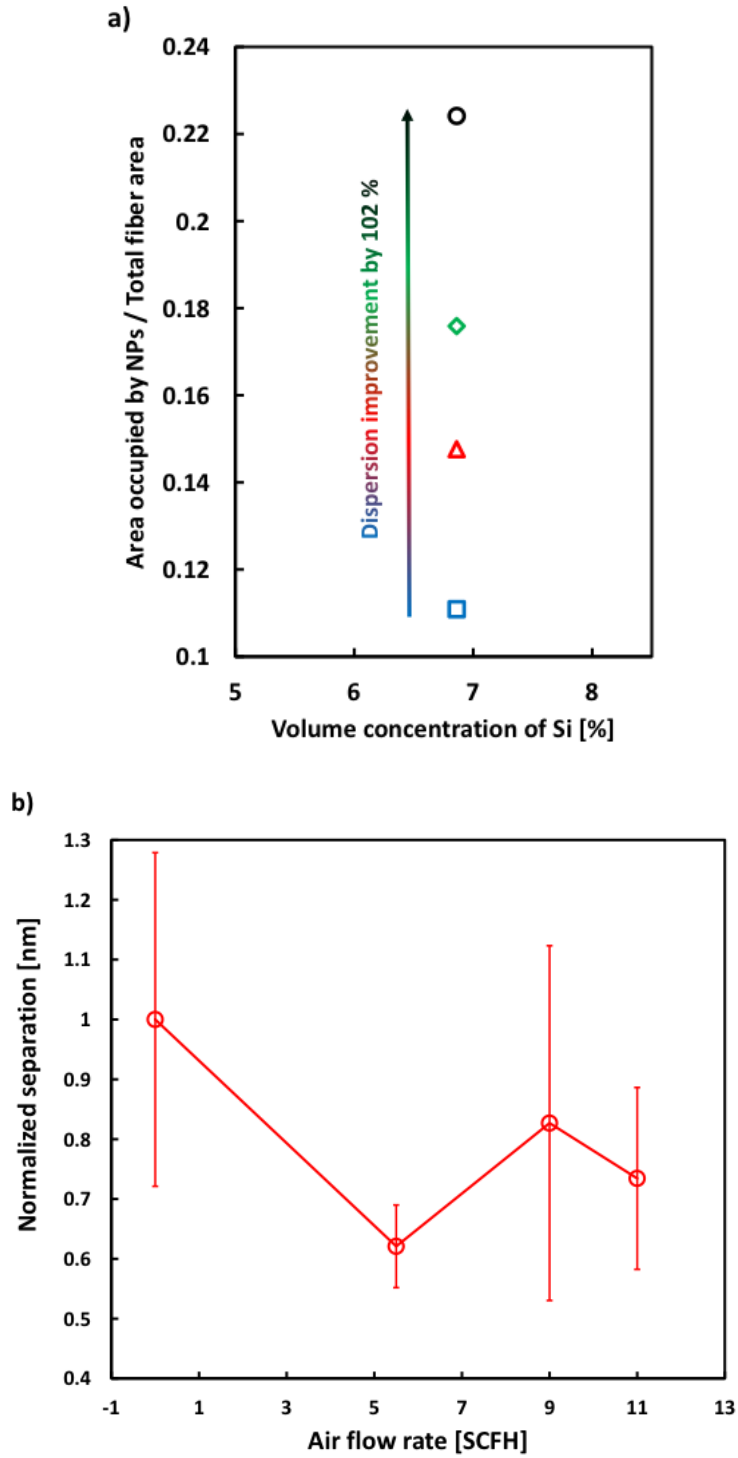
Figure 2.10. TEM image analysis results for electrospinning and gas-assisted electrospinning at different air flow rates of PVA solution with Si NPs (6.86 vol% to PVA) a) Dispersion area analysis results and b) FFT analysis results.

*2.3.3. Improved control over nanofiller dispersion in Li-ion battery anode fabrication*

Silicon, as the material with highest gravimetric capacity has been investigated as the anode for lithium-ion batteries for more than a decade now. The main issue preventing silicon anodes from becoming a viable commercial product is the dramatic volume change (400%) upon lithiation/delithiation. [35, 36] This usually results in pulverization and loss of electric contact of active material with the current collector and eventual capacity fading. Employment of nanoparticles has been proven to be a valuable strategy in alleviation of volume changes and improvement of device longevity [44–47], however, control over the nanofiller dispersion remains a significant challenge. Surface functionalization of nanoparticles is one of the strategies employed by different groups to improve nanoparticle dispersion [48, 49], and electrochemical performance of the created material. Nonetheless, surface functionalization can interfere with some of the inherent particle properties. To investigate the efficacy of GAES system in promotion of particle dispersion of particles without surface modifiers, this technique was applied to a highly loaded solution of PVA, CNTs and Si NPs. Figure 2.11 shows SEM images of PVA-Si-CNT fibers spun via ES and GAES.  Fibers that were spun via conventional ES possess larger aggregates of silicon nanoparticles, while GAES fibers have a more uniform dispersion. This improvement in spatial placement is a result of additional extensional force provided by the sheath layer air flow, as mentioned in previous sections. It should be noted that fiber mats for this experiment were spun simultaneously from the same solution via ES and GAES. Therefore, the only difference between two samples is the utilization of circumferentially uniform air flow in GAES. CNT is a new addition to the system, which may affect the spatial distribution of spherical Si NPs in the polymer matrix, and will be discussed in detail in the following chapter. Generally, the enthalpic interaction

41

between inorganic nano-inclusions and organic dispersion media is very low. However, if the second inorganic inclusion is added (CNTs in our case), it can act as a "dispersant", due to a better enthalpic interaction between inorganic components. [57] It can be concluded that the addition of CNTs may positively affect the dispersion of spherical NPs and improve electronic and thermal properties of the resulting nanocomposite.

To elucidate the role of NP dispersion in electrochemical performance of the samples, half cell batteries were fabricated using ES and GAES fibers and then galvanostatically charged and discharged at rates of 0.2 A/g and 1 A/g. Figure 2.12 (a) illustrates the life cycle of half cells at 0.2 A/g for 100 cycles. GAES fibers start off with higher capacity and show more than 600 mAh/g improvement in the capacity over the life of the battery, which is the direct result of better NP dispersion. GAES fibers depicted a capacity retention of 75% (calculated against the 2nd cycle), while ES fibers only retained 39% after 100 cycles at 0.2 A/g. First charge/discharge profiles of fibers at 0.18 A/g are plotted in Figure 2.12 (b). It is worthy to note that GAES fibers start at capacities higher than the theoretical capacity of silicon (4200 mAh/g). Part of this high initial capacity is due to the irreversible reactions of the electrolyte with particles and PVA template to form the solid electrolyte interface (SEI). Also, CNTs are electrochemically active and have been tested as successful anode materials on their own. They can have capacities as high as 2500 mAh/g on their first cycle. [51, 52] All the capacities in this paper are normalized by the mass of silicon inside of fibers. The shoulder at about 1.2 V [53, 54] is the indication of CNT electrochemical activity, and the plateau at 0.2-0.015 V is attributed to silicon activity. [55–57] Electrodes fabricated with the material spun via GAES show higher capacity and more Si and CNT activity, which is attributed to lower NP agglomeration that was observed from SEM images (Figure 2.11). GAES fibers get around 1500 mAh/g of their initial capacity from CNTs and SEI formation,

whereas for ES sample it is only about 1100 mAh/g. This improvement is the result of better CNT dispersion, therefore more accessible surface area for electrochemical reactions. GAES nanofibers also have better performance at fast rate of 1 A/g as is apparent from Figure 2.12 (c). The improvement in capacity for GAES sample over ES is about 680 mAh/g. This amount is almost twice the theoretical capacity of commercial graphite anodes (372 mAh/g) [58, 59], which is a significant gain at a low cost of additional gas flow. At this rate both electrodes retained 57% of their capacity after 100 cycles. More extensive tests on benefits of gas-assisted electrospinning in silicon anode fabrication and the overall configuration and geometry of composite fibers are currently underway. Versatility of this method is not limited to semiconductor materials. It can also be used with a variety of metallic organometallics with different geometries. GAES is a facile and economical method for a single step electrode fabrication, not only for lithium-ion batteries, but also for any energy storage devices, since better particle dispersion is easily achieved.
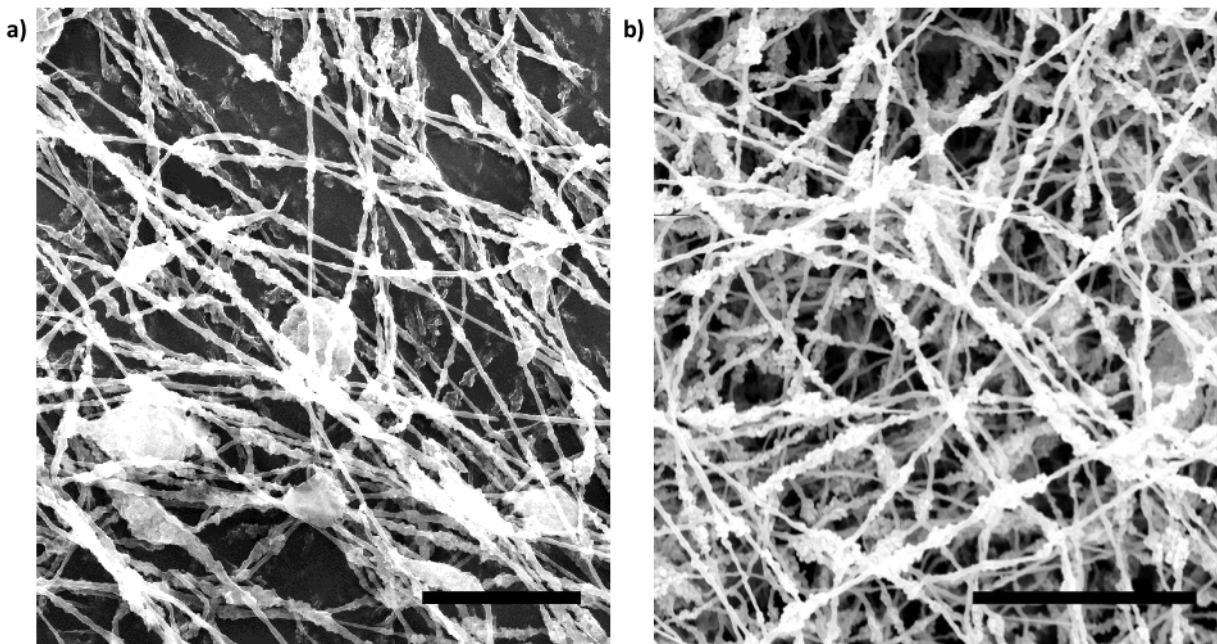
Figure 2.11. SEM images of PVA-Si-CNT fibers for Li-ion battery anode material spun via a) electrospinning and b) gas assisted electrospinning. Scale bar is 5 microns.
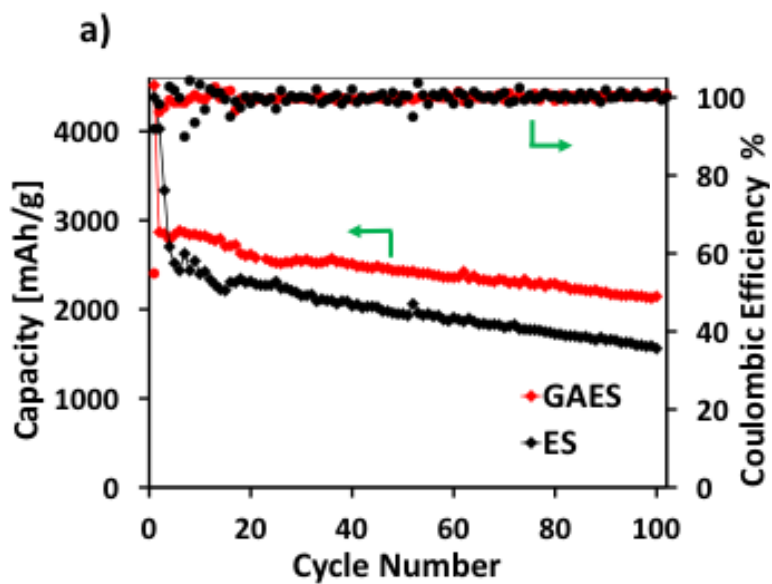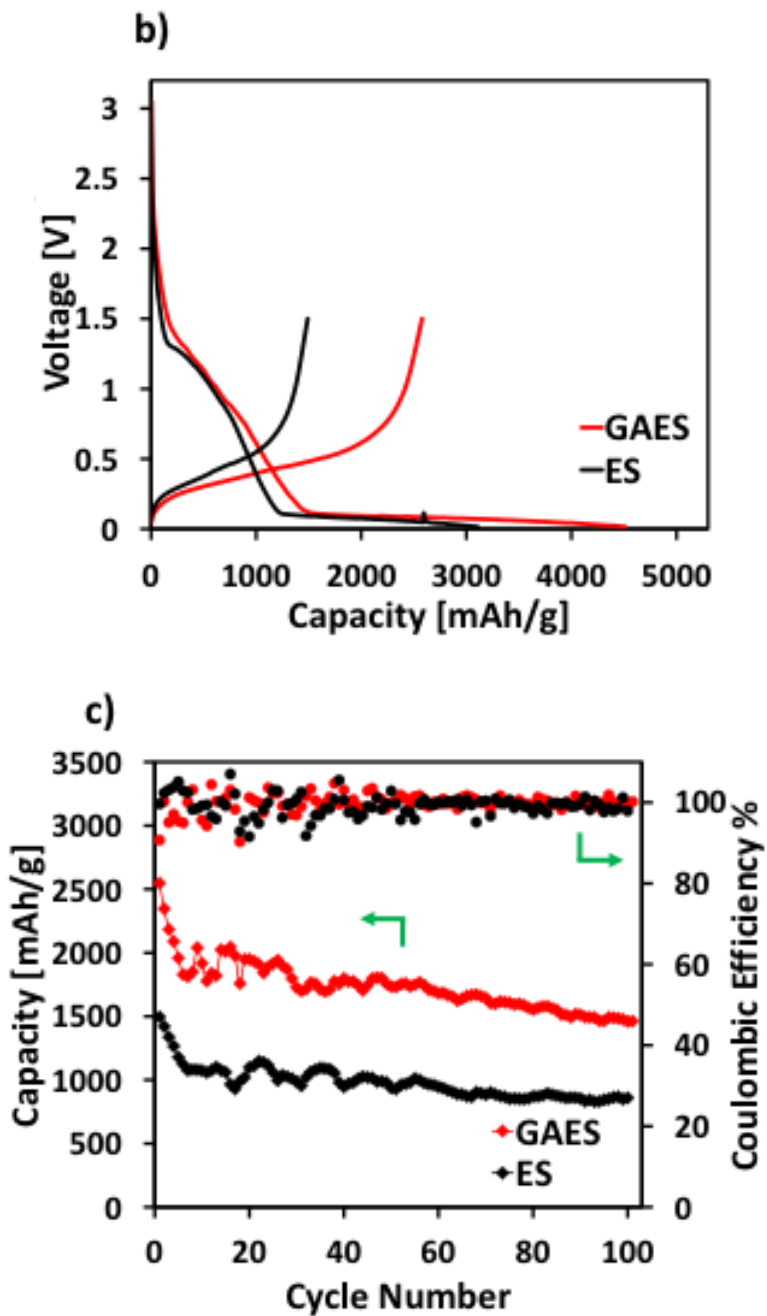
Figure 2.12. Electrochemical performance of anodes prepared via electrospinning and gas-assisted electrospinning. a) Cyclic performance and coulombic efficiencies of anode half cells at 0.2 A/g, b) First charge/discharge profiles of anode half cells at 0.18 A/g, c) Cyclic performance and coulombic efficiencies of anode half cells at 1A/g.

*2.3.4. Experimental validation with non-equilibrium coarse-grained molecular dynamics*

Non-equilibrium coarse-grained molecular dynamics simulations were performed to provide comparison to the experimental results. Simulation details are summarized in the Supporting Information. Figure 2.13 (a) shows snapshots of the simulation for different planar elongational strain rates and concentrations.

At lower rates, elongational strain induces the alignment of the polymer chains towards the extensional flow direction, which in turn causes the nanoparticles to form elongated clusters. At higher rates, the clusters disperse while still maintaining a general organization towards the extensional direction. So, it can be seen that the nanoparticle dispersion is improved at higher elongation rates. This effect is quantified in Figure 2.13 (b). Although these simulations are a simplified representation of experiment, the dispersion area results match the trends observed in experiment (Figure 2.7 (a)), where higher strain rate and higher concentration correspond to larger dispersion area. In Figure 2.13 (c), higher strain rates show reduced peaks of the pair correlation function. This indicates further that higher elongation strain rates result in better nanoparticle dispersion. These simulation results agree qualitatively with experimental electrospinning results, reinforcing that increasing extensional strain by using gas-assisted electrospinning is an effective strategy for improving nanoparticle dispersion.
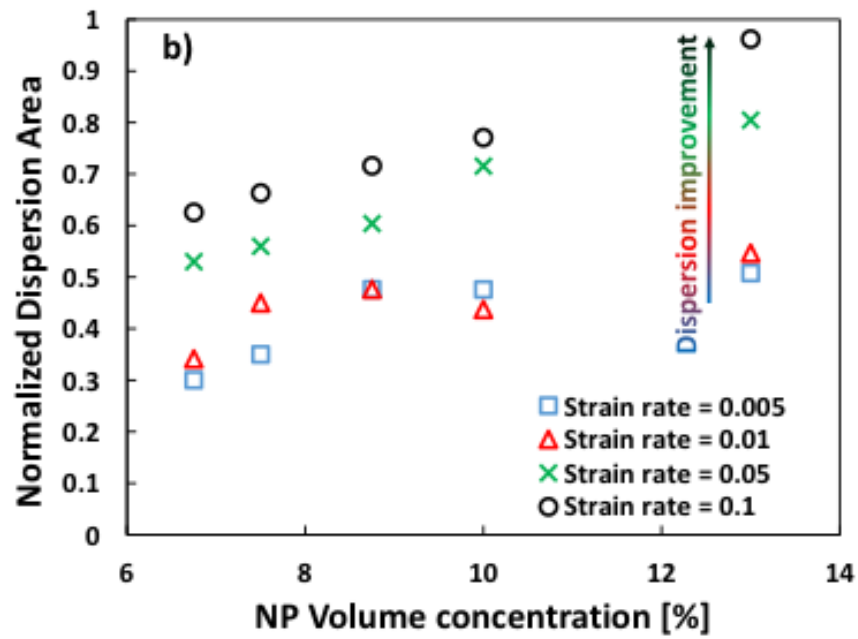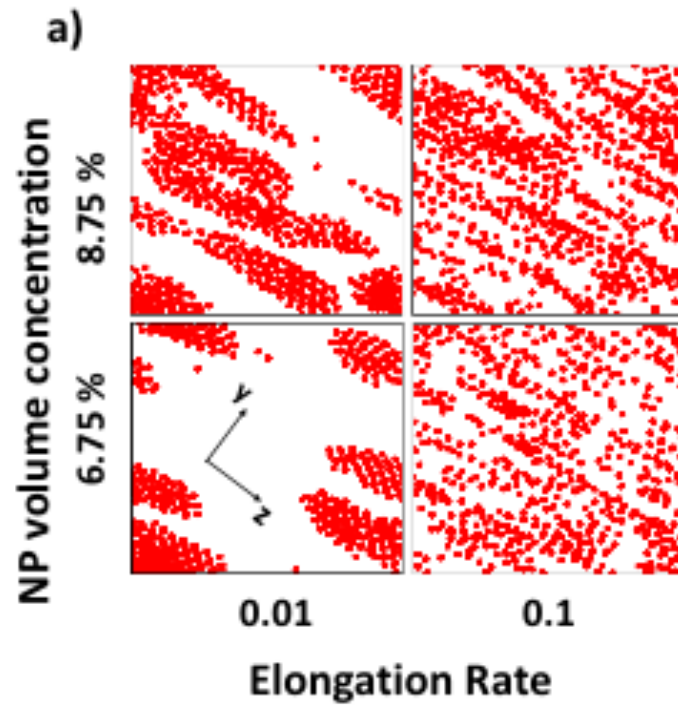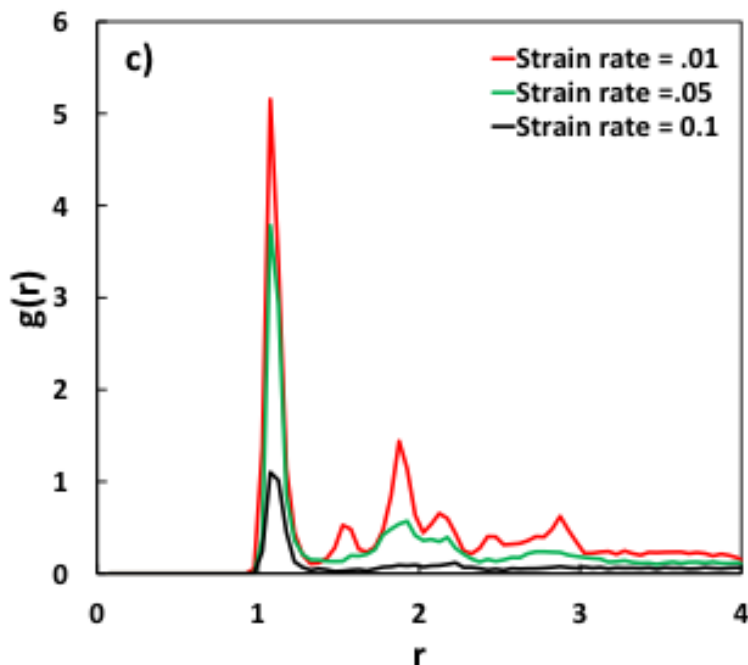
Figure 2.13. Non-equilibrium coarse-grained molecular dynamics simulation results. a) Snapshots of nanoparticle-polymer simulations. Polymer chains are omitted for clarity. Extension is in the *z* direction and compression is in the *y* direction, b) Simulation dispersion area for various elongation strain rates and nanoparticle concentrations, c) Pair correlation function for nanoparticle-polymer simulations at varying strain rate. NP volume concentration is 6.75%.

## 2.4. Summary

In this work, we have presented a systematic approach to control the spatial distribution of unfunctionalized spherical nanoparticles in polymer nanocomposites. Our results demonstrate that the application of high but controlled circumferentially uniform air flow in gas-assisted electrospinning provided additional extensional deformation, and therefore enhanced dispersion and orientation of various nanofillers. First, the effect of extensional deformation on nanofiller dispersion was tested on small $SiO_2$ NPs that were incorporated in PVA/water solution at different loadings. Solutions were spun using conventional ES and GAES at different air flow rates, and

resulting fibers were analyzed by taking TEM images and utilizing two novel image analysis techniques. Our results also demonstrate that with the increase of the air flow rate, and therefore extensional deformation, one can achieve a 350% improvement in dispersion area and an average of 75% decrease in the most probable separation between individual particles and agglomerates. This indicates a significant enhancement in $SiO_2$ dispersion in PVA nanofibers. Improvement is mostly due to strain-induced rupture of nanoparticle agglomerates that occurs when deformational forces overcome cohesive forces between NPs. Mentioned results have been verified by a simple time-scale analysis, which indicated that $t_{diff}/t_{strain} = 6.7$, confirming that extension is a homogenizing force and controls the spatial distribution of $SiO_2$ NPs. FFT results show an empirical evidence of two dispersion regimes, that correspond to $Pe_0 < 6.77$ where diffusion-enhanced distribution mechanism is in competition with the deformation-induced rupture, and $Pe_0 > 6.77$ where the deformation-enhanced distribution mechanism dominates. In addition, we demonstrated the ability to disperse large Si NPs in polymer nanofibers. With the application of the high air flow rate during GAES of PVA/Si solutions we observed a twofold improvement in dispersion area and a 35% decrease in the most probable separation between particles or agglomerates, which indicated a significant improvement in NP dispersion and agglomerate rupture. It is expected that the enhanced diffusivity contribution to the dispersion improvement of Si is negligible, due to a large size of the NP. It was verified by the convection to diffusion rate analysis of the initiation of the polymer jet, that shows almost an order of magnitude decrease of $Pe_0^{Si}$ compared to $Pe_0^{SiO_2}$, resembling slower dispersion kinetics of silicon NPs. The overall time scale analysis indicates that the strain time scale is three orders of magnitude smaller than the diffusivity time scale, indicating that extension is a dominating force and becomes more prominent for large nanoparticles. Furthermore, the ability to effectively produce a large amount of high

surface area nanocomposite material and control NP agglomeration in a single step process, inspired us to utilize this technique in manufacturing of a Li-battery anode material. High surface area, non-woven fiber mats were fabricated via ES and GAES of highly loaded solution of Si NPs and CNTs in PVA. GAES fibers exhibited more than 600 mAh/g improvement of capacity in both fast and slow current rates at the same Si NP loading, which is attributed to enhancement of dispersion of nanofillers and more accessible surface for electrochemical reactions. The study on the control of spatial distribution and orientation of anisotropic particles (CNTs and graphene nanoribbons (GNRs)) is presented in Chapter 3 of this thesis.  All the results in the current study were qualitatively confirmed with a non-equilibrium coarse-grained molecular dynamics to reinforce the idea that increasing extensional strain by using gas-assisted electrospinning is an effective strategy for improving nanoparticle dispersion. To the best of our knowledge, this is the first work in which the control over the placement of various nanofillers in polymer nanofibers has been achieved by tuning the driving force of the manufacturing process. Therefore, the success of current method in improving NP dispersion and preventing agglomeration can obviate both nanoparticle functionalization and multi-step process for desired nanocomposite fabrication.

# REFERENCES

[1]     A. C. Balazs, T. Emrick, and T. P. Russell, "Nanoparticle polymer composites: where two small worlds meet," *Science*, vol. 314, no. November, pp. 1107–1110, 2006.

[2]     V. Kalra, F. Escobedo, and Y. L. Joo, "Effect of shear on nanoparticle dispersion in polymer melts: A coarse-grained molecular dynamics study," *J. Chem. Phys.*, vol. 132, no. 2010, pp. 024901–024912, 2010.

[3]     M. R. Bockstaller, R. A. Mickiewicz, and E. L. Thomas, "Block copolymer nanocomposites: Perspectives for tailored functional materials," *Adv. Mater.*, vol. 17, no. June 2015, pp. 1331–1349, 2005.

[4]     G. A. Buxton and A. C. Balazs, "Simulating the morphology and mechanical properties of filled diblock copolymers," *Phys. Rev. E. Stat. Nonlin. Soft Matter Phys.*, vol. 67, no. March, pp. 031802–031814, 2003.

[5]     A. K. Khandpur, S. Forster, F. S. Bates, I. W. Hamley, A. J. Ryan, W. Bras, K. Almdal, and K. Mortensen, "Polyisoprene-Polysterene Diblock Copolymer Phase Diagram near the Order-Disorder Transition," *Macromolecules*, vol. 28, pp. 8796–8806, 1995.

[6]     R. Krishnamoorti and K. Yurekli, "Rheology of polymer layered silicate nanocomposites," *Curr. Opin. Colloid Interface Sci.*, vol. 6, pp. 464–470, 2001.

[7]     M. Kamibayashi, H. Ogura, and Y. Otsubo, "Shear-thickening flow of nanoparticle suspensions flocculated by polymer bridging," *J. Colloid Interface Sci.*, vol. 321, pp. 294–301, 2008.

[8]     S. Srivastava, J. H. Shin, and L. A. Archer, "Structure and rheology of nanoparticle–polymer suspensions," *Soft Matter*, vol. 8, p. 4097, 2012.

[9]     V. Kalra, S. Mendez, F. Escobedo, and Y. L. Joo, "Coarse-grained molecular dynamics simulation on the placement of nanoparticles within symmetric diblock copolymers under shear flow," *J. Chem. Phys.*, vol. 128, no. 2008, pp. 164909–164920, 2008.

[10]    V. Kalra and Y. L. Joo, "Coarse-grained molecular dynamics study of block copolymer/nanoparticle composites under elongational flow," *J. Chem. Phys.*, vol. 131, no. 21, p. 214904, 2009.

[11]    J. H. Park, V. Kalra, and Y. L. Joo, "Controlling the dispersion and orientation of nanorods in polymer melt under shear: Coarse-grained molecular dynamics simulation study," *J. Chem. Phys.*, vol. 140, pp. 124903–124920, 2014.

[12]    J. H. Park and Y. L. Joo, "Tailoring nanorod alignment in a polymer matrix by elongational flow under confinement: simulation, experiments, and surface enhanced Raman scattering application.," *Soft Matter*, vol. 10, pp. 3494–3505, 2014.

[13]    V. Kalra, J. Lee, J. H. Lee, S. G. Lee, M. Marquez, U. Wiesner, and Y. L. Joo, "Controlling nanoparticle location via confined assembly in electrospun block copolymer nanofibers," *Small*, vol. 4, no. 11, pp. 2067–2073, 2008.

[14]    S. C. Warren, L. C. Messina, L. S. Slaughter, M. Kamperman, Q. Zhou, S. M. Gruner, F. J. DiSalvo, and U. Wiesner, "Ordered mesoporous materials from metal nanoparticle-block copolymer self-assembly.," *Science*, vol. 320, no. June, pp. 1748–1752, 2008.

[15]    E. Zhmayev, D. Cho, and Y. L. Joo, "Nanofibers from gas-assisted polymer melt electrospinning," *Polymer (Guildf).*, vol. 51, no. 18, pp. 4140–4144, Aug. 2010.

[16]    A. E. Spivak, Y. A. I. Dzenis, and D. H. Reneker, "A model of steady state jet in the electrospinning process," *Mech. Res. Commun.*, vol. 27, no. 1, pp. 37–42, 2000.

[17]  M. M. Hohman, M. Shin, G. Rutledge, and M. P. Brenner, "Electrospinning and electrically forced jets. I. Stability theory," *Phys. Fluids*, vol. 13, no. 8, p. 2201, 2001.

[18]  M. M. Hohman, M. Shin, G. Rutledge, and M. P. Brenner, "Electrospinning and electrically forced jets. II. Applications," *Phys. Fluids*, vol. 13, no. 8, pp. 2221–2236, 2001.

[19]  J. J. Feng, "The stretching of an electrified non-Newtonian jet: A model for electrospinning," *Phys. Fluids*, vol. 14, no. 11, p. 3912, 2002.

[20]  Y. M. Shin, M. M. Hohman, M. P. Brenner, and G. C. Rutledge, "Experimental characterization of electrospinning: the electrically forced jet and instabilities," *Polymer (Guildf).*, vol. 42, no. 25, pp. 09955–09967, Dec. 2001.

[21]  C. P. Carroll and Y. L. Joo, "Electrospinning of viscoelastic Boger fluids: Modeling and experiments," *Phys. Fluids*, vol. 18, no. 5, p. 53102, 2006.

[22]  R. B. Thompson, V. V Ginzburg, M. W. Matsen, and  a C. Balazs, "Predicting the mesophases of copolymer-nanoparticle composites.," *Science*, vol. 292, no. June, pp. 2469–2472, 2001.

[23]  J. J. Chiu, B. J. Kim, E. J. Kramer, and D. J. Pine, "Control of nanoparticle location in block copolymers," *J. Am. Chem. Soc.*, vol. 127, pp. 5036–5037, 2005.

[24]  A. J. Schultz, C. K. Hall, and J. Genzer, "Computer simulation of block copolymer/nanoparticle composites," *Macromolecules*, vol. 38, pp. 3007–3016, 2005.

[25]  A. Yazdanbakhsh, Z. Grasley, B. Tyson, and R. K. Abu Al-Rub, "Dispersion quantification of inclusions in composites," *Compos. Part A Appl. Sci. Manuf.*, vol. 42, no. 1, pp. 75–83, 2011.

[26] P. T. Cummings, B. Y. Wang, D. J. Evans, and K. J. Fraser, "Nonequilibrium molecular dynamics calculation of self-diffusion in a non-Newtonian fluid subject to a Couette strain field," *J. Chem. Phys.*, vol. 94, no. 1991, pp. 2149–2158, 1991.

[27] S. Sarman, J. Evans, and A. Baranyai, "Mutual and delf-diffusion in fluids undergoing strong shear," *Phys. Rev. A*, vol. 46, no. 2, pp. 893–902, 1992.

[28] X. Qiu, H. D. Ou-Yang, D. J. Pine, and P. M. Chaikin, "Self-diffusion of interacting colloids far from equilibrium," *Phys. Rev. Lett.*, vol. 61, no. 22, pp. 2554–2557, 1988.

[29] J. R. Abbott, N. Tetlow, A. L. Graham, S. A. Altobelli, E. Fukushima, L. A. Mondy, and T. S. Stephens, "Experimental observations of particle migration in concentrated suspensions: Couette flow," *J. Rheol. (N. Y. N. Y).*, vol. 35, no. 1991, pp. 773–795, 1991.

[30] C. J. Koh, P. Hookham, and L. G. Leal, "An experimental investigation of concentrated suspension flows in a rectangular channel," *J. Fluid Mech.*, vol. 266, pp. 1–32, 1994.

[31] W. Xue and G. S. Grest, "Brownian dynamics simulations for interacting colloids in the presence of a shear flow," *Phys. Rev. A*, vol. 40, no. 3, pp. 1709–1712, 1989.

[32] C. Chang and R. L. Powell, "Self-diffusion of bimodal suspensions of hydrodynamically interacting spherical particles in shearing flow," *J. Fluid Mech.*, vol. 281, pp. 51–80, 1994.

[33] V. Kalra, J. H. Lee, J. H. Park, M. Marquez, and Y. L. Joo, "Confined assembly of asymmetric block-copolymer nanofibers via multiaxial jet electrospinning," *Small*, vol. 5, no. 20, pp. 2323–2332, 2009.

[34] A. M. Kraynik and D. A. Reinelt, "Extensional motions of spatially periodic lattices," *Int. J. Multiph. Flow*, vol. 18, no. 6, pp. 1045–1059, 1992.

[35] B. D. Todd and P. J. Daivis, "The stability of nonequilibrium molecular dynamics

simulations of elongational flows," *J. Chem. Phys.*, vol. 112, no. 1, pp. 40–46, 2000.

[36]   B. D. Todd and P. J. Daivis, "New algorithm for unrestricted duration nonequilibrium molecular dynamics simulations of planar elongational flow," *Comput. Phys. Commun.*, vol. 117, no. 3, pp. 191–199, 1999.

[37]   F. Zhang, D. J. Searles, D. J. Evans, J. S. D. T. Hansen, D. J. Isbister, D. J. Searles, and D. J. Evans, "Kinetic energy conserving integrators for Gaussian thermostatted SLLOD," *J. Chem. Phys.*, vol. 111, no. 1, pp. 18–26, 1999.

[38]   M. L. Matin, P. J. Daivis, and B. D. Todd, "Comparison of Planar Shear Flow and Planar Elongational Flow For Systems of Small Molecules," *J. Chem. Phys.*, vol. 113, no. 20, pp. 9122–9131, 2000.

[39]   W. Bruns and R. Bansal, "Molecular dynamics study of a single polymer chain in solution," *J. Chem. Phys.*, vol. 74, no. 3, pp. 2064–2072, 1979.

[40]   J. Weeks, D. Chandler, and H. C. Andersen, "Role of Repulsive Force in Determining the Equilibrium Structure of Simple Liquids," *J. Chem. Phys.*, vol. 54, no. 12, p. 5237, 1971.

[41]   M. J. Park, K. Char, J. Park, and T. Hyeon, "Effect of the Casting Solvent on the Morphology of Poly ( styrene-b-isoprene ) Diblock Copolymer / Magnetic Nanoparticle Mixtures," *Langmuir*, vol. 22, no. 4, pp. 10–13, 2006.

[42]   R. Teki, R. Krishnan, T. C. Parker, T. M. Lu, P. N. Kumta, and N. Koratkar, "Nanostructured silicon anodes for lithium Ion rechargeable batteries," *Small*, vol. 5, pp. 2236–2242, 2009.

[43]   C. M. Wang, X. Li, Z. Wang, W. Xu, J. Liu, F. Gao, L. Kovarik, J. G. Zhang, J. Howe, D. J. Burton, Z. Liu, X. Xiao, S. Thevuthasan, and D. R. Baer, "In situ TEM investigation of

congruent phase transition and structural evolution of nanostructured silicon/carbon anode for lithium ion batteries," *Nano Lett.*, vol. 12, pp. 1624–1632, 2012.

[44]   J. Bravo, L. Zhai, Z. Wu, R. E. Cohen, and M. F. Rubner, "Transparent superhydrophobic films based on silica nanoparticles," *Langmuir*, vol. 23, no. 28, pp. 7293–7298, 2007.

[45]   F. B. Wyart and P. G. de Gennes, "Viscosity at small scales in polymer melts," *Eur. Phys. J. E*, vol. 97, pp. 93–97, 2000.

[46]   P. G. de Gennes, "Wetting: statistics and dynamics," *Rev. Mod. Phys.*, vol. 57, no. 3, pp. 827–863, 1985.

[47]   P. G. de Gennes, "Reptation of a Polymer Chain in the Presence of Fixed Obstacles," *J. Chem. Phys.*, vol. 55, no. 1971, pp. 572–579, 1971.

[48]   A. Tuteja, M. E. Mackay, S. Narayanan, S. Asokan, and M. S. Wong, "Breakdown of the continuum Stokes-Einstein relation for nanoparticle diffusion," *Nano Lett.*, vol. 7, no. 5, pp. 1276–1281, 2007.

[49]   V. Ganesan, V. Pryamitsyn, M. Surve, and B. Narayanan, "Noncontinuum effects in nanoparticle dynamics in polymers," *J. Chem. Phys.*, vol. 124, no. 22, p. 221102, 2006.

[50]   T. L. Labus and E. P. Symons, "Experimental investigation of an axisymmetric free jet with an initially uniform velocity profile," *Washington, D.C.  Natl. Aeronaut. Sp. Adm.*, pp. 1–22, 1972.

[51]   Y. Yao, M. T. McDowell, I. Ryu, H. Wu, N. Liu, L. Hu, W. D. Nix, and Y. Cui, "Interconnected silicon hollow nanospheres for lithium-ion battery anodes with long cycle life," *Nano Lett.*, vol. 11, pp. 2949–2954, 2011.

[52]   C. K. Chan, H. Peng, G. Liu, K. McIlwrath, X. F. Zhang, R. A. Huggins, and Y. Cui,

"High-performance lithium battery anodes using silicon nanowires.," *Nat. Nanotechnol.*, vol. 3, pp. 31–35, 2008.

[53]  H. Xiang, K. Zhang, G. Ji, J. Y. Lee, C. Zou, X. Chen, and J. Wu, "Graphene/nanosized silicon composites for lithium battery anodes with improved cycling stability," *Carbon N. Y.*, vol. 49, pp. 1787–1796, 2011.

[54]  Y. S. Hu, R. Demir-Cakan, M. M. Titirici, J. O. Müller, R. Schlögl, M. Antonietti, and J. Maier, "Superior storage performance of a Si@SiOx/C nanocomposite as anode material for lithium-ion batteries," *Angew. Chemie - Int. Ed.*, vol. 47, pp. 1645–1649, 2008.

[55]  K. Zhao, L. Zhang, R. Xia, Y. Dong, W. Xu, and C. Niu, "SnO 2 Quantum Dots @ Graphene Oxide as a High-Rate and Long-Life Anode Material for Lithium-Ion Batteries," *Small*, vol. 12, no. 5, pp. 588–594, 2016.

[56]  Z. Li, H. Zhang, Q. Liu, Y. Liu, L. Stanciu, and J. Xie, "Novel Pyrolyzed Polyaniline-Grafted Silicon Nanoparticles Encapsulated in Graphene Sheets As Li-Ion Battery Anodes," *ACS Appl. Mater. Interfaces*, vol. 6, pp. 5996–6002, 2014.

[57]  J. H. Park, V. Kalra, and Y. L. Joo, "Controlling the dispersion and orientation of nanorods in polymer melt under shear: Coarse-grained molecular dynamics simulation study," *J. Chem. Phys.*, vol. 140, no. 12, p. 124903, 2014.

[58]  B. J. Landi, M. J. Ganter, C. D. Cress, R. A. DiLeo, and R. P. Raffaelle, "Carbon nanotubes for lithium ion batteries," *Energy Environ. Sci.*, vol. 2, no. 6, pp. 638–654, 2009.

[59]  E. Frackowiak and F. Beguin, "Electrochemical storage of energy in carbon nanotubes and nanostructured carbons," *Carbon N. Y.*, vol. 40, pp. 1775–1787, 2002.

[60] S. H. Ng, J. Wang, Z. P. Guo, J. Chen, G. X. Wang, and H. K. Liu, "Single wall carbon nanotube paper as anode for lithium-ion battery," *Electrochim. Acta*, vol. 51, no. 1, pp. 23–28, Oct. 2005.

[61] G. Zhou, D.-W. Wang, F. Li, L. Zhang, N. Li, Z.-S. Wu, L. Wen, G. Q. (Max) Lu, and H.-M. Cheng, "Graphene-Wrapped Fe3O4 Anode Material with Improved Reversible Capacity and Cyclic Stability for Lithium Ion Batteries," *Chem. Mater.*, vol. 22, no. 18, pp. 5306–5313, Sep. 2010.

[62] Z. Lu, N. Liu, H. W. Lee, J. Zhao, W. Li, Y. Li, and Y. Cui, "Nonfilling Carbon Coating of Porous Silicon Micrometer-Sized Particles for High-Performance Lithium Battery Anodes," *ACS Nano*, vol. 9, no. 3, pp. 2540–2547, 2015.

[63] B. Wang, X. Li, X. Zhang, B. Luo, M. Jin, M. Liang, S. A. Dayeh, S. T. Picraux, and L. Zhi, "Adaptable silicon-carbon nanocables sandwiched between reduced graphene oxide sheets as lithium ion battery anodes," *ACS Nano*, vol. 7, no. 2, pp. 1437–1445, 2013.

[64] E. Pollak, G. Salitra, V. Baranchugov, and D. Aurbach, "In Situ Conductivity, Impedance Spectroscopy, and Ex Situ Raman Spectra of Amorphous Silicon during the Insertion/Extraction of Lithium," *J. Phys. Chem. C*, vol. 111, no. 30, pp. 11437–11444, Aug. 2007.

[65] Z. X. Shu, R. S. McMillan, and J. J. Murray, "Electrochemical Intercalation of Lithium into Graphite," *J. Electrochem. Soc.*, vol. 140, no. 4, pp. 922–927, Apr. 1993.

[66] M. Endo, C. Kim, K. Nishimura, T. Fujino, and K. Miyashita, "Recent development of carbon materials for Li ion batteries," *Carbon N. Y.*, vol. 38, pp. 183–197, 2000.

# CHAPTER 3

# NON-ENTHALPIC ENHANCEMENT OF SPATIAL DISTRIBUTION AND ORIENTATION OF CNTs AND GNRs IN POLYMER NANOFIBERS FOR LI-ION BATTERY APPLICATIONS

## 3.1. Introduction

Control and enhancement of spatial distribution and orientation of various nanofillers in polymer matrices has a crucial effect on inherent functionalities of advanced polymer nanocomposites. Such nanostructured materials find a lot of applications due to their novel thermal, mechanical, optic and electric properties. [1–6] Carbon nanofillers, and nanorods (NRs) in particular, have shown an increasing interest over the years, owing to their exclusive properties resulting from high aspect ratios. [7–13] Anisotropic nanoparticles (NPs), such as carbon nanotubes (CNTs) can notably improve electrical conductivity if they are well dispersed and randomly oriented in a polymer nanocomposite. [12–15] Likewise, they can enhance thermal conductivity if well-aligned in a polymer matrix. [16] Graphene structures have gained a lot of attention recently for the use in Si-based anode material for Li-batteries, due to their unique architecture and electrical properties. [7, 17–19] Graphene nanorribbons (GNRs), for instance, have an ultrathin and flexile structure that allows them to be easily embedded in polymer fibers, providing effective electronic pathways. [7] GNRs are generally derived through chemical unzipping of CNTs, which allows to control their physical and chemical properties, that are different from their precursor. [17]

NRs, as well as spherical NPs, exhibit high cohesive forces and readily flocculate in a polymer matrix that exhibits no or little affinity, resulting in less enhancement in physical

properties than predicted. [1, 2, 20–23] Various endeavors have been made to enhance and control spatial orientation and distribution, but there is no universal methodology so far. There is a myriad of mechanisms for NP and NR surface functionalization, to decrease the difference between solubility (Flory-Huggins parameter), therefore increase the affinity between substrate and filler. However, such manipulations often lead to a loss of magnetic, catalytic and electrical properties. For instance, surface-functionalized CNTs lose electrical conductivity due to disruption of pi conjugation. [6, 24–26] Hence, there is a high demand for reliable and efficient methods to control and enhance the dispersion and alignment of NRs, without altering their fundamental properties.

Recently, there was a plethora of experimental and computational studies on the application of external flow or electrical force to slow down agglomeration and direct the orientation of various nanofillers, such as spherical NPs [1, 2, 21, 23, 24, 27–29], and NRs [2, 20] in polymer matrices. For example Park *et al*. [2, 20] carried out a comprehensive computational study on the effect of shear and elongational deformation on dispersion and orientation of rigid NRs in polymer melts. It has been shown that elongation can significantly improve the spatial orientation and distribution of NRs, compared to shear at the same deformation rate. Mechanical deformation can change the kinetics of NR flocculation, increasing the aggregation time-scale via rupture of existing agglomerates and affecting diffusion coefficients. It was evident that under strong elongational deformation high aspect ratio NRs will align towards the flow almost instantly and stay in anisotropic state. This behavior results in less probability of individual NRs to encounter each other and form aggregates, concluding that orientational time scale is a dominant factor governing spatial distribution.

In our recent study, we have presented a novel and methodical approach to control spatial distribution and orientation of unfunctionalized $SiO_2$ and Si spherical NPs in polyvinyl alcohol

60

(PVA) nanofibers. [1] We demonstrated that employing circumferentially uniform and controlled air flow through a sheath layer of coaxial spinneret in gas-assisted electrospinning (GAES), contributed additional extensional deformation, thus enhanced dispersion of spherical nanofillers. Solutions were spun using conventional electrospinning (ES) and GAES at the same conditions to isolate the effect of added extensional deformation. We developed an effective analysis and quantification technique that shows a 350% improvement in the area occupied by $SiO_2$ nanoparticles (dispersion area analysis) and an average of 75% improvement in the most probable separation between individual NPs and their agglomerates (FFT analysis), after the increase of the air flow rate. Our results show an empirical evidence of two dispersion regimes, first at $Pe_0 < 6.77$ where diffusion-enhanced dispersion is in completion with the deformation-induced rupture, and second at $Pe_0 > 6.77$ where the deformation-enhanced dispersion mechanism prevails. We have demonstrated that GAES fibers exhibited more than 600 mAh/g improvement of capacity of the fabricated Li-ion battery anode material, which is attributed to enhancement of distribution of functional nanofillers and more accessible surface area for electrochemical interactions.

In the current study, we take a step forward and demonstrate an improved dispersion and control over orientation of CNTs and their unzipped counterparts GNRs in PVA nanofibers with the increase of extensional deformation during the fiber spinning process. Using the same methodology as in our previous work [1] we utilized ES, which is a versatile and facile method to produce nanofibers, by imposing a strong electric potential (~15-30 kV), on a polymer melt/solution. When the electric potential on the surface of the fluid overcomes surface tension, a Taylor cone is formed and a polymer jet is ejected. The charged jet is subjected to strong deformations (~10000 $s^{-1}$), and after fast solvent evaporation (~200 nL $s^{-1}$) and solidification, nano-scale fibers are collected on a grounded collector plate. GAES was utilized to isolate the effect of

enhanced extensional deformation, and is a novel process that employs a circumferentially uniform air flow as a sheath layer of a special coaxial nozzle during ES. [30–36] We produced CNT and GNR-loaded PVA nanofibers at different air flow rates (0, 2.5, 4, 5.5, 9 and 11 SCFH) for different NR concentrations, and at constant applied electric potential (100 kV/m), and addressed three fundamental questions regarding this type of nanocomposite. (1) What is the effect of additional extensional deformation provided by the sheath layer air flow on the CNT and GNR dispersion and orientation pattern? (2) What is the effect of physical and chemical properties, and geometry on their spatial distribution and alignment? (3) How the control of dispersion and orientation translates to the Li-ion battery performance?

CNTs and GNRs are kinetically "trapped" in solidified PVA nanofibers, making it advantageous for the post-process analysis and quantification. In this paper we utilize a previously developed quantification technique [1], with an emphasis on the TEM investigation of the microtomed longitudinal sections of CNT/GNR-loaded PVA nanofibers, which provides a unique opportunity to reveal splendid details of such complex dispersion behavior.

First TEM images are analyzed using the Dispersion Area Analysis (DAA) technique, which calculates the area occupied by NPs relative to the total fiber area. Gray-scale TEM images are converted to binary, keeping the pixel ratio, and analyzed to detect the fiber edge and highlight nanoinclusions. Then, the area ratio is calculated based on the number of pixels in each phase (polymer and NR). Both CNTs and GNRs are hydrophobic and agglomeration is a more energetically favorable state in aqueous PVA solution. However, with the application of a sheath layer air flow extensional forces overcome cohesive forces between NRs and result in a partial or complete agglomerate rupture. [6, 24, 37–43] Thus, there is a significant increase in the area occupied by NRs, which is captured by DAA. [1]

The second method of our spatial distribution analysis technique is the Fast Fourier Transform (FFT) that captures the most probable separation between individual particles and agglomerates. It is done radially in this study to form a probability distribution from which the wavelength corresponding to the most probable separation is chosen. Reduced separation values feature a statistical improvement of spatial distribution and agglomerate rupture. Most probable separation is conceptually similar to the pair correlation function that is commonly used in the coarse-grained molecular dynamics simulations (CGMD) [2, 20, 21, 23, 24], and describes a probability of finding a particle at some distance from a reference.

The last quantification technique is the orientation analysis, which is done by studying the alignment of anisotropic NPs. We measure the average angle of CNTs and GNRs in the flow direction, where $0^o$ is the perfect alignment and $90^o$ is the perpendicular orientation.

To the best of our knowledge this is a first successful attempt to control the spatial distribution and orientation of unfunctionalized CNTs and GNRs via tuning the extensional deformation during the fiber fabrication process. From a nanocomposite application viewpoint, it is important that we demonstrate a robust and powerful methodology for a single step production and control of NP dispersion and orientation for potential utilization in novel research fields, such as energy storage media. Spatial distribution and alignment of CNTs and GNRs is particularly important for Li-battery anode fabrication process, since it governs the electron delivery to the active material. When NRs agglomerate or completely align with the flow, some of the provided electronic pathways are concealed. Hence, a portion of the active material (Si) is not participating in the electrochemical reaction, but is considered in the mass/volume normalization. Therefore, active material will demonstrate low gravimetric and volumetric capacities.

Finally, to confirm our empirical observations and further investigate the role of the strong extensional deformation on the placement of anisotropic carbon additives, we simulated an ideal system of CNTs and GNRs in a polymer melt utilizing non-equilibrium coarse-grained molecular dynamics.

## 3.2. Experimental section

*Materials:* Nanofibers were fabricated using 88% mole Hydrolyzed Polyvinyl alcohol (Mw=78,000 g mol$^{-1}$), purchased from Polysciences, Inc, and CNTs/GNRs provided by EMD. GNRs were made following our patent lisence to unzip CNTs via hexadecyl-functionalization process. [21] Transmission electron microscopy and image analysis were carried out to measure the average dimensions and aspect ratios of nanoinclusions.

*Nanofiber fabrication:* 10% PVA/H$_2$O solution containing 2-5% CNTs or GNRs was prepared and spun into polymer nanofibers via conventional electrospinning and gas-assisted electrospinning at 0, 5.5, 9 and 11 SCFH air flow rate. The infusion rates for electrospinning and gas-assisted electrospinning were 0.003 and 0.01 ml min$^{-1}$ respectively, and the electric field was kept constant at 100 kV m$^{-1}$ for both processes. We refer the reader to our earlier work on electrospinning for a more thorough overview of the experimental setup. [1, 21, 30]

*Nanofiber characterization:* After collection, fibers were left in the furnace at 150 $^{\circ}$C overnight to crosslink hydroxyl groups and prevent water dissolution. Fibers were then embedded in epoxy matrix and left at 60 $^{\circ}$C for a week. Embedded samples were then microtomed into 70-nm thickness sections using Leica Ultracut UCT and stained with osmium tetroxide overnight. Ultrathin sections were analyzed under a Tecnai T12 transmission electron microscope (TEM) that

operated at 120 kV. Resulting TEM images were analyzed using MATLAB 2014R, ImageJ and Adobe Illustrator.

*Dispersion area analysis:* TEM grayscale images generally show poor contrast between carbon-based nanofibers (PVA) and carbon nanoinclusions (CNTs/GNRs) due to a small difference in the electron density, therefore NPs must be highlighted to initiate the image analysis. Images are converted to binary and noise is removed manually or by using filters. The binary image is a 2-dimensional array of ones (white region – polymer matrix) and zeroes (black region – background and nanoinclusions within the fiber). Fibers typically have curved geometries, thus they are divided into sub-images that are analyzed separately and then the results are combined. First, we align images along the horizontal axis, keeping the image size intact. Then we determine the difference between the maximum and the minimum of the coordinates of ones for every column of the array to obtain the fiber thickness along the axial direction. Integration of the thickness along the length gives the total area of the fiber. The integral of zeroes along the fiber length gives the total area occupied by nanoinclusions. The normalized ratio of two gives a dispersion area, which is an estimation of nanofiller dispersion on the longitudinal section of the fiber.

*Radial FFT analysis:* Normalization of the binary image is not required for the radial FFT analysis because the coordinates of the analyzed columns are the same. For each of the columns the coordinates of axisymmetric nanoinclusions are recorded and the fast Fourier transform of the data is obtained. The FFT analysis records wavenumbers, the reciprocal of which is the separation between individual NPs or agglomerates. The wavenumber at the highest amplitude is considered to be the predominant one and the corresponding separation recorded as the most probable for that column along the fiber. This procedure is reiterated for every column along the axial direction and the most frequent separations are recorded in a form of probability distribution. The separation

value corresponding to the highest probability is taken as a most probable separation. Axial FFT analysis is not performed here due to the axisymmetric geometry of CNTs and GNRs and their alignment with the flow in axial direction.

*Alignment analysis:* TEM images were examined to determine the angle off the longitudinal axis of PVA nanofiber for CNTs and GNRs. First, the images were aligned along the horizontal axis, and the flow direction (*z*-axis) was set to $0^o$. Thus, vertical direction (*r*-axis) is perpendicular to the fiber and the angle is set to $90^o$. Next, we select points along the axisymmetric nanoinclusion in order to find an average angle relative to the fiber z-axis. The same procedure is performed numerous times for all NPs within the fiber and for all TEM images and the result is summarized as a fraction of CNTs or GNRs at the angle off horizontal axis. An average aspect ratio determination is a side calculation in this procedure.

*Simulation Details:* 10000 coarse-grained polymer and nanorod beads were simulated using non-equilibrium molecular dynamics. Simulations were run starting from an isotropic state and continued until steady state was reached. To mimic the effects of electrospinning, planar elongation was applied to the simulation box. Although not identical to the uniaxial extension expected in electrospinning, planar elongation contains similar extension and compression and has the advantage of having a well-studied infinite time solution in MD. [44–46] The flow field was applied using the SLLOD equations of motion, which were integrated using a Velocity Verlet algorithm. [47] The code was validated by comparison with the results of Matin *et al*. [48]

Polymer chains of length 20 were bonded through a method of constraints used in Bruns *et al.* [49], which allows a larger integration time step by fixing the bond lengths. For polymer-polymer and polymer-nanorod interactions, the repulsive Weeks-Chandler-Anderson potential was used. [50] To simulate the attractive behavior of the nanorods, nanorod-nanorod interactions

were modeled by a cut and shifted Lennard-Jones potential. Stiffness of the nanorods chains was applied by a harmonic angle potential.

### 3.3. Results and Discussions

*3.3.1. The Dispersion Study of CNTs and GNRs in PVA nanofibers*

Figure 3.1 shows TEM images of CNTs and GNRs embedded in PVA nanofibers that were spun via conventional ES and GAES at 5.5, 9 and 11 SCFH air flow rate. Initial mixing in solution is obtained by ultrasonication that breaks down the agglomerates of nanowire-like anisotropic carbon nanoinclusions. Aspect ratios were measured during the alignment analysis by recording the ratio of the length to diameter of CNTs and GNRs, and are determined to be 16 and 10 respectively. It should be pointed out that GNRs, if unzipped, would almost double their width compared to CNTs [7], and become more brittle and responsive to mechanical deformation.

The unzipping procedure requires hexadecyl-functionalization [7, 17], which may functionalize the surface of graphene and increase the affinity between GNRs and the polymer solution. However, we want to stress that our approach to control spatial distribution and alignment of axisymmetric NPs is unique due to the application of additional extensional deformation exclusively. Generally, particles are deliberately surface-functionalized to ensure the minimization of Flory Huggins interaction parameter, therefore to maximize the number of enthalpic interactions between a substrate and a filler. [21, 51] In the current study we intend to investigate the solo effect of external mechanical deformation on axisymmetric carbon-NP dispersion and orientation in PVA nanofibers.

CNTs and GNRs are hydrophobic, therefore have a low affinity to PVA/water solution and readily form large flocculates with high interparticle forces. These cohesive forces could be

overcome by strong extensional deformation in ES process, which significantly reduce the size of NP agglomerates that are later kinetically trapped within the fiber polymer matrix (Figure: 3.1 (a); 3.1 (e)). However, with the application of the circumferentially uniform air flow we can see a noticeable enhancement in nanoparticle dispersion and agglomerate rupture, as well as an overall yield of CNTs and GNRs in PVA nanofibers (Figure: 3.1 (b-d); 3.1 (f-h)). Similar behavior was observed in our previous study [1], and explained by a ~2(O) magnitude increase of initial extensional deformation in the GAES process compared to conventional ES. It has been empirically observed that a diffusion-enhanced dispersion is a leading mechanism during ES process, and the application of the fast but controlled sheath layer air flow (5.5 SCFH) results in domination of the convective rate, responsible for the deformation-induced rupture mechanism.

To quantify the empirically evident enhancement in spatial distribution of NPs within the nanofiber we carried out two techniques for post-process image analysis.
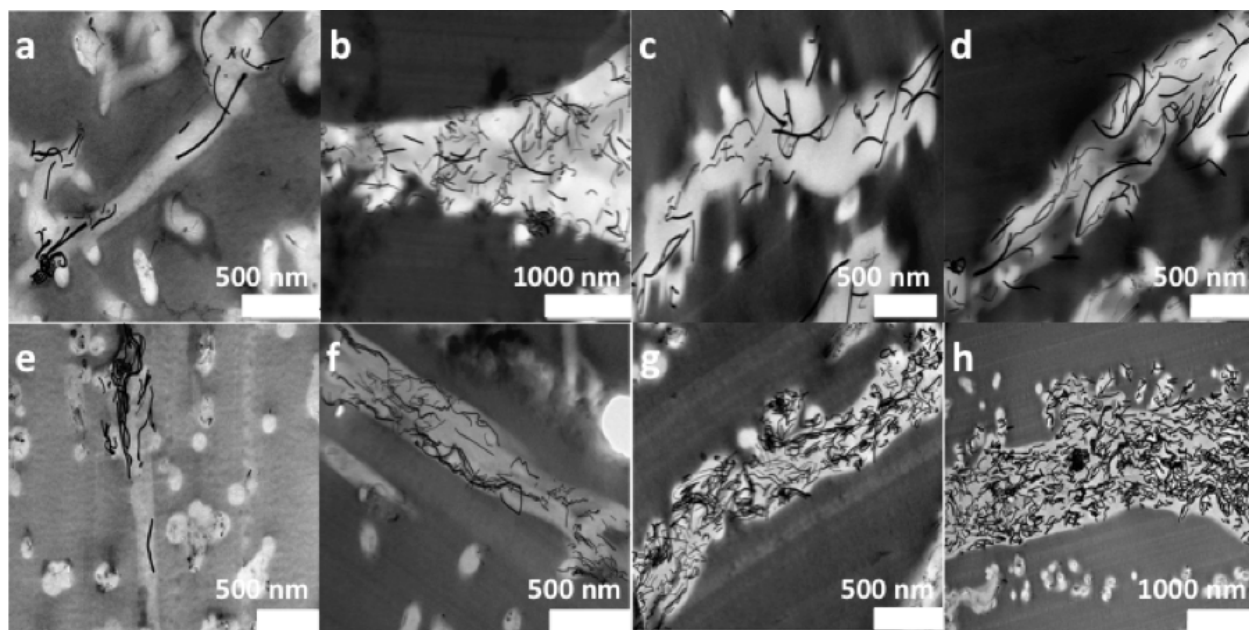
Figure 3.1. TEM images of microtomed longitudinal sections of PVA nanofibers with CNTs (5 vol% to PVA) spun at a) 0, b) 5.5, c) 9, d) 11 SCFH air flow rate; and GNRs (5 vol% to PVA) spun at e) 0, f) 5.5, g) 9, h) 11 SCFH air flow rate, at 100 kV m$^{-1}$.

### 3.3.1.1. Dispersion Area Analysis

The first method quantifies the area occupied by anisotropic nanoincluisons relative to the total area of the polymer nanofiber, and is referred to as a Dispersion Area Analysis (DAA). Aforementioned procedure is elaborately explained in one of our earlier manuscripts [1], and some important details are provided in the Experimental Section. It is expected that hydrophobic CNTs and GNRs would form spheroidal clusters in order to minimize the contact area with the water-based PVA solution. Therefore, the increase in dispersion area is the evidence of agglomerate rupture and dispersion enhancement for the same NP loading.

Figure 3.2 summarizes the DAA results for CNTs and GNRs at different loadings and plotted against Peclet number ($Pe_0$), which is a dimensionless ratio of diffusion and convection

time scales at the onset of fiber spinning, and increases with the increment in external deformation. It is evident that for all concentrations and different geometries there is a significant improvement in dispersion area with the utilization of the high air flow rate, thus added extensional deformation.

The effect of the additional deformation was especially prominent for GNRs (Figure 3.2 (b)), where dispersion area increased by almost 90%. It should be noted that GNRs require significantly lower deformation rates (lower $Pe_0$) to increase agglomeration time scale and rupture agglomerates, compared to their axisymmetric counterparts. This can be explained by a fast response to deformation of a less rigid and wider structure, and a higher affinity between GNRs and water–based PVA solution due to surface functionality remaining after the unzipping process. It has been previously shown that the carbon bond cleavage via oxidation results in carboxyl and hydroxyl group presence on the GNR edges, which may lead to a trapped water presence and high graphene affinity to polar solvents. [17] Thus, as expected, the ratio of composite occupied by GNRs will increase with nanoribbon concentration, due to a relatively easy agglomerate fracture and substaintivity.

On the other hand, CNTs show an average of 60% enhancement in dispersion area with the increase of the initial deformation rate (Figure 3.2 (a)), but remains at approximately 15% of the total area for both concentrations. It is important to note, that CNTs require almost three times the deformation to get to the same spatial distribution as their unzipped counterparts. This behavior is the result of increased stiffness and stronger cohesive forces between individual CNTs, which allows the formation of highly packed and oriented agglomerates that are resilient to strong deformations. It should be mentioned that CNT surface is not functionalized and remains hydrophobic, therefore agglomeration is a more energetically favorable state and its time scale will be minimized in a polar solution.

It should be noted that the effect of the nanofiller loading was previously investigated for spherical nanoinclusions, and proved to be negligible for low concentration of nanofiller. However, a much higher elongational deformation is required to ensure good dispersion of a highly loaded system. [1] The actual NP volume concentration in the PVA fiber may be lower than the calculated one, due to a lower CNT yield associated with poor enthalpic interactions and deficient agglomerate rupture. Similar dispersion pattern was well predicted by our MD simulation, and presented in more detail in the later section.
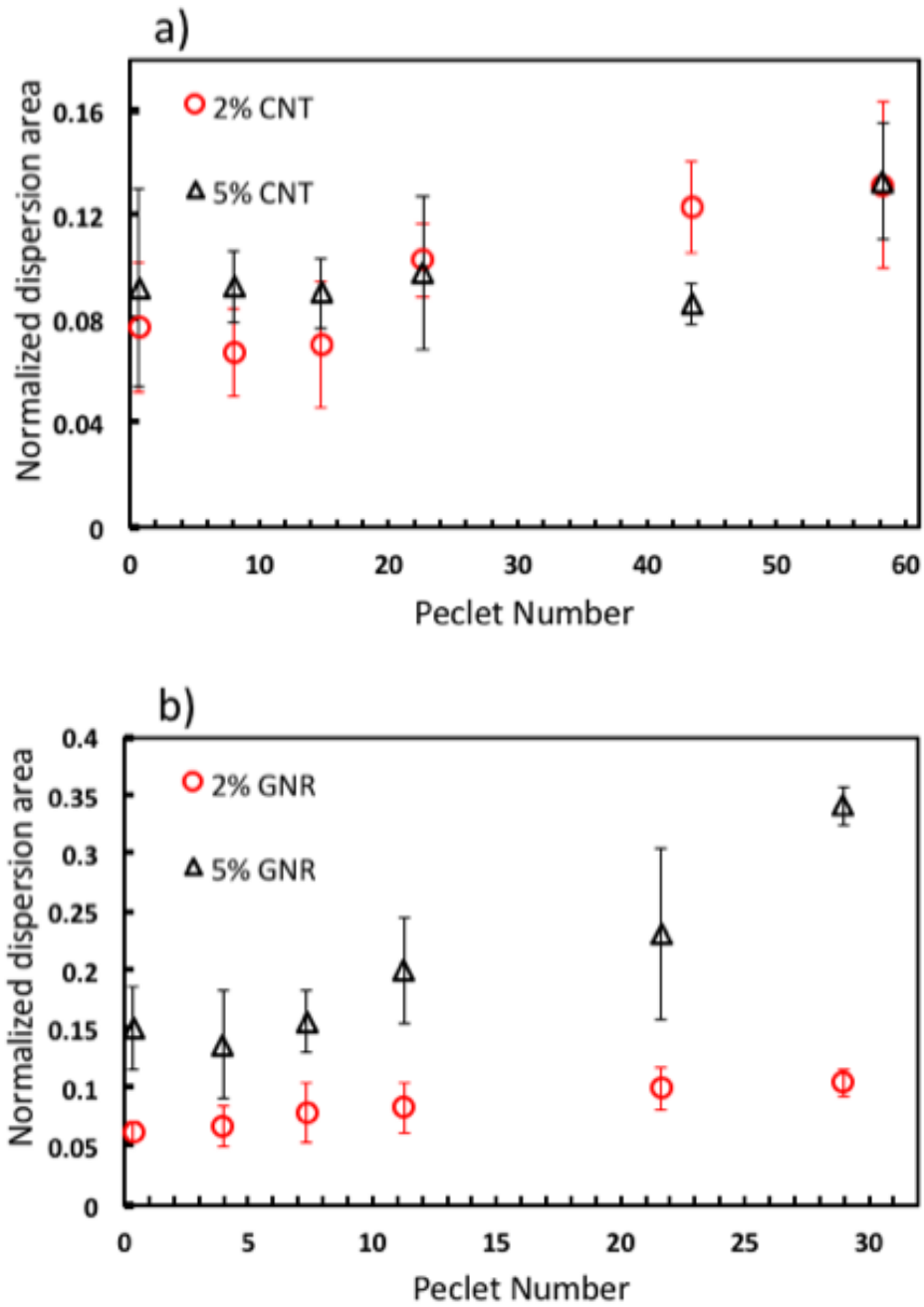
Figure 3.2. Dispersion area analysis results for electrospinning and gas-assisted electrospinning at different air flow rates of a) PVA/CNT and b) PVA/GNR solutions with different nanoparticle loading.

*3.3.1.2. Most Probable Separation Analysis via FFT*

To further analyze the dispersion improvement pattern we utilized a second quantification technique, which is referred to as a radial Fast Fourier Transform Analysis (FFT). This procedure allows finding the most probable separation between CNTs or GNRs in PVA nanofibers. For more details we refer the reader to our recent work on spherical NP dispersion. [1] Some of the key technicalities are provided in the Experimental Section.

Figure 3.3 summarizes the radial separation of anisotropic NPs at different loadings as a function of Peclet number. It has been observed that for all NP loadings used in the current study there is a 50% decrease in radial separation between individual CNTs or GNRs with the application of a high but controlled air flow. Lower separation values are indicative of improved spatial distribution and cluster rupture. It should be noted that GNRs require twice as less initial extensional deformation to homogenize in the dispersion domain, compared to their zipped counterparts, due to a flexible structure and better affinity to dispersion media. The most probable separation is conceptually similar to the pair correlation function which illustrates inter-particle spacing variation and commonly utilized in CGMD studies. [2, 20, 21, 23, 24]

A significant decrease in the most probable separation occurred from conventional ES to the intermediate air flow rate GAES for both CNTs and GNRs, and it is crucial to note that the same transition took place in our previous study on the effect of extensional deformation on spherical NP dispersion in PVA nanofibers. [1] Using the same reasoning and a rigorous time scale analysis, we can conclude that there is an evidence of a significant contribution in extensional deformation provided by the sheath layer air flow at the initial stage of fiber spinning. This contribution results in the existence of two dispersion-governing regimes.

In the earliest stage of the first regime the diffusion-enhanced dispersion is a leading mechanism and responsible for the homogenization of CNT/GNR distribution within the fiber in conventional ES ($Pe_0 = 0.7$ for CNTs; $Pe_0 = 0.3$ for GNRs). Next, with the application of the low air flow there is an order of magnitude increase in the initial strain rate, which results in the convection component development. Thus, the diffusion-enhanced dispersion mechanism starts competing with the deformation-enhanced dispersion mechanism, which becomes dominant when the air flow rate is further increased ($0.7 < Pe_0 < 23$ for CNTs; ($0.3 < Pe_0 < 11$ for GNRs). It was empirically observed that the transition point between two regimes occurs at an intermediate air flow rate ($Pe_0 = 23$ for CNTs; $Pe_0 = 11$ for GNRs), which is similar to our previous observations. [1] It can be concluded that to ensure an excellent spatial distribution of anisotropic nanofillers in polymer nanofibers it is essential to utilize the deformation-enhanced dispersion regime via application of a high air flow rate.
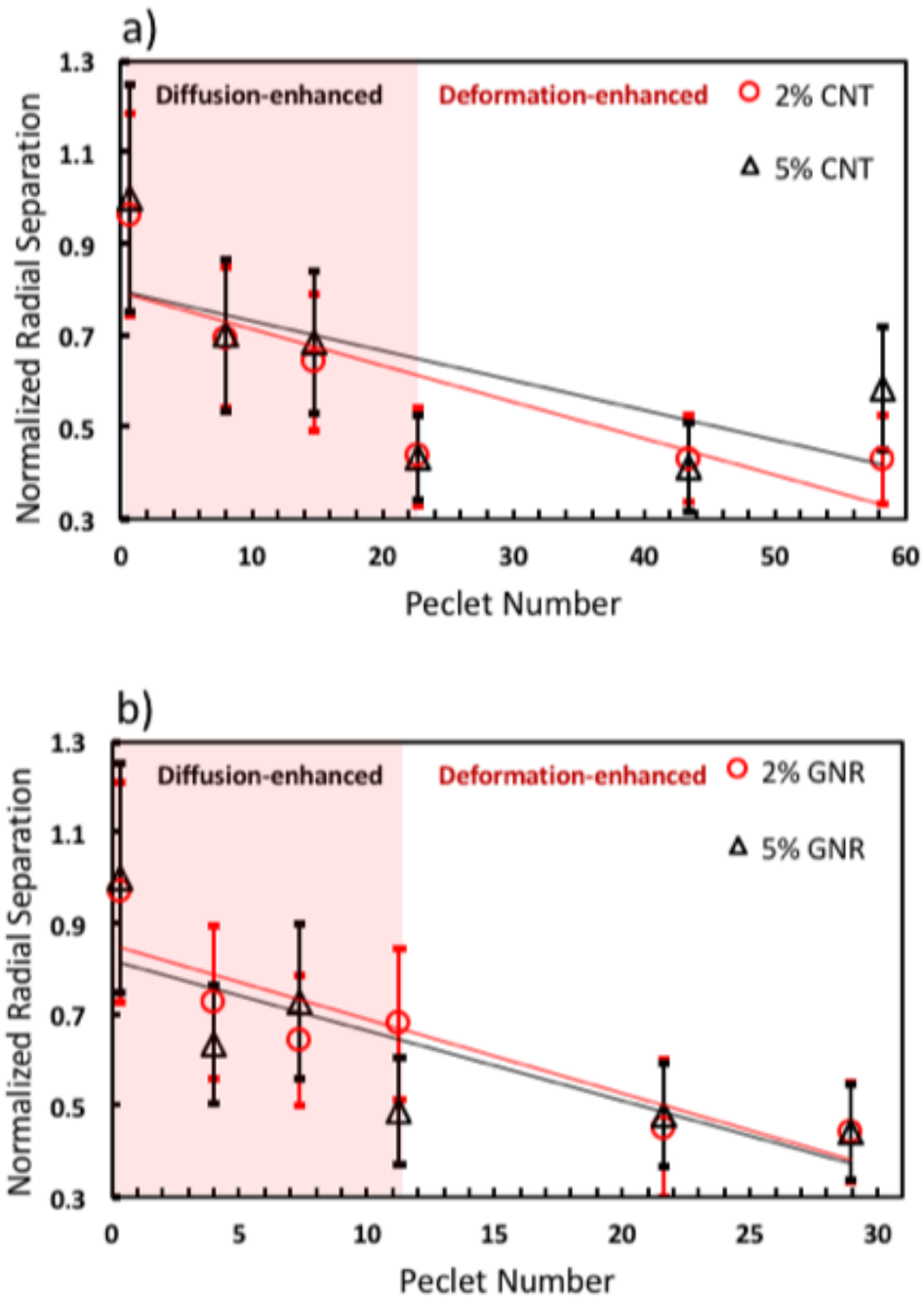
Figure 3.3. Dispersion regime study results from Fast Fourier Transform Analysis of ES and GAES (2.5, 4, 5.5, 9, 11 SCFH) at the initial stage of spinning for a) PVA/CNT and b) PVA/GNR solutions with different nanoparticle loading.

*3.3.1.3. Alignment Analysis*

The final analysis procedure aims to investigate the effect of the elongational deformation on the spatial orientation of CNTs and GNRs in PVA nanofibers. The weighted average angle off the flow direction, along the fiber longitudinal direction, was measured for 1-D NPs following the procedure described in the Experimental Section.

It is evident from Figure 3.4 that applying and increasing the sheath layer air flow during GAES process has a significant effect on CNT and GNR orientation within the electrospun polymer nanocomposite. As expected, after a significant increase in the initial extensional deformation, we observed a 30% linear improvement in spatial orientation of CNTs.

Similar behavior was observed in other studies [2, 20], and was well comprehended by studying the orientational component of NP motion in polymeric fluid. The orientational time scale remains significantly smaller than the translational one and keeps decreasing as the deformation rate is increased. Therefore, at higher initial deformations, CNTs would align with the flow faster and remain oriented and well dispersed. CNTs are much more rigid than GNRs and more uniformly respond to deformation, thus to decrease resistance to the flow they are more prone to align along the flow axis. It is important to note that long PVA chains are well oriented to the flow direction in polymer nanofibers, which guides nanotubes and aids their alignment.

However, it was observed that the alignment behavior is different for GNRs. It is evident that the orientation improves significantly with the aid of additional deformation initially (up to 45%). However, after transition to deformation-enhanced dispersion regime ($Pe_0 > 11$) there is a significant deterioration in alignment of GNRs. This behavior can be explained by a more flexible structure of GNRs, which inhomogeneously respond to deformation and are more prone to enlacement and coiling. We speculate that a high initial deformation may cause some of the GNRs

to form coils initially, due to a shorter orientation time scale for different individual parts. It should be mentioned that similar behavior was observed in our MD simulation of flexible axisymmetric NPs, which is discussed in more details in the next later section. Controlling the alignment of axisymmetric nanoinclusions can be utilized to tune and enhance thermal conductivity of nanocomposite if NPs are well aligned, or electrical conductivity if they are disoriented.

It is worthy to note that our empirical observations are supported by the results from the Li-ion battery anode performance and MD simulation that are discussed in later sections. We further confirm that the utilization of a circumferentially uniform sheath layer air flow in GAES allows to effectively control the spatial distribution and orientation of CNTs and GNRs. This approach provides a simple but robust single-step procedure to manufacture multifunctional nanocomposites, and obviates the use of surface functionalization. Successful utilization of this methodology would be exceptionally useful for the energy storage media application, where active material functionalization may result in a retardation of some essential properties.
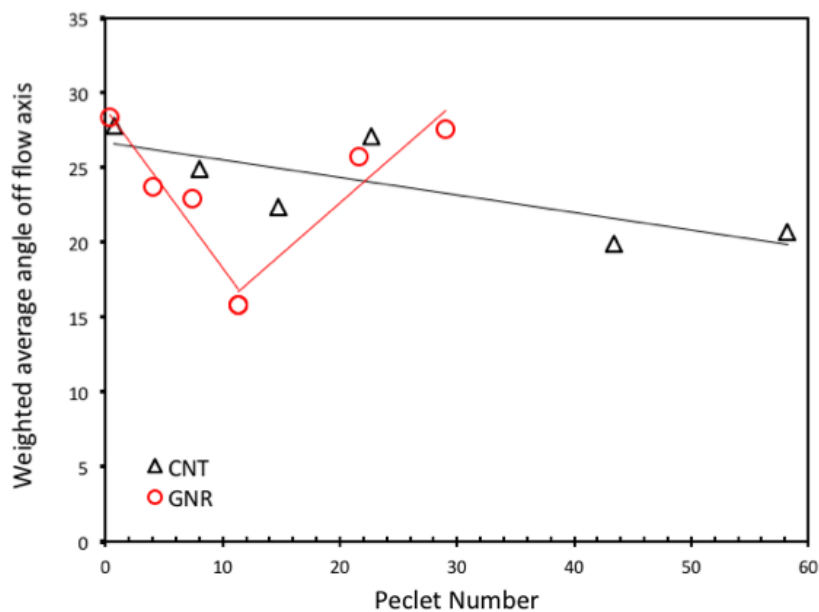


Figure 3.4. Alignment analysis results for ES and GAES (2.5, 4, 5.5, 9, 11 SCFH) of CNTs and GNRs (5 vol% to PVA) in nanofibers.

### 3.3.2. *Non-equilibrium coarse-grained molecular dynamics*

In order to investigate the effect of the strong extensional strains present during the electrospinning process on the placement of the GNR and CNT additives, we simulated an ideal system of CNT and GNR in a polymer melt using non-equilibrium coarse-grained molecular dynamics. In the simulation, the CNT and GNR materials are idealized as nanorods with different stiffness and aspect ratios. The nanorod stiffness was controlled by a constant k in a harmonic angle potential, where a larger k corresponds to a stiffer nanorod (CNT), and the aspect ratios 10 and 16 were chosen to match those used in experiment. The extensional strain was approximated as planar elongational strain, which has the advantage of allowing infinite-time simulations.

Aggregation results are shown in Figure 3.5 by measuring the average number of near nanorod neighbors. A state where the nanorods are aggregated will have a larger number of near neighbors, while a disperse state will have a low number. In these simulations, a value of around 5 represents a fully dispersed state while a value of around 30 corresponds to a fully aggregated state. [44]

Increasing strain rates results in much higher dispersion of the nanorods. This is due to the strong convective effect overpowering the random diffusive motion that causes the nanorods to meet and aggregate. The strain also tends to align the nanorods towards the extension direction, shown in Figure 3.6, reducing their profile and restricting aggregation. Stronger strain also destabilizes large aggregates by imposing a velocity gradient across the aggregate, breaking them apart.

The effect of the chain stiffness can be seen in the early time behavior. For an equal strain rate, the stiffer chains aggregate more slowly. This can be explained by their better alignment to

the extension direction, resulting in less contact between nanorods and slower aggregation. At long times, the stiffer nanorods reach comparable aggregation as the more flexible nanorods.

The aspect ratio appears to have a relatively small affect. The long-time aggregation is slightly higher for the longer nanorods, which is expected due to the greater effect on the number of near neighbors when two longer chains encounter each and aggregate.

Figure 3.6 shows the alignment of the nanorods to the extension direction, which helps to explain the aggregation behavior. At the highest strain rate, el = 0.1, both the flexible and rigid nanorods are well aligned to the extension direction. The elongational strain provides a driving force for the nanorods to align towards the extension direction, but the degree of response is affected by the chain stiffness. This is seen especially for the flexible nanorods, where only the highest strain rate is enough to well align the chains. Lower strain rates do not apply enough of a driving force to fully overcome entanglement and random motion effects. However, the stiffer nanorods are well aligned for all strain rates. While the flexible nanorods can bend to accommodate the effects of the strain, an unaligned rigid nanorod will face strong forces from the strain that propagate through the rigid chain. In the case of the $k = 1$ nanorods at the lowest strain rate, $el =$ 0.01, the weak convection results in a much slower alignment of the nanorods.

Diffusion coefficients in Lennard-Jones units for the simulated nanorods were calculated from equilibrium (no strain) simulations case to help explain the differences in transport behavior between CNT and GNR.

The longer chains have lower translational and rotational diffusion coefficients, as expected from basic transport theory. The stiff nanorods, unable to easily move within the entangled polymer melt, show much lower diffusion coefficients than their flexible counterparts. This also contributes to the slower aggregation of the more rigid nanorods.
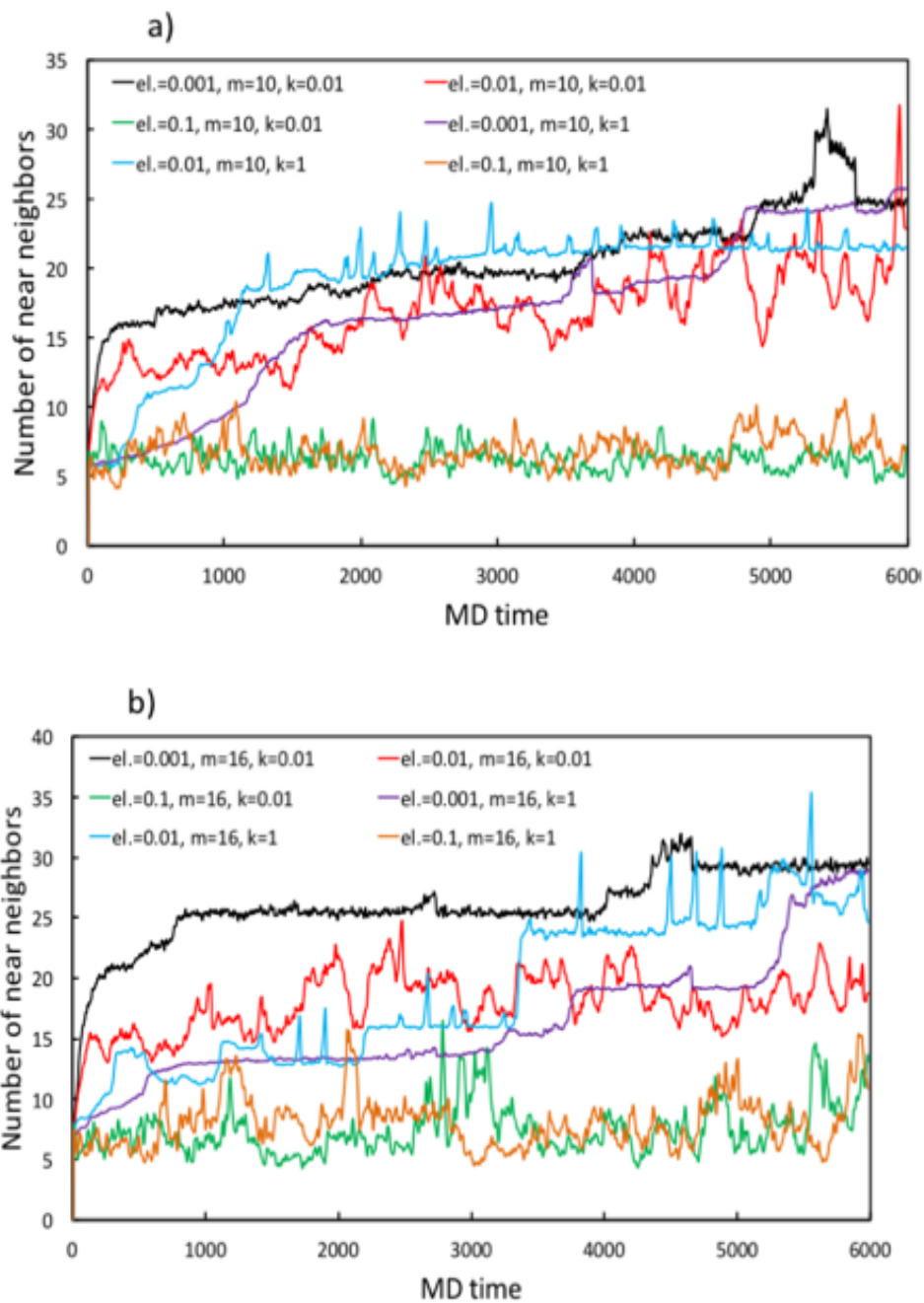
Figure 3.5. CGMD simulation results for aggregation of nanorods with varying aspect ratio a) m=10, b) m=16, chain stiffness (k), and strain rate (el). The concentration of nanorods is kept at 2%.
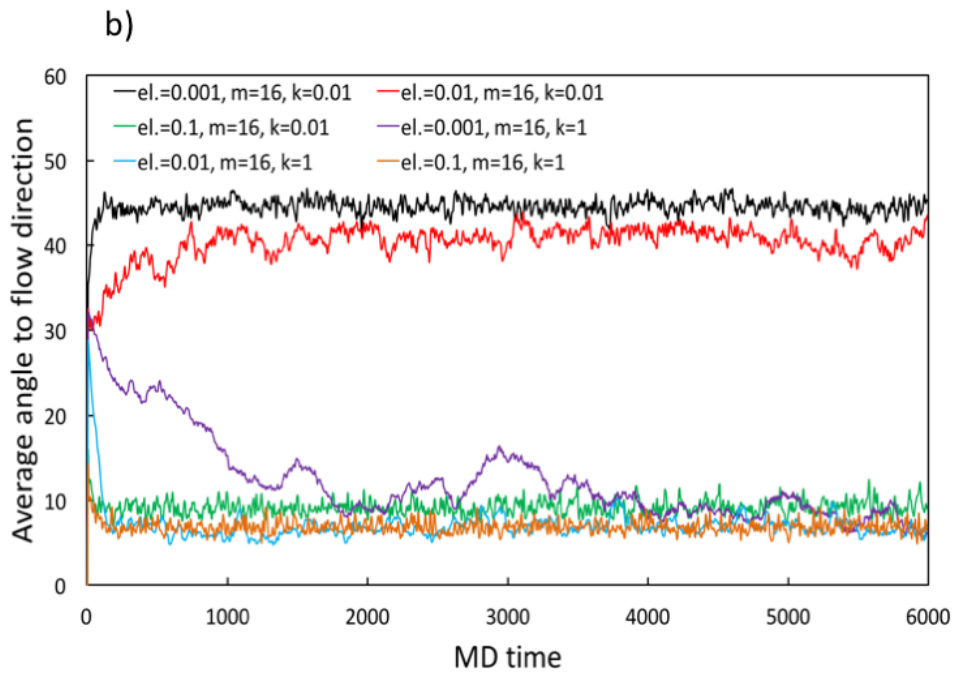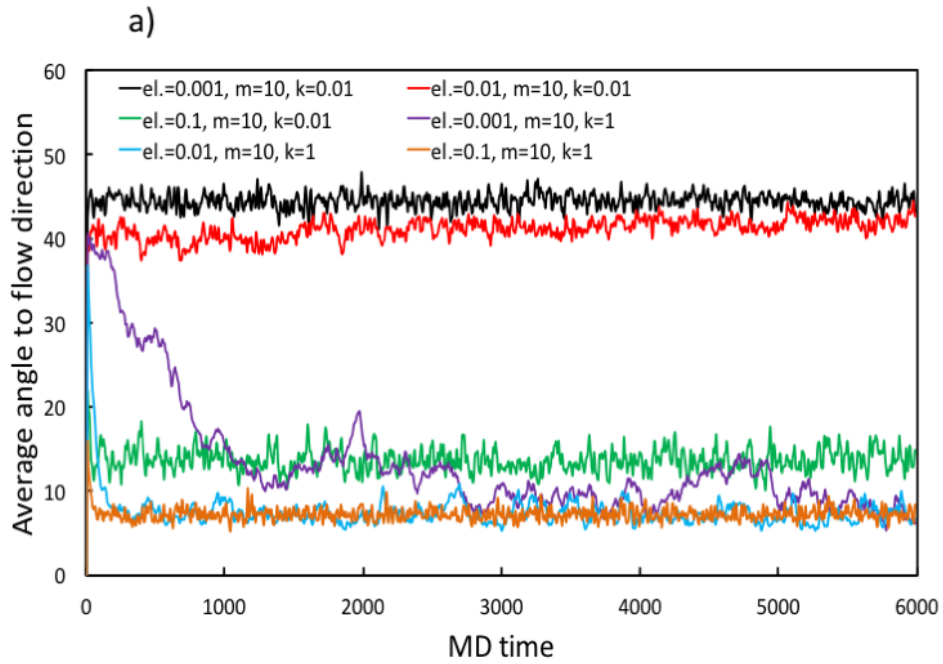
Figure 3.6. CGMD simulation results for alignment of nanorods to the extension direction for varying aspect ratio a) m=10, b) m= 16, chain stiffness (k), and strain rate (el). The concentration of nanorods is kept at 2%.

It has been shown in Chapter 2 (Figure 2.12), that the control of spatial distribution of active material leads to significant improvement of Li-ion battery anode performance. In this chapter, we confirmed that the placement and orientation of anisotropic conductive nanoinclusions can be precisely tuned to create effective conductive pathways for Li ions and maximize the surface area for electrochemical reactions. It can be concluded that the synergistic effect of improved dispersion due to additional extensional deformation, and better enthalpic interaction between anisotropic CNTs and spherical Si NPs galvanize the enhancement of electrochemical performance.

## 3.4. Summary

In this work, we demonstrated a robust methodology to control the dispersion and alignment of unfunctionalized anisotropic nanoinclusions in polymer nanofibers. Our results show that the additional extensional deformation provided by the sheath layer air flow during gas-assisted electrospinning enhances spatial distribution and orientation of nanofillers in resulting polymer fibers. The effect of additional extensional deformation was investigated for PVA solutions with CNTs and their unzipped counterparts – GNRs at different loadings. Solutions were spun into fibers utilizing conventional electrospinning and GAES at different air flow rates. Resulting fibers were microtomed, and longitudinal sections were analyzed using TEM. In order to quantify dispersion and orientation improvement we utilized three image analysis techniques that were previously developed in our laboratory. Our results demonstrate an average of 60 and 90 percent improvement in dispersion area, and 50 and 60 percent improvement in separation between individual nanoparticles and agglomerates due to the application of high but controlled air flow for CNTs and GNRs respectively. We further performed a simple time scale analysis that indicated that deformation-induced rupture is the dominant homogenizing mechanism. It has been shown

that CNTs require 2-3 times higher extensional deformations to disperse, compared to GNRs, which can be explained by increased stiffness, stronger cohesive forces and no surface functionalization. Alignment analysis results show that CNTs respond uniformly to extensional deformation and orient along the fiber spinning axis with the increase of the air flow. However, GNRs undergo alignment worsening at higher air flows, potentially due to inhomogeneous response to deformation, therefore coiling and enlacement. All the empirical observations in the current study were qualitatively confirmed by non-equilibrium coarse-grained molecular dynamics. This work is the extension of our study on dispersion of spherical nanoinclusions, and to the best of our knowledge this is the first attempt to successfully control the placement and orientation of anisotropic nanofillers in polymer nanocomposites by tuning the driving force of the fabrication process. The proposed approach offers a facile but robust single-step technique to produce functional fibrous nanocomposites obviating prior surface functionalization. Therefore, its successful utilization can revolutionize the field and lead to the next generation materials, especially in energy storage media applications, where active material functionalization may hinder some of the most important properties. In Chapter 4, we present a novel air-controlled electrospraying process, which is an extension of gas-assisted electrospinning, and a robust method to manufacture coatings with precisely controllable nanoscale topology, morphology, deposition thickness, and spatial distribution of unfunctionalized NPs.

## REFERENCES

[1]     Y. Zhmayev, S. Pinge, G. Shoorideh, G. L. Shebert, P. Kaur, H. Liu, and Y. L. Joo, "Controlling the Placement of Spherical Nanoparticles in Electrically Driven Polymer Jets and its Application to Li-Ion Battery Anodes," *Small*, pp. 1–11, 2016.

[2]     J. H. Park and Y. L. Joo, "Tailoring nanorod alignment in a polymer matrix by elongational flow under confinement: simulation, experiments, and surface enhanced Raman scattering application.," *Soft Matter*, vol. 10, pp. 3494–3505, 2014.

[3]     A. C. Balazs, T. Emrick, and T. P. Russell, "Nanoparticle Polymer Composites: Where Two Small Worlds Meet," *Science*, vol. 314, no. 5802, pp. 1107–1110, 2006.

[4]     L. Brus, "Quantum crystallites and nonlinear optics," *Appl. Phys. A Solids Surfaces*, vol. 53, no. 6, pp. 465–474, 1991.

[5]     E. P. Giannelis, "Polymer layered silicate nanocomposites," *Adv. Mater.*, no. 1, pp. 29–35, 1996.

[6]     M. R. Bockstaller, R. A. Mickiewicz, and E. L. Thomas, "Block copolymer nanocomposites: Perspectives for tailored functional materials," *Adv. Mater.*, vol. 17, no. June 2015, pp. 1331–1349, 2005.

[7]     Y. S. Kim, G. Shoorideh, Y. Zhmayev, J. Lee, Z. Li, B. Patel, S. Chakrapani, J. H. Park, S. Lee, and Y. L. Joo, "The critical contribution of unzipped graphene nanoribbons to scalable silicon-carbon fiber anodes in rechargeable Li-ion batteries," *Nano Energy*, vol. 16, pp. 446–457, 2015.

[8]     M. J. O'Connell, *Carbon Nanotubes: Properties and Applications*. Boca Raton, 2006.

[9]     R. Andrews and M. C. Weisenberger, "Carbon nanotube polymer composites," *Curr. Opin. Solid State Mater. Sci.*, vol. 8, no. 1, pp. 31–37, 2004.

[10]  R. Yi, F. Dai, M. L. Gordin, S. Chen, and D. Wang, "Micro-sized si-c composite with interconnected nanoscale building blocks as high-performance anodes for practical application in lithium-ion batteries," *Adv. Energy Mater.*, vol. 3, no. 3, pp. 295–300, 2013.

[11]  R. Yi, F. Dai, M. L. Gordin, H. Sohn, and D. Wang, "Influence of silicon nanoscale building blocks size and carbon coating on the performance of micro-sized si-c composite li-ion anodes," *Adv. Energy Mater.*, vol. 3, no. 11, pp. 1507–1515, 2013.

[12]  L.-F. Cui, L. Hu, J. Wook, and Y. Cui, "Light-Weight Free-Standing Carbon Lithium Ion Batteries," *ACS Nano*, vol. 4, no. 7, pp. 3671–3678, 2010.

[13]  W. Wang and P. N. Kumta, "Nanostructured Hybrid Silicon/Carbon Nanotube Heterostructures: Reversible High-Capacity Lithium-Ion Anodes," *ACS Nano*, vol. 4, no. 4, pp. 2233–2241, 2010.

[14]  S. H. Liao, C. C. Weng, C. Y. Yen, M. C. Hsiao, C. C. M. Ma, M. C. Tsai, A. Su, M. Y. Yen, Y. F. Lin, and P. L. Liu, "Preparation and properties of functionalized multiwalled carbon nanotubes/polypropylene nanocomposite bipolar plates for polymer electrolyte membrane fuel cells," *J. Power Sources*, vol. 195, no. 1, pp. 263–270, 2010.

[15]  C. F. Kuan, H. C. Kuan, C. C. M. Ma, and C. H. Chen, "Mechanical and electrical properties of multi-wall carbon nanotube/poly(lactic acid) composites," *J. Phys. Chem. Solids*, vol. 69, no. 5–6, pp. 1395–1398, 2008.

[16]  H. Huang, C. Liu, Y. Wu, and S. Fan, "Aligned carbon nanotube composite films for thermal management," *Adv. Mater.*, vol. 17, no. 13, pp. 1652–1656, 2005.

[17]  D. V Kosynkin, A. L. Higginbotham, A. Sinitskii, J. R. Lomeda, A. Dimiev, B. K. Price, and J. M. Tour, "Longitudinal unzipping of carbon nanotubes to form graphene nanoribbons.," *Nature*, vol. 458, no. 7240, pp. 872–876, 2009.

[18] A. Sinitskii, A. A. Fursina, D. V. Kosynkin, A. L. Higginbotham, D. Natelson, and J. M. Tour, "Electronic transport in monolayer graphene nanoribbons produced by chemical unzipping of carbon nanotubes," *Appl. Phys. Lett.*, vol. 95, no. 25, pp. 36–39, 2009.

[19] L. Jiao, X. Wang, G. Diankov, H. Wang, and H. Dai, "Facile Synthesis of High Quality Graphene Nanoribbons," *Nat. Nanotechnol.*, vol. 5, no. April, pp. 321–325, 2010.

[20] J. H. Park, V. Kalra, and Y. L. Joo, "Controlling the dispersion and orientation of nanorods in polymer melt under shear: Coarse-grained molecular dynamics simulation study," *J. Chem. Phys.*, vol. 140, pp. 124903–124920, 2014.

[21] V. Kalra, J. Lee, J. H. Lee, S. G. Lee, M. Marquez, U. Wiesner, and Y. L. Joo, "Controlling nanoparticle location via confined assembly in electrospun block copolymer nanofibers," *Small*, vol. 4, no. 11, pp. 2067–2073, 2008.

[22] V. Kalra, F. Escobedo, and Y. L. Joo, "Effect of shear on nanoparticle dispersion in polymer melts: A coarse-grained molecular dynamics study," *J. Chem. Phys.*, vol. 132, no. 2, p. 24901, 2010.

[23] V. Kalra, S. Mendez, F. Escobedo, and Y. L. Joo, "Coarse-grained molecular dynamics simulation on the placement of nanoparticles within symmetric diblock copolymers under shear flow," *J. Chem. Phys.*, vol. 128, no. 16, p. 164909, 2008.

[24] V. Kalra, F. Escobedo, and Y. L. Joo, "Effect of shear on nanoparticle dispersion in polymer melts: A coarse-grained molecular dynamics study," *J. Chem. Phys.*, vol. 132, no. 2010, pp. 024901–024912, 2010.

[25] G. A. Buxton and A. C. Balazs, "Simulating the morphology and mechanical properties of filled diblock copolymers," *Phys. Rev. E. Stat. Nonlin. Soft Matter Phys.*, vol. 67, no. March, pp. 031802–031814, 2003.

[26]  A. K. Khandpur, S. Forster, F. S. Bates, I. W. Hamley, A. J. Ryan, W. Bras, K. Almdal, and K. Mortensen, "Polyisoprene-Polysterene Diblock Copolymer Phase Diagram near the Order-Disorder Transition," *Macromolecules*, vol. 28, pp. 8796–8806, 1995.

[27]  R. Krishnamoorti and K. Yurekli, "Rheology of polymer layered silicate nanocomposites," *Curr. Opin. Colloid Interface Sci.*, vol. 6, pp. 464–470, 2001.

[28]  M. Kamibayashi, H. Ogura, and Y. Otsubo, "Shear-thickening flow of nanoparticle suspensions flocculated by polymer bridging," *J. Colloid Interface Sci.*, vol. 321, pp. 294–301, 2008.

[29]  S. Srivastava, J. H. Shin, and L. A. Archer, "Structure and rheology of nanoparticle–polymer suspensions," *Soft Matter*, vol. 8, p. 4097, 2012.

[30]  E. Zhmayev, D. Cho, and Y. L. Joo, "Nanofibers from gas-assisted polymer melt electrospinning," *Polymer*, vol. 51, no. 18, pp. 4140–4144, Aug. 2010.

[31]  A. E. Spivak, Y. A. I. Dzenis, and D. H. Reneker, "A model of steady state jet in the electrospinning process," *Mech. Res. Commun.*, vol. 27, no. 1, pp. 37–42, 2000.

[32]  M. M. Hohman, M. Shin, G. Rutledge, and M. P. Brenner, "Electrospinning and electrically forced jets. I. Stability theory," *Phys. Fluids*, vol. 13, no. 8, p. 2201, 2001.

[33]  M. M. Hohman, M. Shin, G. Rutledge, and M. P. Brenner, "Electrospinning and electrically forced jets. II. Applications," *Phys. Fluids*, vol. 13, no. 8, pp. 2221–2236, 2001.

[34]  J. J. Feng, "The stretching of an electrified non-Newtonian jet: A model for electrospinning," *Phys. Fluids*, vol. 14, no. 11, p. 3912, 2002.

[35]  Y. M. Shin, M. M. Hohman, M. P. Brenner, and G. C. Rutledge, "Experimental characterization of electrospinning: the electrically forced jet and instabilities," *Polymer*

(Guildf)., vol. 42, no. 25, pp. 09955–09967, Dec. 2001.

[36]  C. P. Carroll and Y. L. Joo, "Electrospinning of viscoelastic Boger fluids: Modeling and experiments," *Phys. Fluids*, vol. 18, no. 5, p. 53102, 2006.

[37]  P. T. Cummings, B. Y. Wang, D. J. Evans, and K. J. Fraser, "Nonequilibrium molecular dynamics calculation of self-diffusion in a non-Newtonian fluid subject to a Couette strain field," *J. Chem. Phys.*, vol. 94, no. 1991, pp. 2149–2158, 1991.

[38]  S. Sarman, J. Evans, and A. Baranyai, "Mutual and delf-diffusion in fluids undergoing strong shear," *Phys. Rev. A*, vol. 46, no. 2, pp. 893–902, 1992.

[39]  X. Qiu, H. D. Ou-Yang, D. J. Pine, and P. M. Chaikin, "Self-diffusion of interacting colloids far from equilibrium," *Phys. Rev. Lett.*, vol. 61, no. 22, pp. 2554–2557, 1988.

[40]  J. R. Abbott, N. Tetlow, A. L. Graham, S. A. Altobelli, E. Fukushima, L. A. Mondy, and T. S. Stephens, "Experimental observations of particle migration in concentrated suspensions: Couette flow," *J. Rheol. (N. Y. N. Y).*, vol. 35, no. 1991, pp. 773–795, 1991.

[41]  C. J. Koh, P. Hookham, and L. G. Leal, "An experimental investigation of concentrated suspension flows in a rectangular channel," *J. Fluid Mech.*, vol. 266, pp. 1–32, 1994.

[42]  W. Xue and G. S. Grest, "Brownian dynamics simulations for interacting colloids in the presence of a shear flow," *Phys. Rev. A*, vol. 40, no. 3, pp. 1709–1712, 1989.

[43]  C. Chang and R. L. Powell, "Self-diffusion of bimodal suspensions of hydrodynamically interacting spherical particles in shearing flow," *J. Fluid Mech.*, vol. 281, pp. 51–80, 1994.

[44]  B. D. Todd and P. J. Daivis, "New algorithm for unrestricted duration nonequilibrium molecular dynamics simulations of planar elongational flow," *Comput. Phys. Commun.*, vol. 117, no. 3, pp. 191–199, 1999.

[45]  A. M. Kraynik and D. A. Reinelt, "Extensional motions of spatially periodic lattices," *Int.*

J. *Multiph. Flow*, vol. 18, no. 6, pp. 1045–1059, 1992.

[46]  B. D. Todd and P. J. Daivis, "The stability of nonequilibrium molecular dynamics simulations of elongational flows," *J. Chem. Phys.*, vol. 112, no. 1, pp. 40–46, 2000.

[47]  F. Zhang, D. J. Searles, D. J. Evans, J. S. D. T. Hansen, D. J. Isbister, D. J. Searles, and D. J. Evans, "Kinetic energy conserving integrators for Gaussian thermostatted SLLOD," *J. Chem. Phys.*, vol. 111, no. 1, pp. 18–26, 1999.

[48]  M. L. Matin, P. J. Daivis, and B. D. Todd, "Comparison of planar shear flow and planar elongational flow for systems of small molecules," *J. Chem. Phys.*, vol. 113, no. 20, p. 9122, 2000.

[49]  W. Bruns and R. Bansal, "Molecular dynamics study of a single polymer chain in solution," *J. Chem. Phys.*, vol. 74, no. 3, pp. 2064–2072, 1979.

[50]  J. D. Weeks, D. Chandler, and H. C. Andersen, "Role of Repulsive Forces in Determining the Equilibrium Structure of Simple Liquids," *J. Chem. Phys.*, vol. 54, no. 12, p. 5237, 1971.

[51]  M. J. Park, K. Char, J. Park, and T. Hyeon, "Effect of the Casting Solvent on the Morphology of Poly ( styrene-b-isoprene ) Diblock Copolymer / Magnetic Nanoparticle Mixtures," *Langmuir*, vol. 22, no. 4, pp. 10–13, 2006.

# CHAPTER 4

# CONTROLLING SPATIAL DISTRIBUTION OF ACTIVE NANOINCLUSIONS AND SURFACE MORPHOLOGY/TOPOLOGY IN FUNCTIONAL COATINGS VIA NOVEL AIR-CONTROLLED ELECTROSPRAYING PROCESS

## 4.1. Introduction

Controlling surface topology, morphology and dispersion of active nanoinclusions plays a crucial role in manufacturing of functional coatings for different applications, such as superhydrophobic materials [1–3], biomedical devices [4, 5] and energy storage media [6–13]. There is a plethora of methods currently being investigated for efficient coating fabrication. Chemical vapor deposition [14], physical vapor deposition [15, 16], plasma-spraying [17], dip-coating [18, 19] and spin-coating [19, 20] are a few examples of the most mature methods. However, these techniques suffer from low and non-uniform deposition rates, poor control of surface topology, low deposition efficiency, difficulty to develop a continuous process, as well as to cover large and complicated architectures. [4, 10]

Recently, conventional electrospraying method received a lot of attention, due to its facile controllability and capability to alleviate some of the above-mentioned drawbacks. [1, 3–6, 10], [11, 21–28] During electrospraying process a liquid is pumped through a capillary nozzle into a high-voltage electric field, where electrical forces overcome surface tension forces and a pendular droplet takes a conical shape, which is commonly referred to as a Taylor cone. [21, 23] The charged cone soon becomes unstable and breaks into fine droplets that rapidly subdivide due to secondary breakup, called Coulombic fission. [29] The size of the droplets can be controlled via electrospraying conditions, and ranges between hundreds of micrometers to several nanometers. In the final stage of spraying a mist of fine charged droplets is deposited on a grounded collector

in the form of a film. It should be mentioned that charged droplets are self-dispersing in space and monodisperse. The control of the droplet size and solvent evaporation rate determines the quality of the coating, as well as topological and morphological characteristics. [6, 10, 21, 23]

It has been shown that electrospraying approach is superior to alternative techniques for direct deposition of active materials on current collectors, and offers a powerful single-step procedure for electrode fabrication. [6] Nanomaterials, such as silicon nanoparticles (NPs) [30–37], metal oxides ($SnO_2$, $CoO$, $Fe_2O_3$) [6, 7, 11, 12] and conductive carbon (carbon nanotubes (CNTs), graphene nanoribbons (GNRs), carbon black (CB)) [35, 38, 39], are generally used to improve electrode performance. In particular, due to enhanced surface interaction with electrolyte, shorter diffusion length for Li ions and electrons, mitigation of the volume change effects, and feasibility of fully reversible reactions. [6, 35] However, all the above-mentioned advantages can be concealed if nanomaterials are improperly incorporated into the electrode architecture, and their spatial distribution and orientation is not precisely controlled. [6, 35, 39] In this case, it is essential to have a way to directly manufacture and coat nanomaterials pre-mixed in a binder, rather than dispersing them in a separate step.

Techniques, such as vapor deposition [14, 15], sputtering [40], electrodeposition [41] are used to decrease the number of process steps, but in all these examples conductive additives and binders are not added in the final electrodes. In contrast to conventional deposition methods, that require multiple steps, high temperatures, toxic solvents and thorough mixing in a slurry, electrospraying obviates any tedious procedures and offers a significant cut down on time. [21, 23] However, significant challenges still exist, particularly in the attempts to increase the throughput, further control fluid atomization, tune the deposition thickness and nanoscale topology, as well as dispersion and orientation of functional nanoinclusions in resulting coatings.

91

In our recent studies, we have introduced a novel and systematical procedure to control dispersion and orientation of unfunctionalized spherical and anisotropic NPs in polyvinyl alcohol (PVA) nanofibers for Li-ion Battery anode application. [39] In this work, we are taking a step forward, and extending our knowledge to a novel air-controlled (AC) electrospraying process, which is a powerful and efficient technique to produce coatings with precisely controllable nanoscale topology, morphology, deposition thickness, and spatial distribution of active nanoinclusions. The AC-electrospraying process utilizes an additional extensional deformation applied on the fluid during the initial stage of atomization by applying a circumferentially homogeneous and controlled air flow through an outer layer of coaxial nozzle. [39, 42] This deformation tunes the atomization mechanism by yielding bending instability, and overcomes the cohesive forces between nanoinclusions due to additional shearing and elongation. This robust approach allows a precise control of fluid atomization, uniformity of deposition and dispersion of nanoinclusions in the coating without chemical surface functionalization. [39, 43–47] It should be mentioned that AC-electrospray offers a tenfold increase in production rate per nozzle compared to conventional electrospraying, which gives a potential for industrial utilization.

In the current study, we produced CNT and CB loaded PVA coatings utilizing AC-electrospraying at different air flow rates (0, 20, 30, 35, 40 and 45 psi), and focused on the experimental visualization of the onset of atomization. The initial atomization behavior can elucidate the interplay between surface tension, viscous, electrical and aerodynamic forces acting on the Taylor cone and the droplet, and reveal some information about the novel atomization mechanism.

We further investigated the effect of additional deformation on the deposition homogeneity and the dispersion of carbon NPs in resulting coatings, as it plays a crucial role for energy-storage

applications. [6] Active nanomaterials exhibit strong cohesive interactions and actively agglomerate in a binder matrix that offers little affinity. [39, 43–47] There is a plethora of methods for chemical surface modification to increase the affinity between the dispersant and dispersion media. [48, 49] Nevertheless, such manipulations can cause impairment of inherent material properties. For example, chemical functionalization of carbon nanotubes disrupts $\pi$-conjugation and results in a significant loss of electrical conductivity. [45, 50–52] As it has been earlier shown, the agglomeration time scale of various unfunctionalized NPs can be increased by elongating or shearing the fluid [39, 43], and in the current study we demonstrate that this methodology applies to AC-electrospray process.

Carbon inclusions are kinetically immobilized in solidified polymer matrix upon deposition, which is beneficial for the post process analysis. In this study, we utilized scanning electron microscopy (SEM) and transmission electron microscopy (TEM) to examine the effect of the assisting air-flow on the coating topology/morphology and dispersion of carbon additives, respectively. Further, the ability to control deposition thickness and yield was confirmed by measuring the deposit mass and film depth as a function of the air flow rate.

Finally, to mitigate surface charging issues, which can potentially inhibit thin-film deposition on insulating materials, we utilized an AC driving potential [27, 28], and developed an alternating current air-controlled (AC$^2$) electrospraying process. Alternating current allows atomization of charged droplets with changing polarities, which results in charge neutralization in the deposited coating. AC$^2$ electrospray offers additional control of fluid atomization via changing frequency and the wave form, as well as alleviates scalability constraints by utilizing a multi-jet mode, which allows the 600% enlargement of the spinneret diameter.

To the extent of our knowledge, this is a first successful attempt to control fluid atomization and dispersion of functional nanoinclusions in coatings by electrical and aerodynamic forces in synergy. From the application perspective, it is important to accentuate that we unveil a powerful, but easily-scalable single-step coating fabrication technique, which can be effectively utilized in modern research and technology.

## 4.2. Experimental section

*Materials:* Coatings were fabricated using 88% mole Hydrolyzed Polyvinyl alcohol (Mw=25,000 g mol$^{-1}$), purchased from Polysciences, Inc, small multi-wall CNTs provided by EMD, and TIMCAL Graphite & Carbon Super P® Conductive Carbon Black. Transmission electron microscopy and image analysis were carried out to measure the average dimensions and aspect ratios of nanoinclusions.

*Coating fabrication and visualization:* 3% PVA/H$_2$O solution containing 5-15 vol.% CNTs or CB was prepared and sprayed via conventional electrospraying and AC-Electrospraying at 0, 5, 10, 20, 30, 35, 40, and 45 psi, air flow rate. The infusion rates for electrospraying and AC-electrospraying were 0.005 and 0.06 ml min$^{-1}$ respectively, and the electric field was kept constant at 100 kV m$^{-1}$ for both processes. The electrospraying and AC-electrospraying setups are depicted in Figure 4.1, and are similar to electrospinning setups that were utilized in our previous work. [39, 42]

Experimental visualization was performed with a high-speed camera (RedLake MotionPro HS-3 with Nikon MICRO NIKORR 60 mm 1:2:8 lens). The high-speed camera was operated at 1000 frames per second, and acquired images were digitized utilizing MotionStudio software. Illumination was supplied with a 500 W lamp with light dispersing material. [53]

*Coating characterization:* Coating morphology, topology and thickness were characterized using scanning electron microscopy (Tescan Mira3 FESEM). Further, ultrathin coatings (0.2 mL target volume of PVA-CNT/CB, 5 % vol. NP to PVA) were collected on the hexagonal copper grid and analyzed under a Tecnai T12 transmission electron microscope (TEM) that operated at 120 kV. Resulting TEM images were analyzed using MATLAB 2014R and ImageJ.
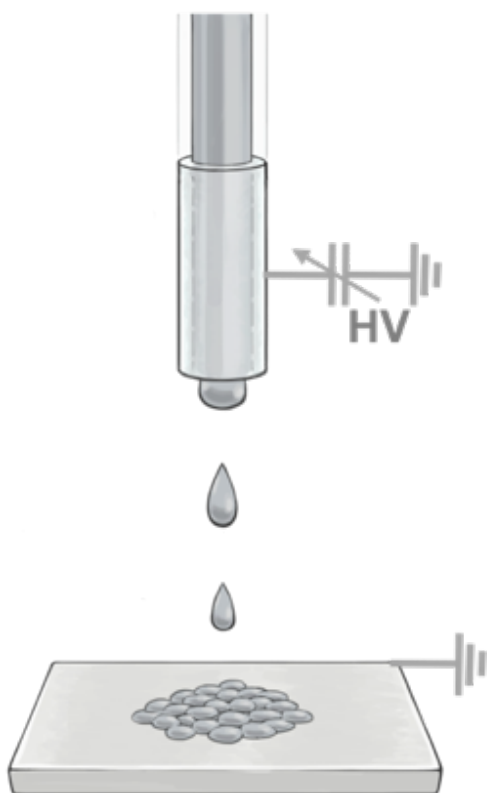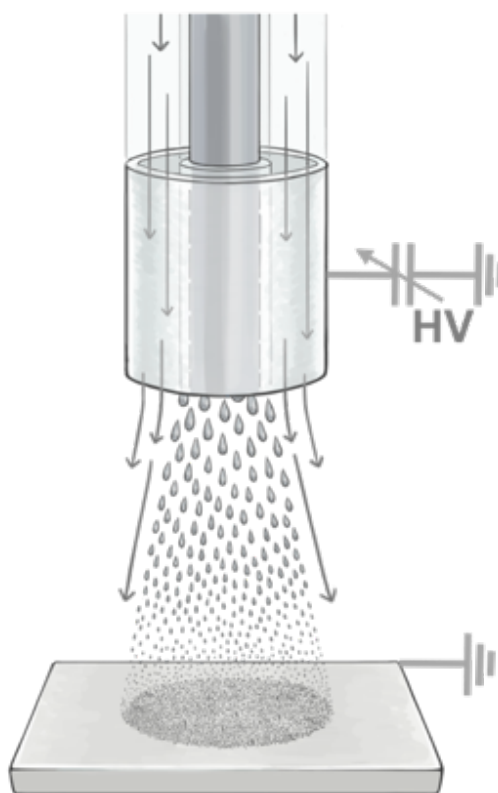


Figure 4.1. Conventional electrospray and AC-electrospray setup schematics

## 4.3. Results and discussions

### 4.3.1. *Controlling atomization mechanism via AC-electrospraying*

Figure 4.2 shows high-speed camera images of the onset of atomization during conventional electrospraying (Figure 4.2 A) and air-controlled electrospraying of PVA solution at different air flow rates (Figure 4.2 B and Figure 4.2 C). It can be seen, that applying a sheath layer air flow will result in alternation of atomization mechanism evident from the change of the Taylor cone geometry and further emergence of bending instability, which is commonly referred to as a "whipping motion". [54, 55] It should be mentioned that this instability, initiated by electrostatic repulsion, is not observed in conventional electrospraying process, and becomes more vigorous with the increase of the air flow rate.
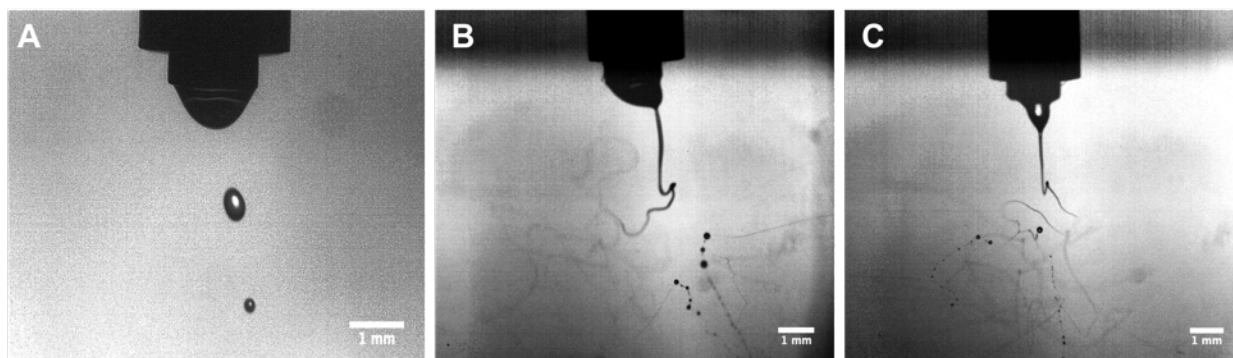


Figure 4.2. High-speed camera images of the onset of atomization during A) Conventional electrospray, and AC-electrospray at B) 5 psi and C) 10 psi sheath-layer air flow

This behavior can be comprehended by studying the additional shearing and extensional deformation on the surface of the polymer solution provided by the sheath layer air flow during the initial stage of spraying. It has been previously shown that there is a two orders of magnitude increase in strain due to the assisting air flow at the tip of the spinneret, which results in sufficient

thinning and acceleration of the polymer jet, as well as an air drag reduction. [39, 42] Once the polymer jet is thin enough, there is a sufficient charge accumulation on the fluid surface, which triggers an immediate repulsive response to the applied electric field in a form of bending instability. During whipping motion the polymer jet is further elongated, which rapidly decreases its diameter, and finally breaks into small droplets due to low viscoelasticity and high capillary force (low concentration of PVA solution). Therefore, the droplet diameter during the initial stage of AC-electrospraying was decreased by 60 percent, and doubling the air flow pressure led to additional 60 percent size reduction, as depicted in Figure 4.3 A. It should be mentioned that the droplet size distribution became more uniform utilizing AC-electrospraying, due to a consistent axisymmetric splitting of bending polymer jets (Figure 4.3 B). From a materials application perspective, it is important to note that we are providing a simple, but robust and effective methodology to control fluid atomization at the onset of spraying. Additional deformation through the sheath layer air flow enables the control of the droplet diameter and size distribution, and in conjunction with fluid viscoelasticity modifies the emanation mechanism.
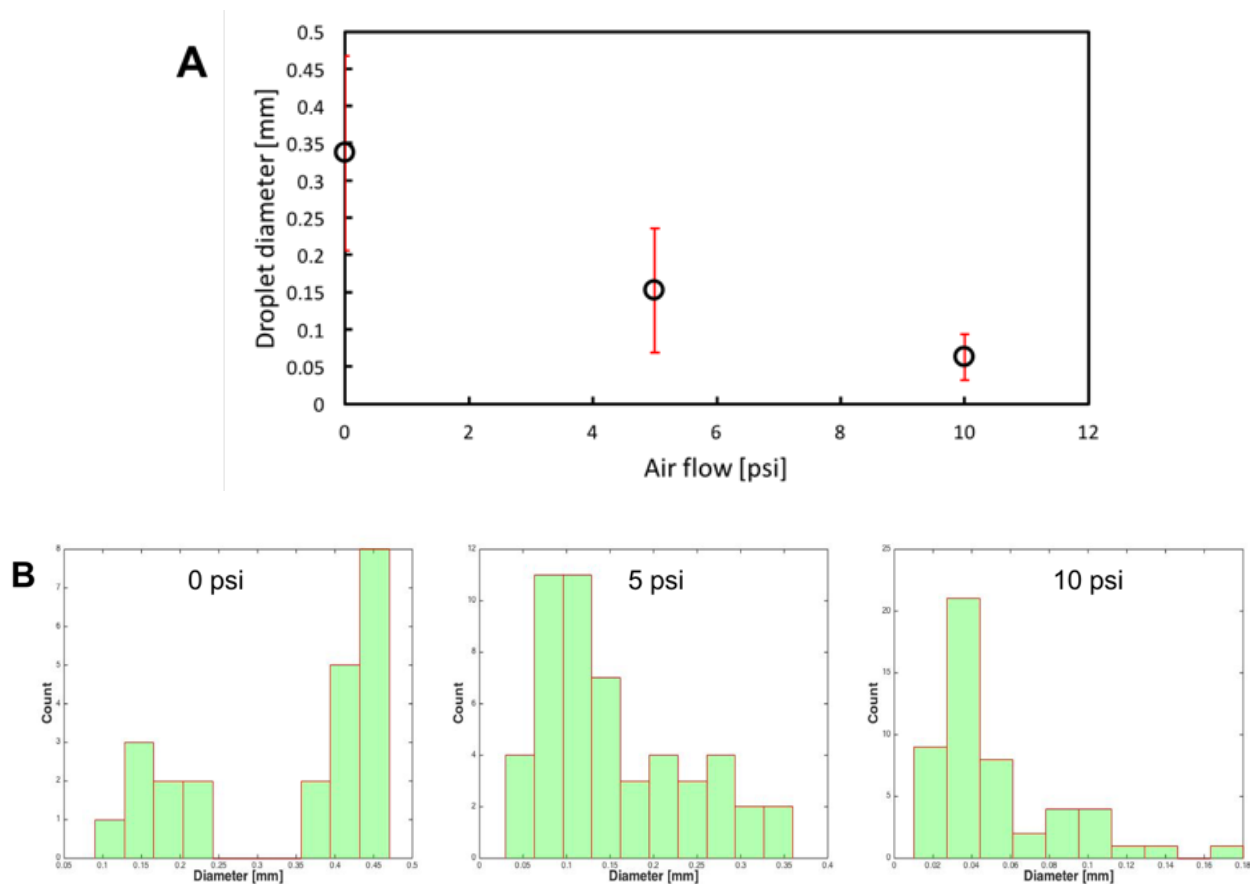
Figure 4.3. Effect of the air flow rate during electrospraying on the fuid atomization. A) size of droplets during atomization and B) droplet size histograms for different air flow rates

### 4.3.2. Controlling coating topology, morphology and nanoparticle dispersion via AC-electrospraying

The effect of the air flow rate on coating deposition and morphology was further tested utilizing PVA/water solution with pre-dispersed carbon materials as a model system. It is important to mention, that target volumes and spraying conditions were kept constant for all experiments, and the only differences were the application of the sheath-layer air flow and higher solution feeding rate in AC-electrospraying. CNTs and CB are commonly used as conductive materials in energy storage applications [35, 38, 39, 56, 57], and their effective placement plays a

crucial role in electrode performance. It should be mentioned that some of the functional nanoinclusions are expensive, so their use must be economical to meet sustainability requirements. Therefore, it is essential to maintain an even and effective deposition, as well as to control NP dispersion and spatial orientation. [35]

Figure 4.4 shows photos of coatings deposited on the glass-slides using conventional electrospray and AC-electrospray at different air flow rates. It is evident that PVA-CB coating deposited via conventional electrospraying displays poor morphology and uneven topology. However, with the application of assisting air flow in AC electrospraying, there is a significant improvement. We can observe some remaining texture on the film deposited by 20 psi AC-electrospraying (Figure 4.4 B), but there are no visible defects at higher air flow rates (Figure 4.4 C and D), due to an effective atomization, as well as directed and precisely-controlled deposition.
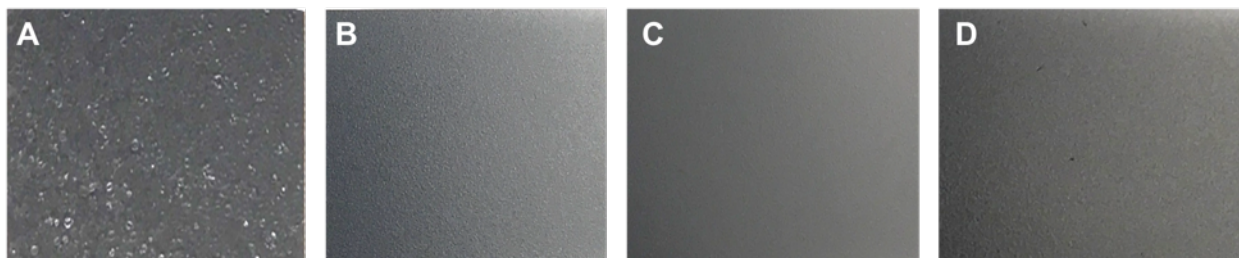


Figure 4.4. Photographs of PVA/CB (15 vol% to PVA) coating over glass slides deposited via A) 0 (Conventional electrospray) at 0.005 mL/min feeding rate, B) 20, C) 35 and D) 45 psi sheath layer air flow AC electrospray at 0.06 mL/min feeding rate

SEM was then utilized to further investigate macro-, micro-, and nano-scale morphologies of the PVA-CB coating deposited via electrospraying at different air flows (Figure 4.5). It is

evident from Figure 4.5 A that there is a significant deviation in size distribution of droplets that are sprayed via conventional electrospray, ranging from 300 $\mu$m (macro-scale) to 50 nm (nano-scale). The solvent evaporation is not precisely controlled in conventional electrospray, which results in deposition of solid polymer particles on the surface, creating rough topology. It can be observed in Figure 4.5 B-D, that with the application of the air flow in AC electrospray, the morphology and topology have significantly improved at all magnifications, due to a precise control over atomization and significant decrease of droplet dimensions. It is important to mention, that the number of solid polymer particles on coating surfaces significantly decreased with the increase of the air flow (Figure 4.5 D,C). The polymer droplets are effectively directed towards the substrate by the air flow, therefore the final solvent evaporation takes place on the surface upon deposition. Extremely high assisting flows result in premature solidification of the droplet, due to forced convection, increasing the number of solid particles on the surface of the coating (Figure 4.5 D). Therefore, AC electrospray can be effectively utilized to precisely control topology and morphology even at nanoscale. This is particularly useful for the development of superhydrophobic coatings, where the control of the surface roughness plays a crucial role and determines wetting angles. [1–3]
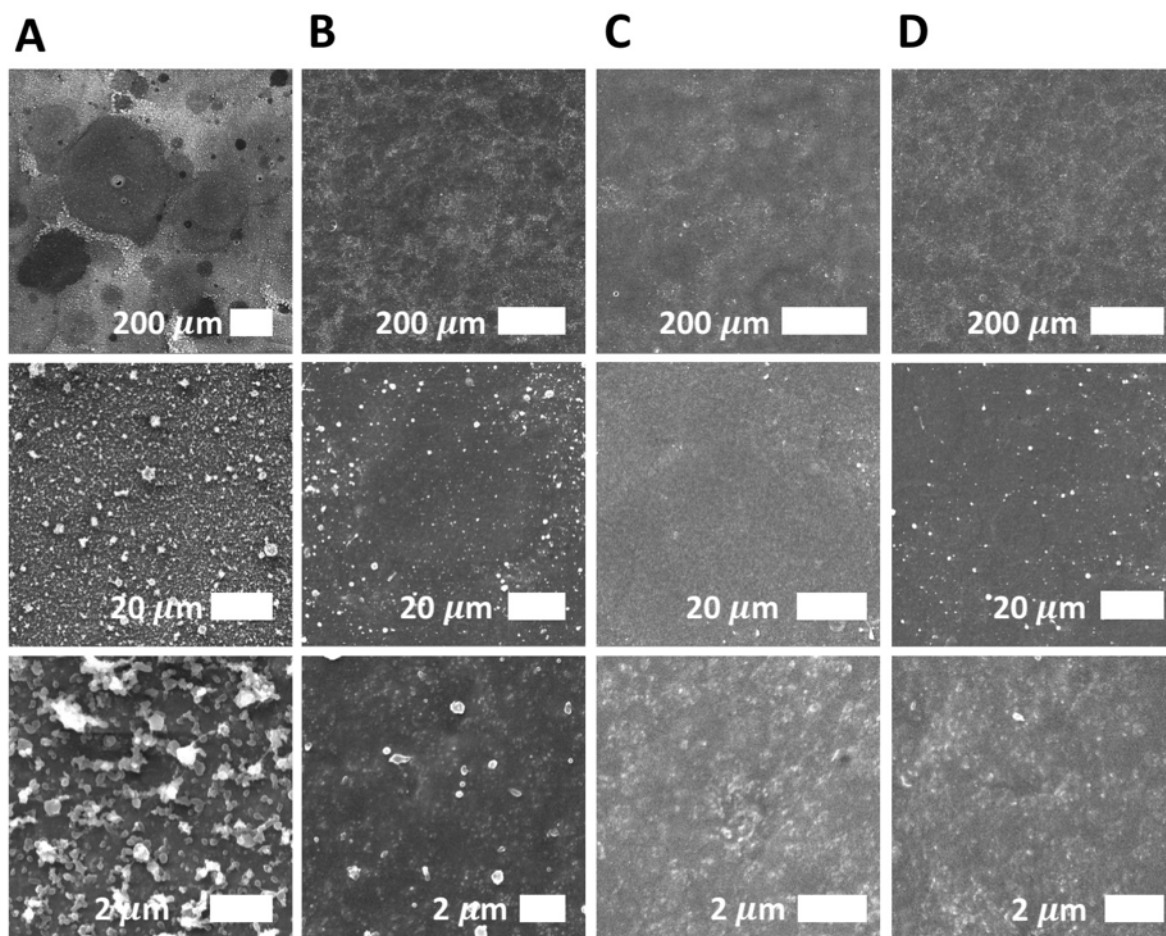
Figure 4.5. SEM images of macro/micro/nano-topology of 3% PVA solution with CB (15 vol% to PVA) coatings deposited via A) 0 (Conventional electrospray), B) 20, C) 35 and D) 45 psi sheath layer air flow AC electrospray.

The deposition efficiency was then calculated for both conventional electrospray and AC-electrospray at intermediate air flow rate (20 psi) based on the comparison of the coating mass deposited on the glass slide (Equation 4.1). The application of assisting air flow resulted in a significant improvement of deposition efficiency from 37% to 96% for conventional electrospraying and AC-electrospraying respectively. This enhancement is an effect brought about by the precise control of the direction and localization of spraying due to the sheath-layer air flow.

$$Coating\ efficiency = \frac{Coating\ mass\ on\ the\ glass\ slide}{Total\ mass\ of\ sprayed\ PVA-NP\ solution} \quad\quad (4.1)$$

Figure 4.6 shows TEM images of PVA-CNT and PVA-CB coatings, directly deposited on copper grids using different air-flow rate electrospraying. It is important to note, that the particle surface is not functionalized, thus the dispersion improvement is not associated with the affinity between nanoinclusions and dispersion media. [39] It can be seen from Figure 4.6 A and Figure 4.6 E that both CNTs and CB particles are prone to form large agglomerates in PVA film deposited with conventional electrospray. However, we can observe a significant improvement in nanoparticle dispersion and agglomerate rupture with the application of high but controlled sheath-layer air flow in AC electrospraying for both CNTs and CB NPs (Figure 4.6 B-D and Figure 4.6 F-H respectively). It can be concluded that this improvement is the result of synergistic effect of two contributors, namely, improved atomization and additional extensional deformation supplied by the air flow during AC electrospraying.

Carbon particles tend to form large flocculates in water-based solutions, due to their hydrophobic nature.[58, 59] Therefore, in the initial stage of spinning, specifically at the onset of the Taylor cone regime, a poor dispersion must be observed. A significant reduction of the droplet size in the initial stage of electrospraying process, due to the bending instability mechanism triggered by the air flow, allows droplets to host less particles and smaller agglomerates. As a result, after further size reduction due to Coulomb fission [29], smaller droplets land on the collector where particles are kinetically "trapped" in a solidified polymer matrix.

The second contribution comes from a significant extensional deformation provided by the sheath layer air flow at the onset of spraying, and vigorous elongation during whipping motion. Extensional forces translate to agglomerates and overcome cohesive forces between individual NPs and their agglomerates, leading to strain-enhanced agglomerate rupture and homogenization

102

within the droplet. [39] Therefore, we can observe a significant enhancement of spatial distribution for both spherical (CB) and anisotropic (CNT) NPs with the increase of the air flow rate in AC-electrospraying. This work is particularly useful for the energy storage applications where particle surface functionalization is detrimental for the properties of active materials. [45, 50–52] For that reason, the development of methods that allow controlling surface topology, morphology and dispersion during a single-step deposition of functional coatings will radically progress the field and cut the cost.
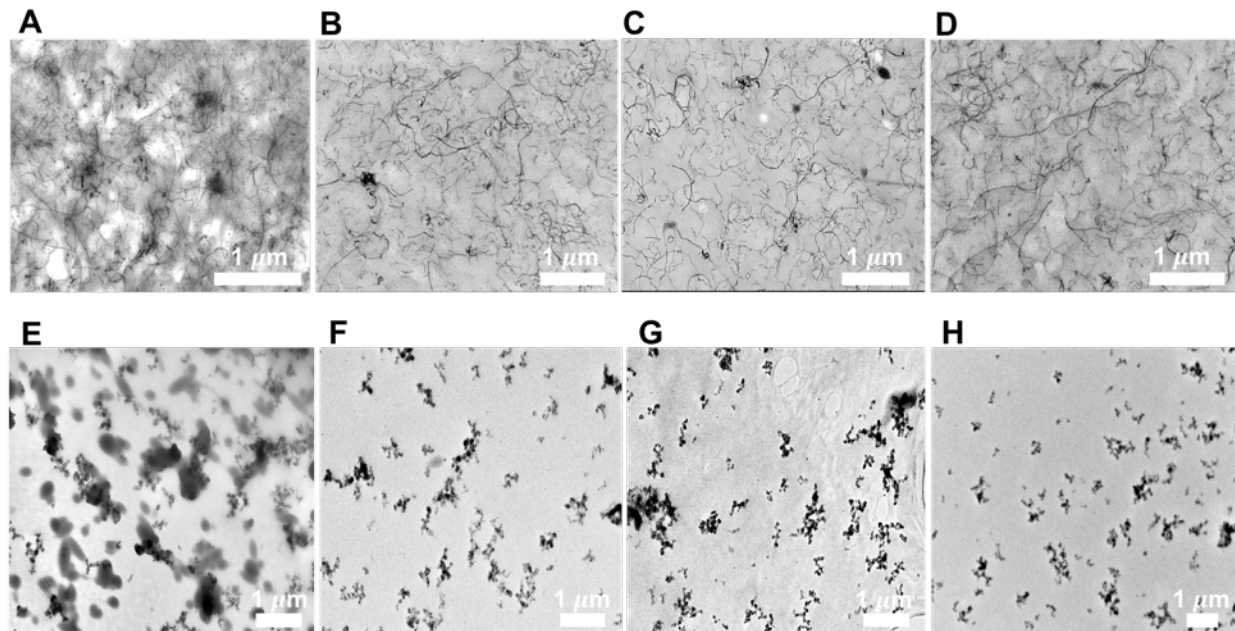


Figure 4.6. TEM images of PVA/CNT and PVA/CB films (5 vol% to PVA) at A, E) 0 psi (Conventional electrospray), B, F) 20 psi, C, G) 30 psi, D, H) 35 psi sheath-layer air flow.

### 4.3.3. Air-controlled alternating current (AC$^2$) electrospray

It has been previously confirmed that conventional electrospraying DC-voltage electrostatic configuration has drawbacks in some applications where a uniform deposition over an insulating substrate is required. The coating retardation and irregularity can be caused by the

surface-charge build-up, which may redirect charged droplets. [27, 28] The alternating current driving potential was previously applied in conventional electrospraying process to mitigate this issue, as it produces droplets with alternating polarity that further self-neutralize. [27, 60] Additionally, it has been previously confirmed that AC-potential adds instability and more effective surface charge accumulation, which triggers a "multi-jet mode" emanation. This allows to produce multiple jets or droplets from the same Taylor cone surface (Figure 4.7 A), and can be used to alleviate scalability constraints. [61]
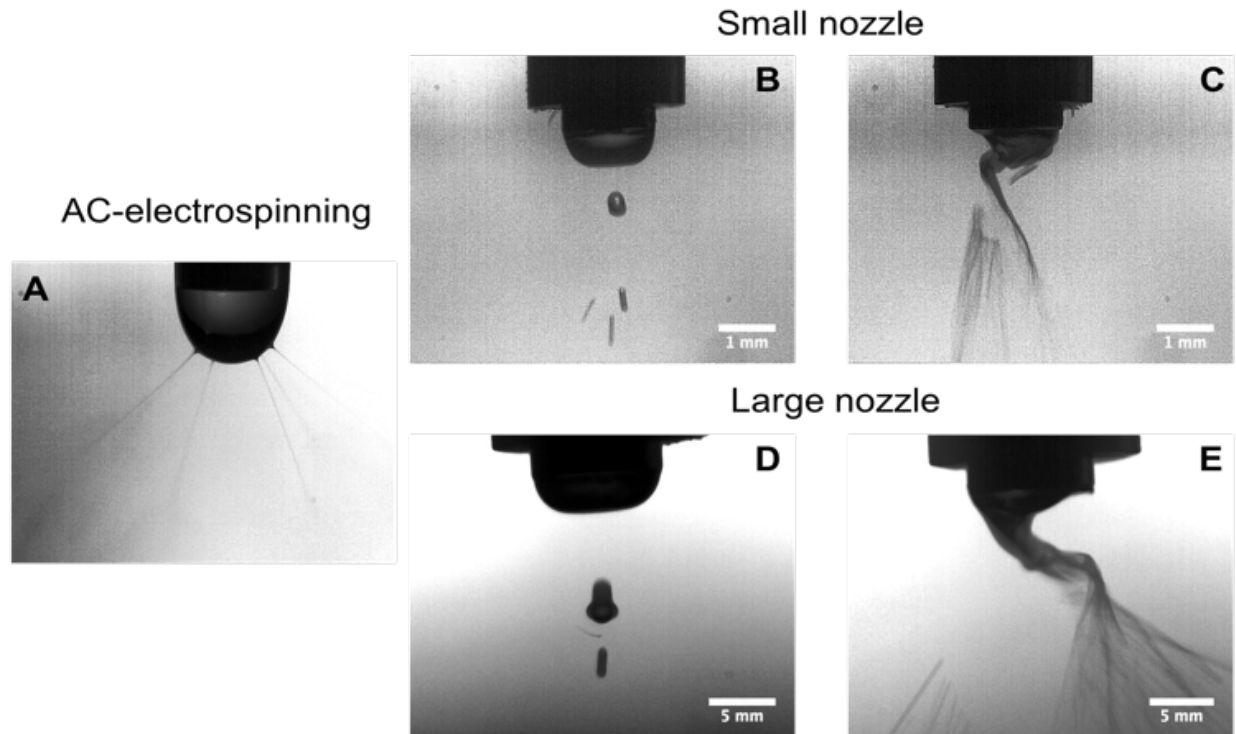


Figure 4.7. High-speed camera images of the onset of fiber/droplet initiation during A) alternating current electrospinning of 10% PVA/$H_2O$, B) alternating current electrospray with small nozzle (1.651 mm I.D.), C) AC$^2$ electrospray with small nozzle (1.651 mm O.D.), D) alternating current electrospray with large nozzle (10 mm O.D.) and E) AC$^2$ electrospray with large nozzle (10 mm O.D.) of 3% PVA/$H_2O$

In the current study, we present a novel $AC^2$ electrospraying process that combines advantages associated with additional controlled air flow and AC potential. Figure 4.7 B and C show high speed camera images of the onset of atomization for conventional alternating-current electrospraying and $AC^2$ elecrospraying, respectively. It can be seen, that conventional alternating-current spraying and conventional DC electrospraing atomization mechanisms are very similar. However, with the application of the sheath layer air flow there is an obvious thinning of the Taylor cone geometry, followed by "multi-jetting" and their vigorous bending instability. Thinning of the Taylor cone favors faster charge accumulation on the fluid surface in multiple locations, followed by jetting and further bending instability. Once the jets are formed, the droplet atomization mechanism in $AC^2$ electrospraying is assumed analogous to its DC-driven counterpart.

The "multi-jetting" behavior was further employed to mitigate scalability limitations via increasing the spinneret diameter by 6 times. Figure 4.7 D and E show high-speed camera images of the onset of atomization for the large nozzle (10 mm in diameter) during alternating-current electrospraying and $AC^2$-electrospraying. It is important to mention, that atomization mechanism remained unaffected, however the production rate was increased by 10-fold.

It can be seen from Figure 4.8 A and B that coating morphology and topology can be controlled and further improved with the application of the air flow in $AC^2$ system. Higher air flow rate benefits fluid atomization and reduces the number of large droplets that result in topological irregularities. It can be seen from Figure 4.8 C that large nozzle $AC^2$-spraying produces decent and uniform coating, however with some roughness and porosity, potentially due to hindered evaporation upon deposition. However, it is possible to adjust experimental conditions to allay these minor issues, and we are currently modifying our apparatus to obtain the most favorable regime. $AC^2$-electrospraying is a powerful method, that allows to effectively control the deposition

process even over insulating substrates due to the droplet-charge neutralization, as well as to significantly upscale coating fabrication.
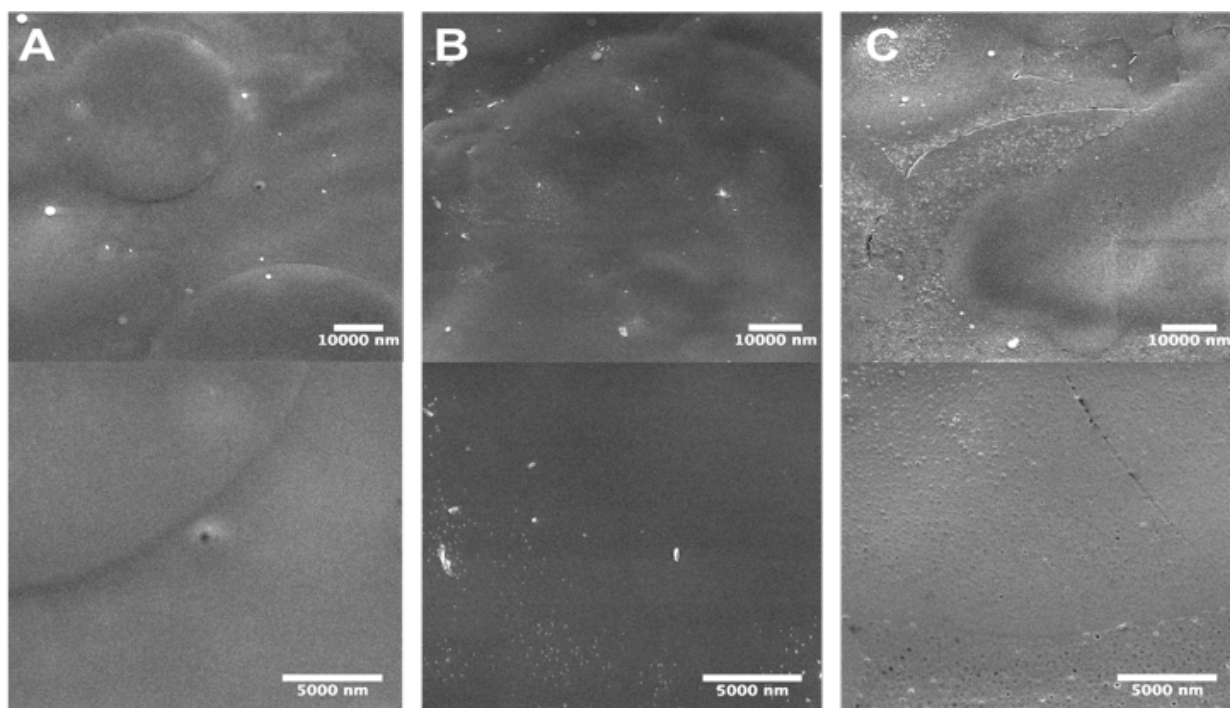


Figure 4.8. SEM images of PVA coatings deposited via alternating current A) electrospray (small nozzle), B) air-controlled electrospray at 10 psi air flow (small nozzle), and C) air-controlled electrospray at 10 psi air flow (large nozzle).

**4.4. Summary**

In this study, we introduced a novel technique to control morphology and topology of functional coatings at nanoscale via the application of the controlled sheath layer air flow through a coaxial spinneret during air-controlled electrospraying. Our results reveal that high but controlled circumferentially uniform air flow can tune the atomization mechanism, by triggering bending instability due to additional Taylor cone thinning, acceleration and air drag reduction. Hence, the average droplet diameter during the initial stage of spraying decreased by 60% and 120%, compared to conventional electrospray, with the application of 5 and 10 psi air flow, respectively. Our results also demonstrate that by increasing the air flow, one can precisely control the homogeneity and efficiency (60% increase) of coating deposition. Further, we observe a significant improvement in spatial distribution of spherical (CB) and anisotropic (CNT) active nanoinclusions in deposited coatings with the increase of the air flow. Improvement is due to a synergistic effect of the droplet size reduction, and strain-induced rupture of nanoparticle agglomerates that occurs when extensional forces, provided by the air flow, overcome cohesive forces between nanoparticles. Furthermore, to alleviate scalability constraints and mitigate the coating irregularity issues due to the surface-charge build up on the substrate during DC electrospray, we developed a novel alternating current air-controlled electrospraying process ($AC^2$ electrospray). A rigorous visualization study confirmed that we can further control the atomization and deposition process, even over insulating substrates, due to the droplet-charge neutralization. We can also enhance the production rate by at least an order of magnitude by significantly increasing the spinneret diameter (6 times). To the best of our knowledge, this is the first study in which the control of atomization and spatial distribution of various functional NPs in polymer films was obtained in a single step by tuning the driving force (air flow rate) of the deposition

method. Therefore, AC and $AC^2$ electrospray techniques undoubtedly deserve deeper attention in energy storage applications, providing a powerful and robust methodology to efficiently produce functional coatings with highly controlled surface morphology, topology and placement of unfunctionalized nanoparticles. In Chapter 5, we utilized a new air-controlled electrospraying technique for micro/nano-scale encapsulation, and to fabricate polymer composites with in situ indication of mechanical damage.

## REFERENCES

[1]     E. Burkarter, C. K. Saul, F. Thomazi, N. C. Cruz, L. S. Roman, and W. H. Schreiner, "Superhydrophobic electrosprayed PTFE," *Surf. Coatings Technol.*, vol. 202, no. 1, pp. 194–198, 2007.

[2]     J. Bravo, L. Zhai, Z. Wu, R. E. Cohen, and M. F. Rubner, "Transparent superhydrophobic films based on silica nanoparticles," *Langmuir*, vol. 23, no. 28, pp. 7293–7298, 2007.

[3]     S. T. Yohe and M. W. Grinstaff, "A facile approach to robust superhydrophobic 3D coatings via connective-particle formation using the electrospraying process.," *Chem. Commun.*, vol. 49, no. 8, pp. 804–6, 2013.

[4]     Q. Guo, J. P. Mather, P. Yang, M. Boden, and P. T. Mather, "Fabrication of Polymeric Coatings with Controlled Microtopographies Using an Electrospraying Technique.," *PLoS One*, vol. 10, no. 6, pp. 1–14, 2015.

[5]     L. T. De Jonge, S. C. G. Leeuwenburgh, J. J. J. P. Van Den Beucken, J. G. C. Wolke, and J. A. Jansen, "Electrosprayed enzyme coatings as bioinspired alternatives to bioceramic coatings for orthopedic and oral implants," *Adv. Funct. Mater.*, vol. 19, no. 5, pp. 755–762, 2009.

[6]     M. Valvo, E. García-Tamayo, U. Lafont, and E. M. Kelder, "Direct synthesis and coating of advanced nanocomposite negative electrodes for Li-ion batteries via electrospraying," *J. Power Sources*, vol. 196, no. 23, pp. 10191–10200, 2011.

[7]     Y. Yu, C.-H. Chen, J.-L. Shui, and S. Xie, "Nickel-Foam-Supported Reticular CoO-Li2O Composite Anode Materials for Lithium Ion Batteries," *Angew. Chemie Int. Ed.*, vol. 44, no. 43, pp. 7085–7089, 2005.

[8]     C. H. Chen, E. M. Kelder, M. J. G. Jak, and J. Schoonman, "Electrostatic spray deposition

of thin layers of cathode materials for lithium battery," *Solid State Ionics*, vol. 86–88, no. 96, pp. 1301–1306, 1996.

[9]     Y. Yu, J. L. Shui, Y. Jin, and C. H. Chen, "Electrochemical performance of nano-SiO2 modified LiCoO 2 thin films fabricated by electrostatic spray deposition (ESD)," *Electrochim. Acta*, vol. 51, no. 16, pp. 3292–3296, 2006.

[10]    A. A. van Zomeren, E. M. Kelder, J. C. M. Marijnissen, and J. Schoonman, "The Production of Thin Films of LiMn2O4 by Electrospraying," *J. Aerosol Sci.*, vol. 25, no. 6, pp. 407–410, 1994.

[11]    L. Wang, H. W. Xu, P. C. Chen, D. W. Zhang, C. X. Ding, and C. H. Chen, "Electrostatic spray deposition of porous Fe2O3 thin films as anode material with improved electrochemical performance for lithium-ion batteries," *J. Power Sources*, vol. 193, no. 2, pp. 846–850, 2009.

[12]    Y. Yu, L. Gu, A. Dhanabalan, C. H. Chen, and C. Wang, "Three-dimensional porous amorphous SnO2 thin films as anodes for Li-ion batteries," *Electrochim. Acta*, vol. 54, no. 28, pp. 7227–7230, 2009.

[13]    J. Schoonman and E. M. Kelder, "Thin film solid electrolytes and electrodes for rechargeable lithium-ion batteries," *J. Power Sources*, vol. 68, no. 1, pp. 65–68, 1997.

[14]    K. L. Choy, "Chemical vapour deposition of coatings," *Prog. Mater. Sci.*, vol. 48, no. 2, pp. 57–170, 2003.

[15]    N. Selvakumar and H. C. Barshilia, "Review of physical vapor deposited (PVD) spectrally selective coatings for mid- and high-temperature solar thermal applications," *Sol. Energy Mater. Sol. Cells*, vol. 98, pp. 1–23, 2012.

[16]    U. Helmersson, M. Lattemann, J. Bohlmark, A. P. Ehiasarian, and J. T. Gudmundsson,

"Ionized physical vapor deposition (IPVD): A review of technology and applications," *Thin Solid Films*, vol. 513, no. 1–2, pp. 1–24, 2006.

[17]   P. Fauchais, "Understanding plasma spraying," *J. Phys. D. Appl. Phys.*, vol. 37, no. 9, pp. R86–R108, 2004.

[18]   C. J. Brinker, G. C. Frye, A. J. Hurd, C. S. Ashley, S. N. Laboratories, and I. Introduction, "Fundamentals of sol-fel dip coating," *Thin Solid Films*, vol. 201, pp. 97–108, 1991.

[19]   L. E. Scriven, "Physics and Applications of Dip Coating and Spin Coating," *Mater. Res. Soc.*, vol. 121, pp. 717–729, 1998.

[20]   N. Sahu, B. Parija, and S. Panigrahi, "Fundamental understanding and modeling of spin coating process: A review," *Indian J. Phys.*, vol. 83, no. 4, pp. 493–502, 2009.

[21]   A. Jaworek, "Electrospray droplet sources for thin film deposition," *J. Mater. Sci.*, vol. 42, no. August 2004, pp. 266–297, 2007.

[22]   A. M. Gañán-Calvo, "The surface charge in electrospraying: Its nature and its universal scaling laws," *J. Aerosol Sci.*, vol. 30, no. 7, pp. 863–872, 1999.

[23]   A. Jaworek and A. T. Sobczyk, "Electrospraying route to nanotechnology: An overview," *J. Electrostat.*, vol. 66, pp. 197–219, 2008.

[24]   H. You, Y. Yang, X. Li, K. Zhang, X. Wang, M. Zhu, and B. S. Hsiao, "Low pressure high flux thin film nanofibrous composite membranes prepared by electrospraying technique combined with solution treatment," *J. Memb. Sci.*, vol. 394–395, pp. 241–247, 2012.

[25]   I. Uematsu, H. Matsumoto, K. Morota, M. Minagawa, A. Tanioka, Y. Yamagata, and K. Inoue, "Surface morphology and biological activity of protein thin films produced by electrospray deposition," *J. Colloid Interface Sci.*, vol. 269, no. 2, pp. 336–340, 2004.

[26] A. Jaworek, A. Krupa, M. Lackowski, A. T. Sobczyk, T. Czech, S. Ramakrishna, S. Sundarrajan, and D. Pliszka, "Nanocomposite fabric formation by electrospinning and electrospraying technologies," *J. Electrostat.*, vol. 67, no. 2–3, pp. 435–438, 2009.

[27] S. Sarkar, N. Levit, and G. Tepper, "Deposition of polymer coatings onto SAW resonators using AC electrospray," *Sensors Actuators, B Chem.*, vol. 114, no. 2, pp. 756–761, 2006.

[28] S. Maheshwari, N. Chetwani, and C. Hsueh-Chia, "Alternating current electrospraying," *Industrial and Engineering Chemistry Research*. pp. 9358–9368, 2009.

[29] D. Duft, T. Achtzehn, R. Müller, B. a Huber, and T. Leisner, "Coulomb fission: Rayleigh jets from levitated microdroplets.," *Nature*, vol. 421, no. 6919, p. 128, 2003.

[30] Y. Yao, M. T. McDowell, I. Ryu, H. Wu, N. Liu, L. Hu, W. D. Nix, and Y. Cui, "Interconnected silicon hollow nanospheres for lithium-ion battery anodes with long cycle life," *Nano Lett.*, vol. 11, pp. 2949–2954, 2011.

[31] W. Wang and P. N. Kumta, "Nanostructured Hybrid Silicon/Carbon Nanotube Heterostructures: Reversible High-Capacity Lithium-Ion Anodes," *ACS Nano*, vol. 4, no. 4, pp. 2233–2241, 2010.

[32] H. Xiang, K. Zhang, G. Ji, J. Y. Lee, C. Zou, X. Chen, and J. Wu, "Graphene/nanosized silicon composites for lithium battery anodes with improved cycling stability," *Carbon N. Y.*, vol. 49, pp. 1787–1796, 2011.

[33] B. Wang, X. Li, X. Zhang, B. Luo, M. Jin, M. Liang, S. A. Dayeh, S. T. Picraux, and L. Zhi, "Adaptable silicon-carbon nanocables sandwiched between reduced graphene oxide sheets as lithium ion battery anodes," *ACS Nano*, vol. 7, no. 2, pp. 1437–1445, 2013.

[34] Z. Li, H. Zhang, Q. Liu, Y. Liu, L. Stanciu, and J. Xie, "Novel Pyrolyzed Polyaniline-Grafted Silicon Nanoparticles Encapsulated in Graphene Sheets As Li-Ion Battery

Anodes," *ACS Appl. Mater. Interfaces*, vol. 6, pp. 5996–6002, 2014.

[35] Y. S. Kim, G. Shoorideh, Y. Zhmayev, J. Lee, Z. Li, B. Patel, S. Chakrapani, J. H. Park, S. Lee, and Y. L. Joo, "The critical contribution of unzipped graphene nanoribbons to scalable silicon-carbon fiber anodes in rechargeable Li-ion batteries," *Nano Energy*, vol. 16, pp. 446–457, 2015.

[36] R. Teki, R. Krishnan, T. C. Parker, T. M. Lu, P. N. Kumta, and N. Koratkar, "Nanostructured silicon anodes for lithium Ion rechargeable batteries," *Small*, vol. 5, pp. 2236–2242, 2009.

[37] Y. S. Hu, R. Demir-Cakan, M. M. Titirici, J. O. Müller, R. Schlögl, M. Antonietti, and J. Maier, "Superior storage performance of a Si@SiOx/C nanocomposite as anode material for lithium-ion batteries," *Angew. Chemie - Int. Ed.*, vol. 47, pp. 1645–1649, 2008.

[38] B. J. Landi, M. J. Ganter, C. D. Cress, R. A. DiLeo, and R. P. Raffaelle, "Carbon nanotubes for lithium ion batteries," *Energy Environ. Sci.*, vol. 2, no. 6, pp. 638–654, 2009.

[39] Y. Zhmayev, S. Pinge, G. Shoorideh, G. L. Shebert, P. Kaur, H. Liu, and Y. L. Joo, "Controlling the Placement of Spherical Nanoparticles in Electrically Driven Polymer Jets and its Application to Li-Ion Battery Anodes," *Small*, vol. 12, no. 40, pp. 5543–5553, 2016.

[40] L. Y. Beaulieu, S. D. Beattie, T. D. Hatchard, and J. R. Dahn, "The Electrochemical Reaction of Lithium with Tin Studied By In Situ AFM," *J. Electrochem. Soc.*, vol. 150, no. 4, p. 1457, 2003.

[41] S. T. Chang, I. C. Leu, C. L. Liao, J. H. Yen, and M. H. Hon, "Electrochemical behavior of nanocrystalline tin oxide electrodeposited on a Cu substrate for Li-ion batteries," *J.*

*Mater. Chem.*, vol. 14, no. 12, pp. 1821–1826, 2004.

[42]   E. Zhmayev, D. Cho, and Y. L. Joo, "Nanofibers from gas-assisted polymer melt
electrospinning," *Polymer*, vol. 51, no. 18, pp. 4140–4144, Aug. 2010.

[43]   J. H. Park and Y. L. Joo, "Tailoring nanorod alignment in a polymer matrix by
elongational flow under confinement: simulation, experiments, and surface enhanced
Raman scattering application.," *Soft Matter*, vol. 10, pp. 3494–3505, 2014.

[44]   J. H. Park, V. Kalra, and Y. L. Joo, "Controlling the dispersion and orientation of
nanorods in polymer melt under shear: Coarse-grained molecular dynamics simulation
study," *J. Chem. Phys.*, vol. 140, pp. 124903–124920, 2014.

[45]   V. Kalra, F. Escobedo, and Y. L. Joo, "Effect of shear on nanoparticle dispersion in
polymer melts: A coarse-grained molecular dynamics study," *J. Chem. Phys.*, vol. 132, no.
2, p. 24901, 2010.

[46]   V. Kalra and Y. L. Joo, "Coarse-grained molecular dynamics study of block
copolymer/nanoparticle composites under elongational flow," *J. Chem. Phys.*, vol. 131,
no. 21, p. 214904, 2009.

[47]   V. Kalra, S. Mendez, F. Escobedo, and Y. L. Joo, "Coarse-grained molecular dynamics
simulation on the placement of nanoparticles within symmetric diblock copolymers under
shear flow," *J. Chem. Phys.*, vol. 128, no. 16, p. 164909, 2008.

[48]   B. Faure, G. Salazar-Alvarez, A. Ahniyaz, I. Villaluenga, G. Berriozabal, Y. R. De
Miguel, and L. Bergström, "Dispersion and surface functionalization of oxide
nanoparticles for transparent photocatalytic and UV-protecting coatings and sunscreens,"
*Sci. Technol. Adv. Mater.*, vol. 14, p. 23001, 2013.

[49]   A. H. Lu, E. L. Salabas, and F. Schüth, "Magnetic nanoparticles: Synthesis, protection,

functionalization, and application," *Angew. Chemie - Int. Ed.*, vol. 46, no. 8, pp. 1222–1244, 2007.

[50]   M. R. Bockstaller, R. A. Mickiewicz, and E. L. Thomas, "Block copolymer nanocomposites: Perspectives for tailored functional materials," *Adv. Mater.*, vol. 17, no. June 2015, pp. 1331–1349, 2005.

[51]   G. A. Buxton and A. C. Balazs, "Simulating the morphology and mechanical properties of filled diblock copolymers," *Phys. Rev. E. Stat. Nonlin. Soft Matter Phys.*, vol. 67, no. March, pp. 031802–031814, 2003.

[52]   A. K. Khandpur, S. Forster, F. S. Bates, I. W. Hamley, A. J. Ryan, W. Bras, K. Almdal, and K. Mortensen, "Polyisoprene-Polysterene Diblock Copolymer Phase Diagram near the Order-Disorder Transition," *Macromolecules*, vol. 28, pp. 8796–8806, 1995.

[53]   Y. Zhmayev, M. J. Divvela, A. C. Ruo, T. Huang, and Y. L. Joo, "The jetting behavior of viscoelastic Boger fluids during centrifugal spinning," *Phys. Fluids*, vol. 27, no. 12, p. 123101, 2015.

[54]   D. H. Reneker, A. L. Yarin, H. Fong, and S. Koombhongse, "Bending instability of electrically charged liquid jets of polymer solutions in electrospinning," *J. Appl. Phys.*, vol. 87, no. 9, p. 4531, 2000.

[55]   A. L. Yarin, S. Koombhongse, and D. H. Reneker, "Bending instability in electrospinning of nanofibers," *J. Appl. Phys.*, vol. 89, no. 5, p. 3018, 2001.

[56]   Z. X. Shu, R. S. McMillan, and J. J. Murray, "Electrochemical Intercalation of Lithium into Graphite," *J. Electrochem. Soc.*, vol. 140, no. 4, pp. 922–927, Apr. 1993.

[57]   A. Greiner and J. H. Wendorff, "Electrospinning: A fascinating method for the preparation of ultrathin fibers," *Angew. Chemie - Int. Ed.*, vol. 46, no. 30, pp. 5670–5703, 2007.

[58]   S. H. Liao, C. C. Weng, C. Y. Yen, M. C. Hsiao, C. C. M. Ma, M. C. Tsai, A. Su, M. Y. Yen, Y. F. Lin, and P. L. Liu, "Preparation and properties of functionalized multiwalled carbon nanotubes/polypropylene nanocomposite bipolar plates for polymer electrolyte membrane fuel cells," *J. Power Sources*, vol. 195, no. 1, pp. 263–270, 2010.

[59]   D. V. Kosynkin, W. Lu, A. Sinitskii, G. Pera, Z. Sun, and J. M. Tour, "Highly conductive graphene nanoribbons by longitudinal splitting of carbon nanotubes using potassium vapor," *ACS Nano*, vol. 5, no. 2, pp. 968–974, 2011.

[60]   R. Kessick, J. Fenn, and G. Tepper, "The use of AC potentials in electrospraying and electrospinning processes," *Polymer*, vol. 45, no. 9, pp. 2981–2984, 2004.

[61]   P. Pokorny, E. Kostakova, F. Sanetrnik, P. Mikes, J. Chvojka, T. Kalous, M. Bilek, K. Pejchar, J. Valtera, and D. Lukas, "Effective AC needleless and collectorless electrospinning for yarn production," *Phys. Chem. Chem. Phys.*, vol. 16, no. 48, pp. 26816–26822, 2014.

# CHAPTER 5

# NANO-SCALE ENCAPSULATION OF DYES VIA AC ELECTROSPRAY FOR MECHANICAL DAMAGE INDICATION

## 5.1. Introduction

Polymer composites are prone to inconspicuous mechanical damage, which can substantially compromise robustness and overall performance. For example, the deterioration of automotive protective coatings, due to harsh environmental conditions and scratching, causes corrosion or the loss of esthetic appearance. [1, 2] On the other hand, nylon ropes and harnesses are generally subjected to significant extensional deformations, and even a microscopic damage leads to the loss of mechanical properties, which can be fatal in some applications. [3] Thus, the capability to promptly identify these defects is important for both safety and economic reasons.

There is a plethora of techniques to trigger mechanochromic response to deformation or damage. Mechanochemistry, for instance, has been utilized to produce a visual indication of deformation or damage in bulk polymers under extension. [4–7] However, this technique suffers from low intensity, fading [8–10] and reversible mechanochromic response [11, 12], which is not favorable for the actual application. Therefore, some of the recent studies reveal a promising alternative methodology in which the indication agent is insulated in the polymer shell of a capsule [13–15], or other hollow geometry [16, 17]. Encapsulation technology has recently gained a lot of attention in pharmaceutical, food, and textile industries. [13, 18–20] The aim of this technique is to shield the functional core material (dyes, enzymes, drugs, fragrances, flavors, etc.) from the surroundings, by encapsulating it in the polymer shell. The polymer material may be chosen based on the application requirements and environmental conditions, and there is a myriad of natural,

semi-synthetic as well as synthetic candidates. [18, 21] Micron and nano-scale capsules can be utilized solely or incorporated in nanocomposites and coatings to provide functionality. Once the capsule shell breaks due to mechanical damage, the indication becomes active by the exposure of the colored agent. Therefore, encapsulation has been extensively utilized to generate mechanochromic or photochromic response to mechanical or environmental degradation. [4, 13, 15]

Although, this technique was previously limited due to poor stability, low contrast and insufficient control, there are several robust concepts that were recently presented. Li et al. [4], for example, reported a microcapsule-based technique that yields a distinguishable in situ indication of mechanical damage in polymer composites. The capsules containing 2',7'-dichlorofluorescein (DCF), as an indicating agent, are homogeneously distributed in the amine-containing epoxy coating. When microcapsules are ruptured due to mechanical damage, the core materials react with the amine groups and change color from yellow to red, which provides a clear indication. It should be mentioned that this methodology provides a stable and degradation-resistant mechanism, and does not require supplementary components or activators. However, this technique requires a tedious multi-step synthesis procedure, and offers little control of dimensions and size distribution of fabricated microcapsules. Hence, to further commercialize the process, there is an urgent demand to overcome the scalability constraints.

Recently, electrospraying gained a lot of attention in the fabrication of particles, coatings and micron/nano-scale encapsulation, due to its ease and potential scalability. [19, 21–29] The process utilizes a high electric potential to a liquid that is continuously pumped through a capillary nozzle. Approaching sufficient charge accumulation on the fluid surface, the droplet takes a conic shape (Taylor cone), which later breaks into fine charged droplets that further rapidly subdivide

118

due to Coulomb fission. [30] The droplets are monodisperse, and the size can be precisely controlled by tuning electrospraying parameters (voltage, distance between the spinneret and collector, feeding rate, etc.). The final droplets are deposited directly on the substrate or in the gelation bath, in a form of solidified particles, capsules or film, which can be controlled by tuning process conditions, fluid composition, and solvent evaporation rate. [22, 31] Many authors have optimized the elecrospraying process, and investigated the effect of experimental conditions on the capsule fabrication for various applications. [21, 29] For example, Ghayempour et al. [21] utilized a coaxial nozzle in electrospraying setup to encapsulate essential oil with sodium alginate biopolymer, and optimized conditions for microcapsule (~200 $\mu$m) production. It has been observed that increasing the magnitude of the ring electrode voltage, spinneret diameter, feeding rate, distance and polymer molecular weight leads to the increase of the capsule size. However, the increase of the driving force results in the decrease of capsule dimensions.

Conventional electrospraying has been shown to be superior to alternative techniques [4, 14, 32], and offers a robust single-step encapsulation procedure. However, significant challenges remain, especially in the pursuit to increase productivity, further control the size, and produce nano-scale capsules. In this study, we propose a novel air-controlled (AC) electrospraying process, which was developed to overcome all the foregoing challenges. The AC electrospray utilizes a circumferentially uniform air flow as a sheath layer of coaxial spinneret [33], providing additional extensional deformation at the initial stage of droplet emanation to tune the atomization mechanism. This powerful method allows further control of fluid atomization, homogeneity of deposition and a ten-fold increase in productivity per-nozzle, compared to its conventional counterpart.

In the current study, the AC electrospraying technique was successfully utilized for mass production of encapsulated oil red dye in polyvinylidene fluoride (PVDF) and polystyrene (PS) shells. We investigated the effect of the sheath layer air flow rate, as well as other experimental conditions, to control the size and optimize the production of sub-micron capsules. A rigorous analysis, utilizing scanning electron microscopy (SEM), was performed to quantify the effects contributed by the process conditions, and to study morphological changes. Finally, the process was used to fabricate stress-sensing patches via a single-step direct deposition of encapsulated dye over the nonwoven polypropylene substrate. These composites were further tested using compression mode of Instron machine, and the mechanochromic response was analyzed as a function of different capsule loadings and sizes.

To the best of author's knowledge, AC electrospray is the first process that utilizes the synergistic effect of aerodynamic and electrohydrodynamic forces for efficient and single-step mass production of nanocapsules, precisely controlling their morphologies. From the commercialization perspective, it is important to emphasize that we present a robust and readily-scalable technique, that can be utilized in the critical-stress and other damage-indication application for various materials.

## 5.2. Experimental section

*Materials*: PVDF capsules were fabricated using polyvinylidene fluoride (Mw=180,000 g mol$^{-1}$) as a shell material, N,N-dimethylformamide (DMF) as a solvent, hexadecane ($\geq$ 99%), and Oil Red O dye as a core. PS capsules were fabricated using polystyrene (Mw=280,000) as a shell material, dichloromethane (DCM) ($\geq$ 99.8%) as a solvent, hexadecane ($\geq$ 99%), and Oil Red O

dye as a core. All materials were purchased from Sigma Aldrich (USA). Nonwoven polypropylene substrate was purchased from Hollingsworth & Vose (PE13030CA).

*Solution preparation and capsule fabrication*: 8% (w/w) PVDF/DMF and 4% PS/DCM (w/w) solutions were first prepared, then 0.55 g of hexadecane and 0.003 g of Oil Red O dye were added and stirred overnight. Capsules were prepared via conventional electrospray and AC electrospray (Figure 5.1) utilizing different air pressures, infuse rates, nozzle diameters, electric potentials at the spinneret and the ring electrode. Capsules were collected on the aluminum foil, glass slides and nonwoven substrate for further characterization.

*Characterization*: Capsule morphology and dimensions were characterized using scanning electron microscopy (SEM) using a high-performance scanning electron microscope (Tescan Mira3 FESEM). Confocal laser scanning microscopy (CLSM) images were obtained by using confocal laser scanning microscope (Zeiss LSM 710). Compression testing was performed using Instron 5566 Universal Testing Machine. Resulting digital images were analyzed using MATLAB 2014R and ImageJ.
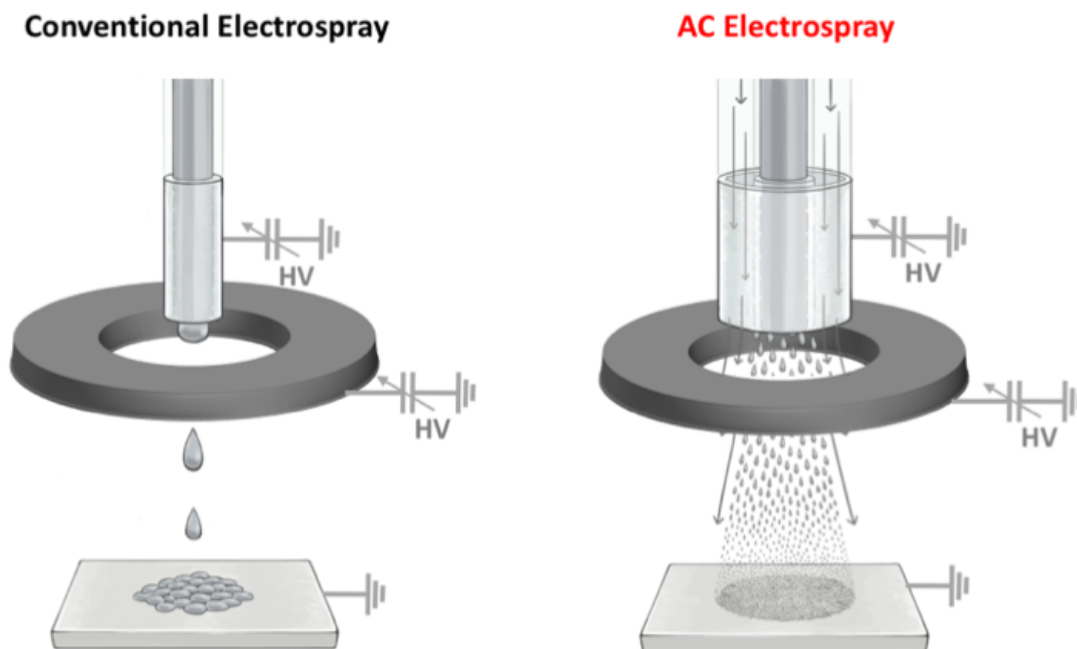
Figure 5.1. Conventional electrospray and Air-Controlled electrospray setups.

## 5.3. Results and discussions

### 5.3.1. *Mass production of micro/nanocapsules via AC Electrospray*

By utilizing a high electric potential between the nozzle and the grounded collector plate in electrospraying, we emulate a dripping process that is commonly used in the production of capsules, yet reducing the droplet dimensions and increasing productivity. [21, 29] By employing circumferentially uniform air flow as a sheath layer of concentric coaxial nozzle in AC electrospray we can further control atomization and significantly increase the throughput. We discovered that the size and morphology of resulting capsules can be precisely controlled by tuning experimental parameters, and have a more pronounced effect in conjunction with the air flow.

*5.3.1.1. Effect of the air flow rate*

Additional shearing and extensional deformation provided by the sheath-layer air flow leads to decrease of the air drag, sufficient thinning and acceleration of the polymeric fluid at the initial stage of spraying. [33] These effects modify the atomization mechanism, resulting in the jet emanation and further evolution of bending instability, which is generally referred to as a "whipping motion'. [34, 35] While the polymer jet is undergoing bending, which is triggered by a repulsive response to the applied electric potential, its dimensions further decrease until it breaks into small droplets, which further undergo Coulomb fission. [30] It should be mentioned that bending instability, is rarely observed in conventional electrospraying process, due to low viscoelasticity, and becomes more intense with the increase of the air flow rate.

In order to investigate the influence of this parameter on the final dimensions and morphology of PVDF-based capsules, we varied the air flow pressure from 0 psi (Conventional electrospray) to 16 psi. Figure 5.2 shows SEM images of PVDF nanocapsules fabricated under different air flows, and Figure 5.2 E displays the size distribution diagram. The results suggest that with increasing the air flow rate, the capsule average diameter significantly decreases, from around 1.7 $\mu$m to 550 nm. It should be noted that the size distribution becomes more homogeneous with the increase of the air flow, however the morphology of the AC-electrosprayed capsule is not as smooth as for its conventionally produced counterpart.
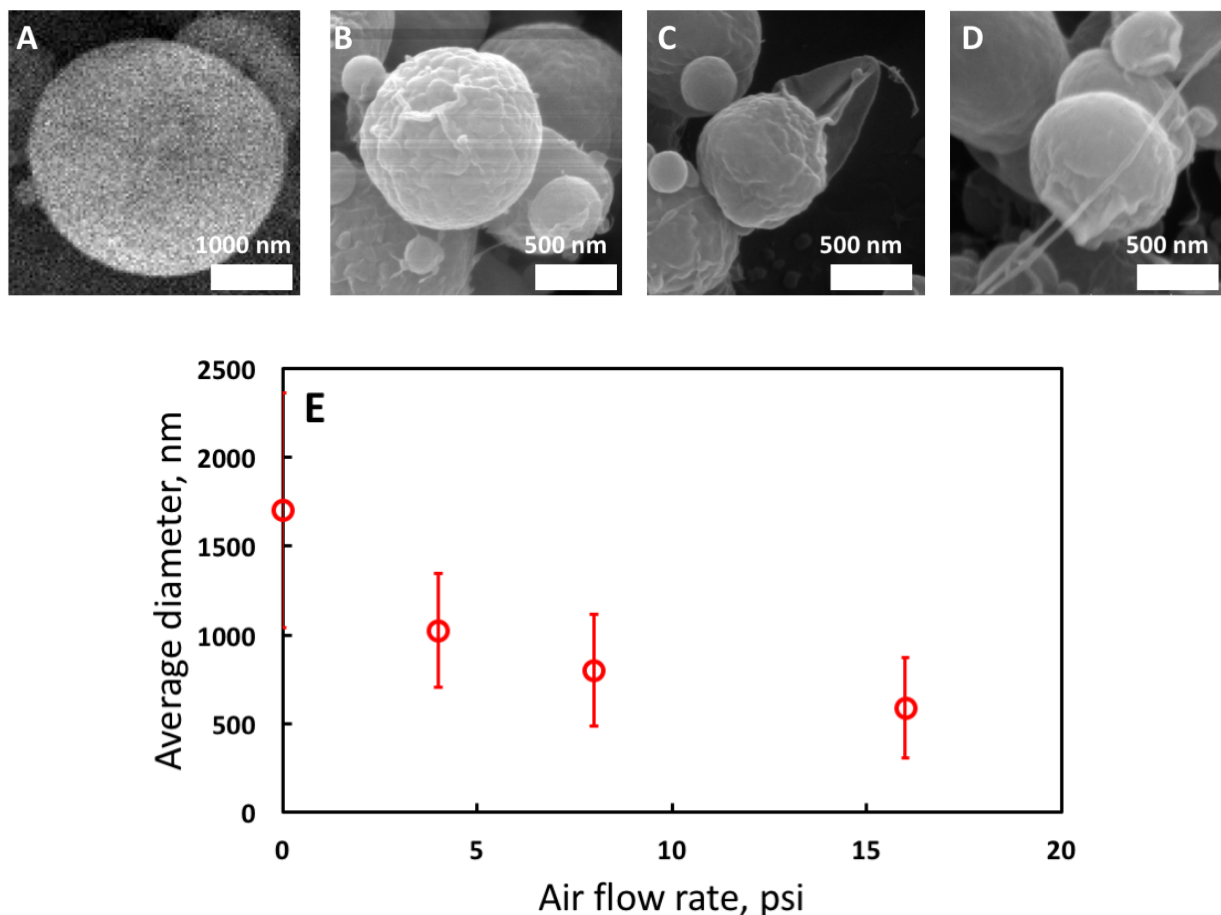
Figure 5.2. SEM images of PVDF/Oil Red O nanocapsules fabricated via electrospraying at different air flow rates: A) 0 psi (Conventional electrospray), B) 4 psi, C) 8 psi, and D) 16 psi, and 12.5 kV, 16 cm distance from the spinneret to collector, and 0.009 mL/min feeding rate. E) PVDF/Oil Red O nanocapsule sizes controlled by tuning air flow rate.

### 5.3.1.2. Electric potential at the nozzle and ring electrode

By tuning electric potential, which is the major driving force of the AC electrospraying process, we control the charge accumulation on the fluid surface and the vigor of bending instability. The accumulated charge overcomes the surface tension of the polymer solution to form jets that are accelerated away from the spinneret. Due to sufficient thinning and additional

acceleration from the air flow, vigorously bending jets effectively break into small droplets which are further subdivided by electrostatic forces. [21, 30, 33]

The influence of electric potential was investigated by varying the applied nozzle voltage from 12 to 25 kV during this array of experiments. Figure 5.3 A demonstrates that increasing nozzle voltage in AC electrospray results in reduction of capsule sizes. Further, in order to control the whipping motion and dripping frequency, we utilized a ring electrode at different electric potentials, which was placed at various distances from the spinneret. It can be seen from Figure 5.3 B,C that increasing the ring voltage and the distance hinders the intensity of bending instability, increasing the size of the resulting capsules. It should be mentioned that similar phenomenon was reported in previous studies [21, 36, 37], and can benefit the mass production of highly-uniform nanocapsules.
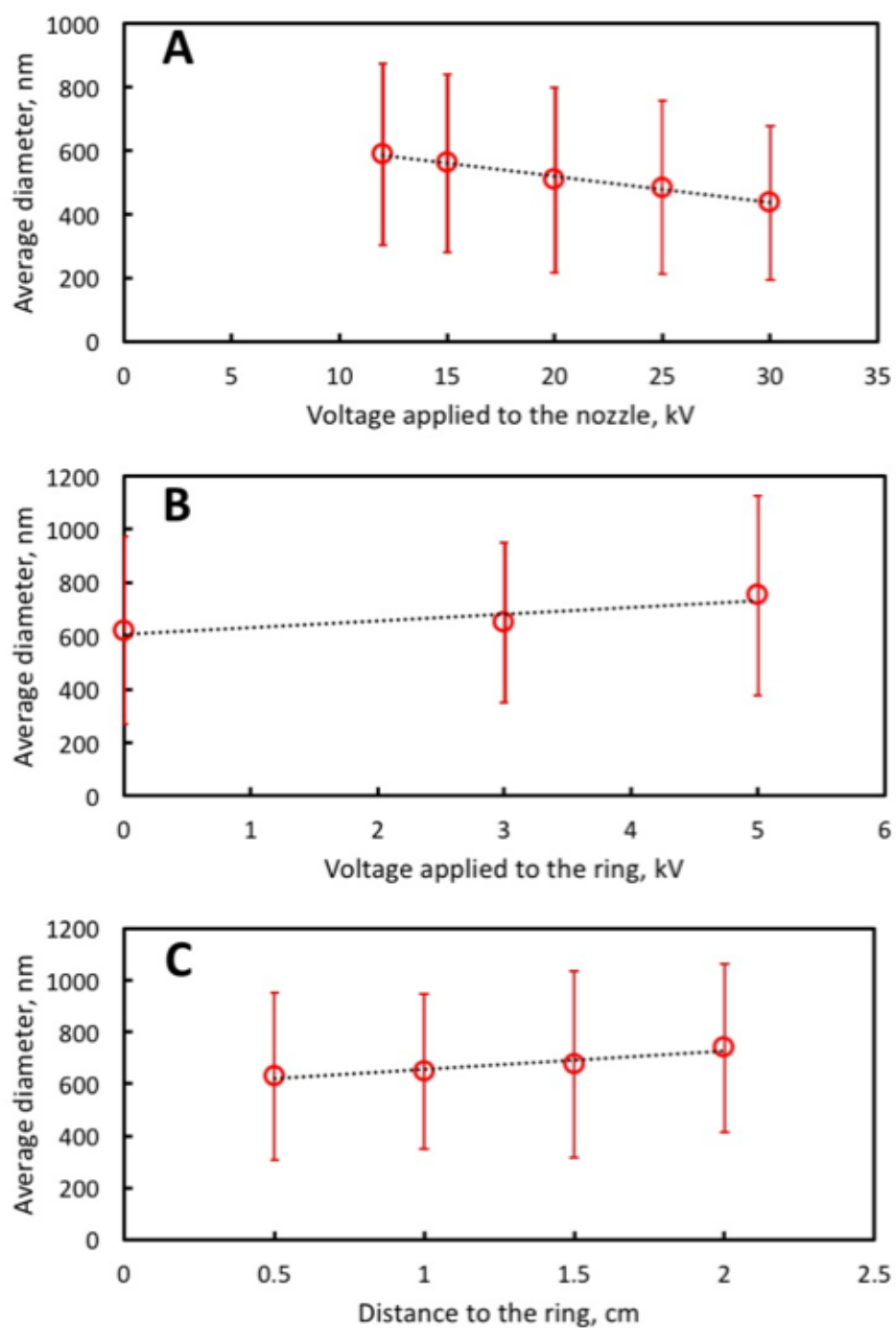
Figure 5.3. PVDF/Oil Red O nanocapsule sizes controlled by tuning electric potential. A) voltage applied at the nozzle, B) voltage at the ring electrode and C) distance from the nozzle to the ring electrode. Capsules were fabricated via AC electrospray at 8 psi air flow, 0.009 mL/min feeding rate, 16 cm distance from the spinneret to collector.

### 5.3.1.3. Effect of the solution flow rate

The effect of the flow rate was examined by changing the pumping rate of PVDF solution during AC electrospray, while other parameters were kept constant. Providing higher volume of solution requires substantial driving forces to maintain efficient atomization. Therefore, to sustain the process equilibria, electric potential and air flow must be simultaneously increased to control the droplet size. Otherwise, the resulting capsule diameter significantly increases (Figure 5.4). It should be noted that the flow rate affected the size distribution of PVDF capsules (Figure 5.4 D). Higher feeding rates produced polydisperse encapsulates, potentially due to increased dripping frequency and deficient electric force gradient. Therefore, to maintain an efficient process and high throughput, it is necessary to choose a suitable driving force for a range of preferred flow rates. Moreover, utilizing AC electrospraying process, we can increase the feeding rate by almost 10 times and still fabricate capsules that are smaller than the ones produced via conventional electrospraying.
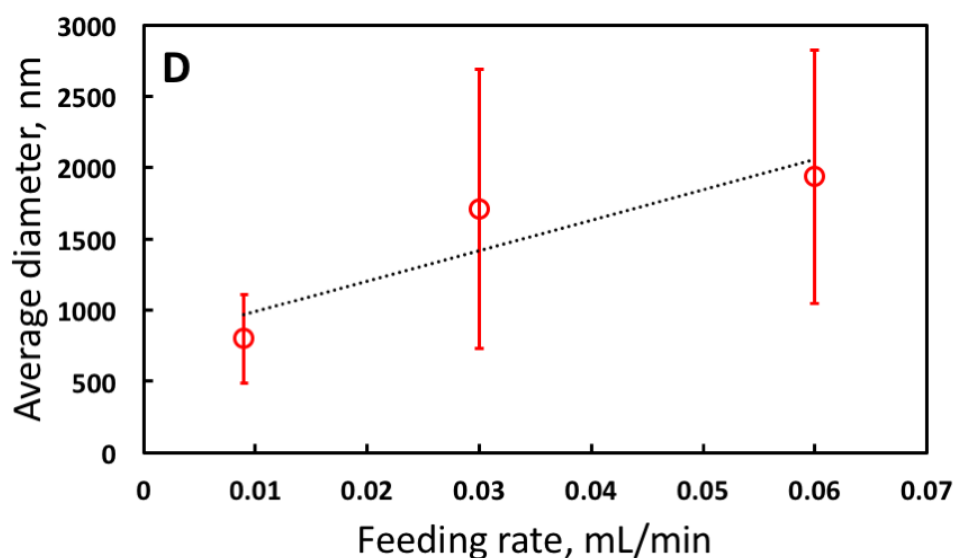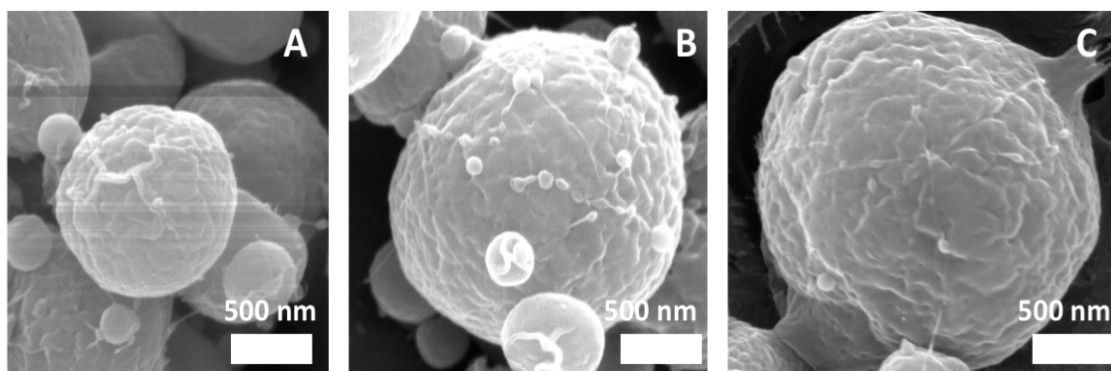
Figure 5.4. SEM images of PVDF/Oil Red O nanocapsules fabricated via AC electrospray at different feeding rates: A) 0.009 mL/min, B) 0.03 mL/min, and C) 0.06 mL/min, at 8 psi, 12.5 kV, 16 cm distance from the spinneret to the collector. D) PVDF/Oil Red O nanocapsule sizes controlled by tuning feeding rate.

### 5.3.2. Critical mechanical damage indication via mechanochromic response

High contrast between "on" and "off" modes of mechanochromic stress indicator is required for effective critical damage detection. In the current study, we developed micro/nano encapsulation-based composites, that provide a distinct optical indication of compressive deformation. This approach will be utilized to indicate and forestall the critical failure in nylon

ropes that are subjected to extreme tensile deformations in various applications, such as climbing or construction. The critical-stress indicating patch is molded to the thimble of the rope, where a carabiner is connected. When the rope is subjected to high extensional deformation, the shackle is compressed against the stress-indicating patch on the thimble, translating the tensile stress to compressive. The dye-containing capsules rupture when subjected to high loads, exposing the coloring agent, therefore providing mechanochromic indication to the user. The "turn-on" mechanism of the novel stress-sensing patch can be well controlled by tuning the capsule volume and dimensions, as well as the substrate material. It should be noted that the compression-triggered mechanocromic response is easily correlated to the critical tensile deformation, and does not possess any material limitations.

To demonstrate the potentiality of this novel approach, the critical-stress indicating patches were fabricated by direct AC electrospraying of the dye-containing (Figure 5.5 C) capsules in between the polypropylene nonwoven mats. Resulting composites were compressed at different loads (100-1000 kgf) utilizing Instron testing machine, and the mechanochromic response intensity was quantified using image analysis. The capsules rupture upon compression (Figure 5.5 D,E), releasing the coloring agent, that penetrates through macro-pores of the nonwoven mat, creating visual indication.
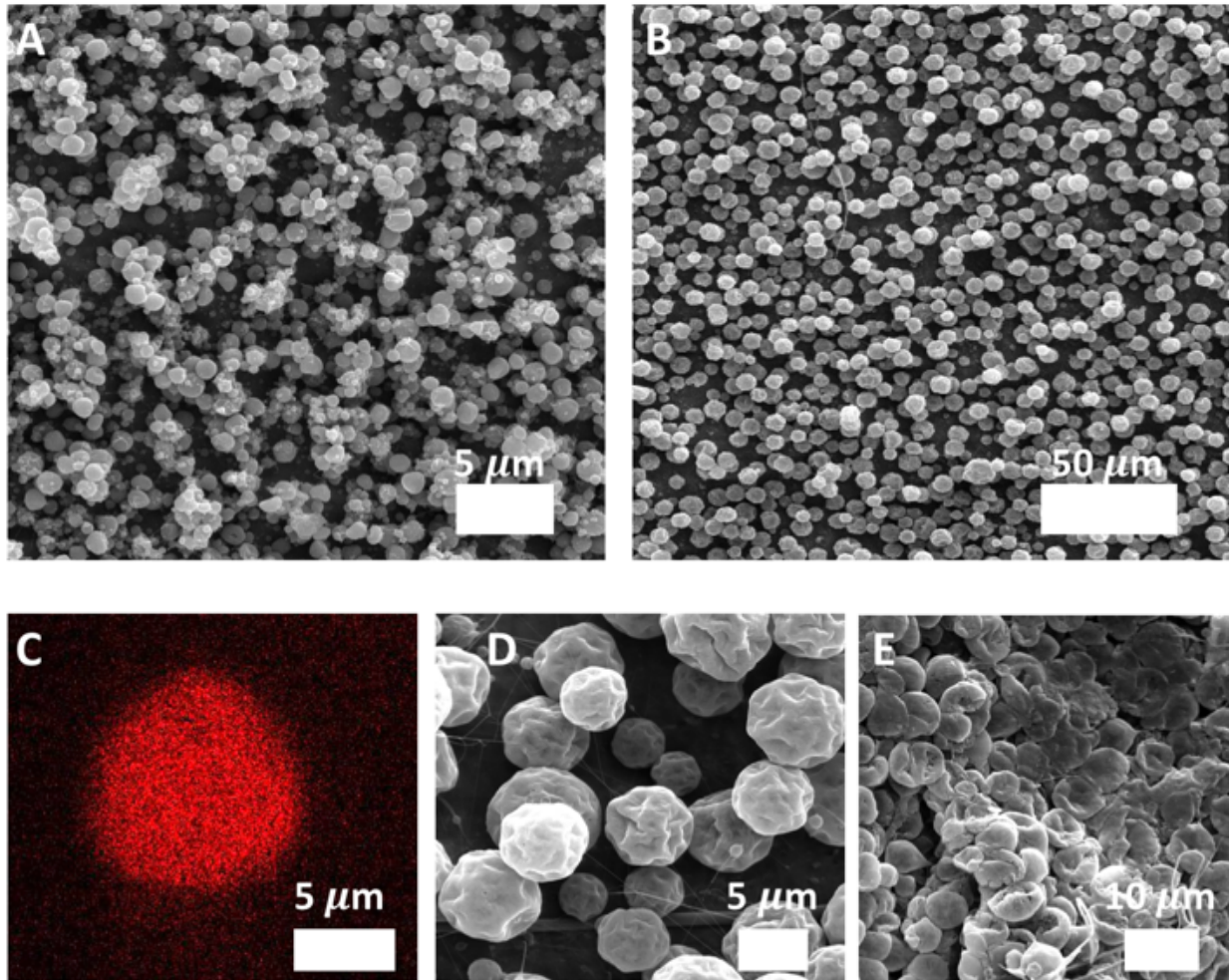
Figure 5.5. SEM and confocal microscopy analysis of PVDF and PS capsules. A) SEM image of PVDF/Oil Red O nanocapsules, B) SEM image of PS/Oil Red O microcapsules, C) Fluorescent confocal microscope image of PS/Oil Red O microcapsule, D) PS/Oil Red O microcapsule before compression and E) PS/Oil Red O microcapsule after compression.

The effect of the capsule size was probed by utilizing two different shell materials that produce nano-scale (PVDF – Figure 5.5 A) and micron-scale (PS – Figure 5.5 B) encapsulates. As shown in Figure 5.6, nano-scale PVDF capsules generate a heterogeneous visual response when subjected to Instron compressive deformation. This effect can be well explained by comparing the

dimensions of polypropylene fibers and dye-carrying encapsulates. Nano-scale PVDF capsules are mainly deposited within the macro-pores between polypropylene fibers. When the resulting composite is subjected to compression, polypropylene mat acts as a cushion, absorbing energy and hindering stress propagation to nanocapsules. Therefore, only parts of the composite, where macro-pores are entirely filled with PVDF capsules, resemble mechanochromic response upon compression (Figure 5.6 A-C).   On the other hand, PS capsules are commensurate in dimensions with polypropylene fibers, thus can easily occupy all the macro-pores and generate a homogeneous response to compressive deformation (Figure 5.7 A-C).

To evaluate the performance of stress-indicating patches and maximize color intensity, we investigated the effect of the applied compressive force and encapsulate concentration. It can be seen from Figure 5.6 A-C and Figure 5.7 A-C, that for both PVDF and PS-based patches the mechanochromic indication becomes more pronounced at higher deformations. Higher compressive loads effectively direct stress to encapsulates, facilitating complete rupture and distinct optical response. This behavior is further quantified by measuring average color intensities as a function of compressive force, and it can be seen from Figure 5.6 D-F and Figure 5.7 D-F that there is on average a 150% improvement at higher loads. As expected, the visual indication is more evident at higher capsule concentrations, which allows to precisely control the "turn-on" mechanism that is correlated to the actual application.
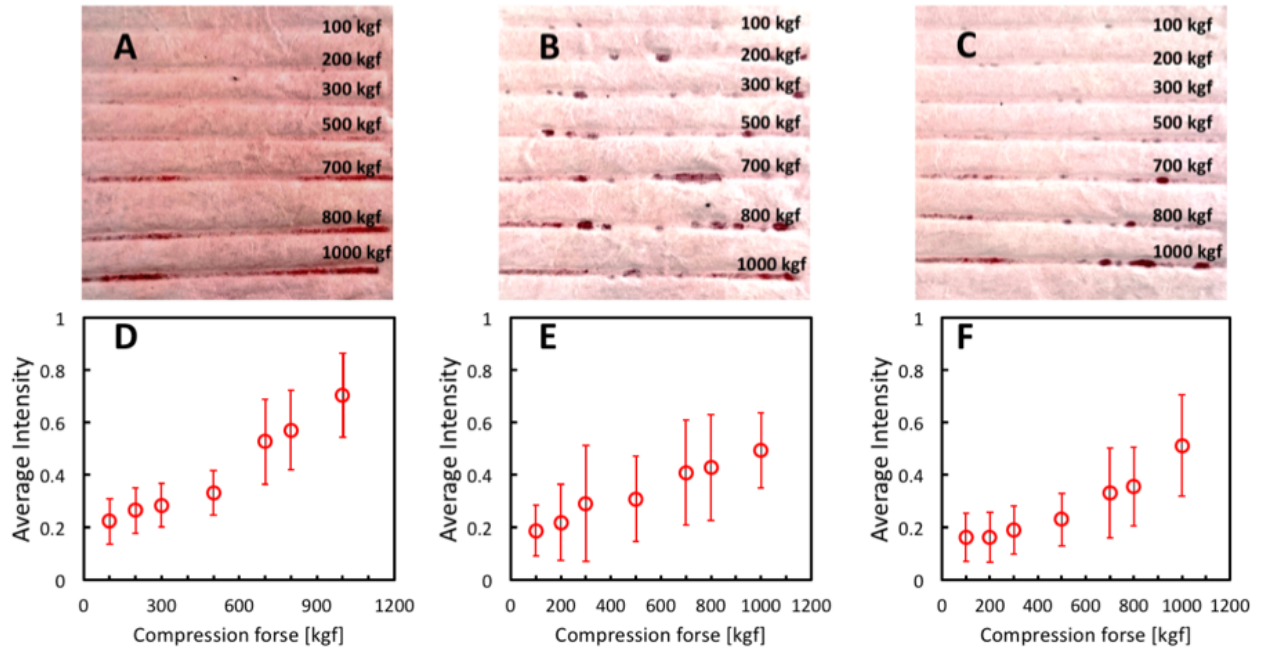
Figure 5.6. The image analysis results of critical stress-indicating patches with PVDF/Oil Red O solution A) 0.5 mL, B) 3 mL and C) 5 mL deposited as nanocapsules via AC electrospray at 8 psi air flow, 12.5 kV, 16 cm distance from the spinneret to collector, 0.009 mL/min feeding rate; and mechanochromic response intensity analysis for patches with D) 0.5 mL, E) 3 mL and F) 5 mL of PVDF/Oil Red O solution deposited as nanocapsules.
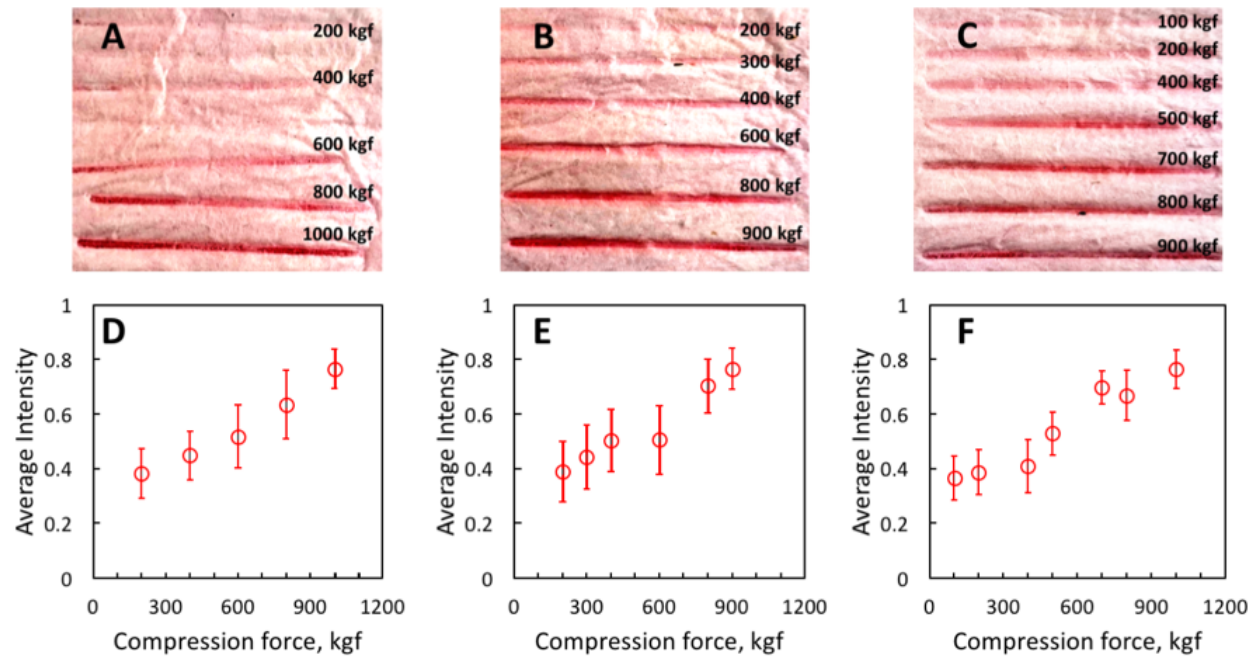
Figure 5.7. The image analysis results of critical stress-indicating patches with PS/Oil Red O solution A) 0.5 mL, B) 3 mL and C) 5 mL deposited as microcapsules via AC electrospray at 8 psi air flow, 18 kV, 18 cm distance from the spinneret to collector, 0.03 mL/min feeding rate; and mechanochromic response intensity analysis for patches with D) 0.5 mL, E) 3 mL and F) 5 mL of PS/Oil Red O solution deposited as microcapsules.

As a final step, we examined the effect of the sheath layer air flow in AC electrospray on the performance of the damage-sensing system. Two PVDF-based stress-indicating patches were fabricated utilizing conventional electrospray and AC electrospray at the same process conditions. As shown in Figure 5.8, AC-electrosprayed patches perform slightly worse and have a more heterogeneous mechanochromic response to deformation, due to a 70 % decrease in the average diameter of deposited nanocapsules. Therefore, we have demonstrated a novel, robust and scalable methodology to produce self-reporting damage-sensing composites capable of indicating critical compressive deformation, which further reaffirms the validity of our auspicious technique for single step encapsulation via AC electrospray.
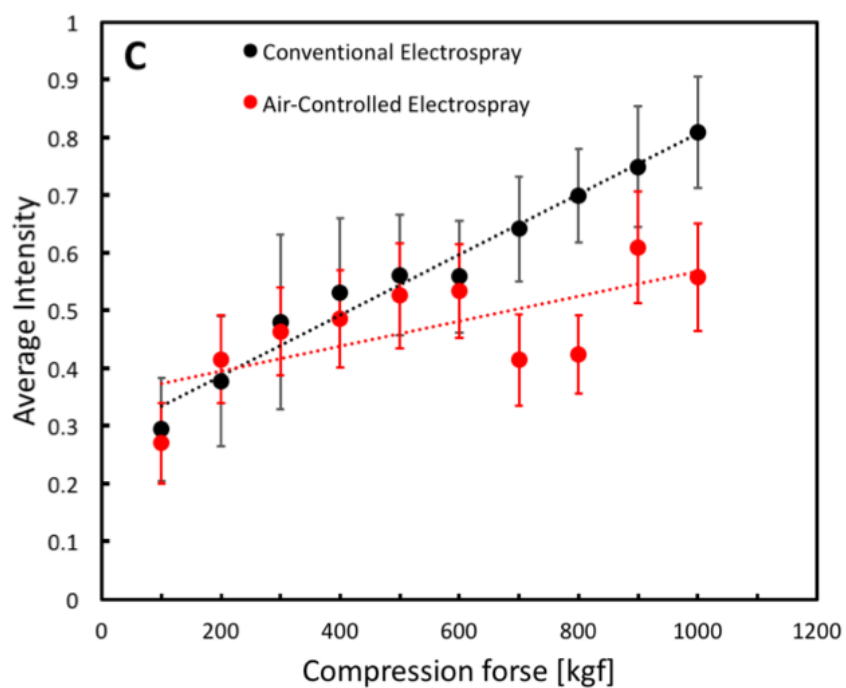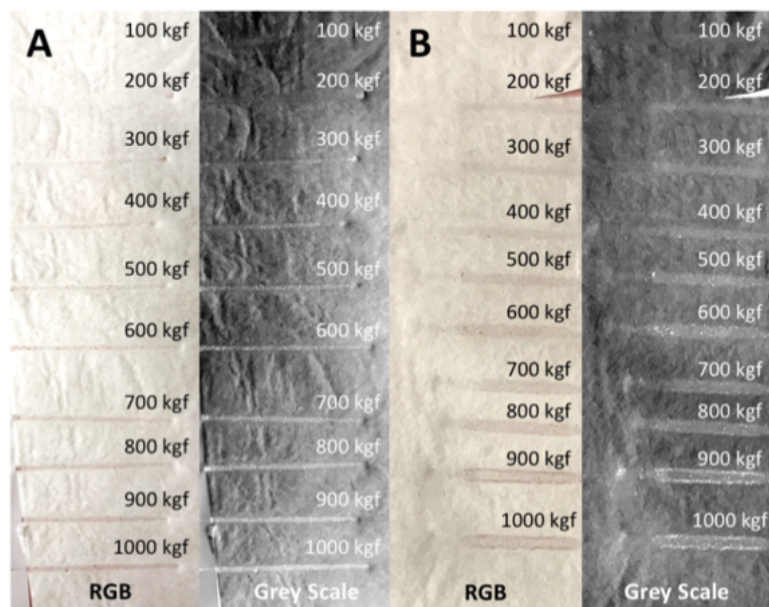
Figure 5.8. The image analysis results of critical stress-indicating patches with 1.5 mL of PVDF/Oil Red O solution deposited as nanocapsules via spraying processes. A) conventional electrospray and B) AC electrospray at 16 psi air flow, 12.5 kV, 16 cm distance from the spinneret to collector, 0.009 mL/min feeding rate; and C) mechanochromic response intensity analysis for patches fabricated via conventional electrospray and AC electrospray of PVDF/Oil Red O capsules.

## 5.4. Summary

In this work, we have demonstrated that by utilizing a circumferentially uniform air flow as a sheath layer of coaxial nozzle of a novel AC electrospraying process we can effectively control fluid atomization and mass-produce micron/nano-scale capsules. Oil Red O dye was successfully encapsulated in PVDF and PS shells, and it has been shown that capsule dimensions and morphologies can be precisely controlled by tuning AC electrospray process parameters, such as air flow rate, voltage applied to the nozzle, voltage applied to the ring electrode, distance from the ring electrode to the spinneret, and polymer solution feeding rate. Further, PVDF and PS capsules were effectively deposited on the nonwoven substrate in a single-step AC electrospraying process, and critical stress-indicating patches were fabricated. The coloring agent was released upon compressive deformation during Instron compression mode test, creating a highly distinct red color visual indication. It has been observed that the intensity of mechanochromic response increased with compressive load, and the visual feedback was more evident at higher capsule concentrations. However, AC-electrosprayed patches have a more heterogeneous mechanochromic response to deformation, compared to their conventionally–sprayed counterparts, due to a 70 % decrease in the average diameter of produced capsules. Further, in Chapter 6, we present a rigorous visualization study on the jetting behavior during novel centrifugal spinning process. The application of this new technique can overcome scalability constraints, as well as ensure economic viability and feasibility for industrial utilization.

# REFERENCES

[1]     C. Seubert, K. Nietering, M. Nichols, R. Wykoff, and S. Bollin, "An Overview of the Scratch Resistance of Automotive Coatings: Exterior Clearcoats and Polycarbonate Hardcoats," *Coatings*, vol. 2, no. 4, pp. 221–234, 2012.

[2]     M. Lonyuk, M. Bosma, A. C. Riemslag, J. Zuidema, A. Bakker, and M. Janssen, "Stone-impact damage of automotive coatings: A laboratory single-impact tester," *Prog. Org. Coatings*, vol. 58, no. 2–3, pp. 241–247, 2007.

[3]     B. R. Das, S. M. Ishtiaque, and R. S. Rengasamy, "Static Failure Mechanism of Staple Yarns: A Critical Review," *Asian J. Text.*, vol. 1, no. 1, pp. 50–58, Jan. 2011.

[4]     W. Li, C. C. Matthews, K. Yang, M. T. Odarczenko, S. R. White, and N. R. Sottos, "Autonomous Indication of Mechanical Damage in Polymeric Coatings," *Adv. Mater.*, vol. 28, no. 11, pp. 2189–2194, 2016.

[5]     C. Löwe and C. Weder, "Oligo(p-phenylene vinylene) excimers as molecular probes: Deformation-induced color changes in photoluminescent polymer blends," *Adv. Mater.*, vol. 14, no. 22, pp. 1625–1629, 2002.

[6]     B. R. Crenshaw and C. Weder, "Deformation-Induced Color Changes in Melt-Processed Photoluminescent Polymer Blends," *Chem. Mater.*, vol. 15, no. 25, pp. 4717–4724, 2003.

[7]     B. R. Crenshaw and C. Weder, "Self-assessing photoluminescent polyurethanes," *Macromolecules*, vol. 39, no. 26, pp. 9581–9589, 2006.

[8]     A. D. N. Celestine, B. A. Beiermann, P. A. May, J. S. Moore, N. R. Sottos, and S. R. White, "Fracture-induced activation in mechanophore-linked, rubber toughened PMMA," *Polymer*, vol. 55, no. 16, pp. 4164–4171, 2014.

[9]     Y.-K. Song, K.-H. Lee, W.-S. Hong, S.-Y. Cho, H.-C. Yu, and C.-M. Chung,

"Fluorescence sensing of microcracks based on cycloreversion of a dimeric anthracene moiety," *J. Mater. Chem.*, vol. 22, no. 4, p. 1380, 2012.

[10]   S. Y. Cho, J. G. Kim, and C. M. Chung, "A fluorescent crack sensor based on cyclobutane-containing crosslinked polymers of tricinnamates," *Sensors Actuators, B Chem.*, vol. 134, no. 2, pp. 822–825, 2008.

[11]   D. A. Davis, A. Hamilton, J. Yang, L. D. Cremar, D. Van Gough, S. L. Potisek, M. T. Ong, P. V Braun, T. J. Martínez, S. R. White, J. S. Moore, and N. R. Sottos, "Force-induced activation of covalent bonds in mechanoresponsive polymeric materials.," *Nature*, vol. 459, no. 7243, pp. 68–72, 2009.

[12]   Y. H. Lee, F. Mei, M. Y. Bai, S. Zhao, and D. R. Chen, "Release profile characteristics of biodegradable-polymer-coated drug particles fabricated by dual-capillary electrospray," *J. Control. Release*, vol. 145, no. 1, pp. 58–65, 2010.

[13]   B. Di Credico, G. Griffini, M. Levi, and S. Turri, "Microencapsulation of a UV-responsive photochromic dye by means of novel uv-screening polyurea-based shells for smart coating applications," *ACS Appl. Mater. Interfaces*, vol. 5, no. 14, pp. 6628–6634, 2013.

[14]   S. A. Odom, A. C. Jackson, A. M. Prokup, S. Chayanupatkul, N. R. Sottos, S. R. White, and J. S. Moore, "Visual Indication of Mechanical Damage Using Core − Shell Microcapsules," *ACS Appl. Mater. Interfaces*, vol. 3, pp. 4547–4551, 2011.

[15]   S. Vidinejevs, A. N. Aniskevich, A. Gregor, M. Sjoberg, and G. Alvarez, "Smart polymeric coatings for damage visualization in substrate materials," *J. Intell. Mater. Syst. Struct.*, vol. 23, no. 12, pp. 1371–1377, 2012.

[16]   J. W. C. Pang and I. P. Bond, "'Bleeding composites' - Damage detection and self-repair

using a biomimetic approach," *Compos. Part A Appl. Sci. Manuf.*, vol. 36, no. 2 SPEC. ISS., pp. 183–188, 2005.

[17]   J. W. C. Pang and I. P. Bond, "A hollow fibre reinforced polymer composite encompassing self-healing and enhanced damage visibility," *Compos. Sci. Technol.*, vol. 65, no. 11–12, pp. 1791–1799, 2005.

[18]   S. Gouin, "Microencapsulation: Industrial appraisal of existing technologies and trends," *Trends Food Sci. Technol.*, vol. 15, no. 7–8, pp. 330–347, 2004.

[19]   I. G. Loscertales and A. M. Gañán-Calvo, "Micro / Nano Encapsulation via Electrified Coaxial Liquid Jets," *Science*, vol. 295, no. 2002, pp. 1695–1698, 2002.

[20]   S. N. Rodrigues, I. Fernandes, I. M. Martins, V. G. Mata, F. Barreiro, and A. E. Rodrigues, "Microencapsulation of limonene for textile application," *Ind. Eng. Chem. Res.*, vol. 47, no. 12, pp. 4142–4147, 2008.

[21]   S. Ghayempour and S. M. Mortazavi, "Fabrication of micro-nanocapsules by a new electrospraying method using coaxial jets and examination of effective parameters on their production," *J. Electrostat.*, vol. 71, no. 4, pp. 717–727, 2013.

[22]   A. Jaworek and A. T. Sobczyk, "Electrospraying route to nanotechnology: An overview," *J. Electrostat.*, vol. 66, pp. 197–219, 2008.

[23]   S. T. Yohe and M. W. Grinstaff, "A facile approach to robust superhydrophobic 3D coatings via connective-particle formation using the electrospraying process.," *Chem. Commun.*, vol. 49, no. 8, pp. 804–6, 2013.

[24]   I. Uematsu, H. Matsumoto, K. Morota, M. Minagawa, A. Tanioka, Y. Yamagata, and K. Inoue, "Surface morphology and biological activity of protein thin films produced by electrospray deposition," *J. Colloid Interface Sci.*, vol. 269, no. 2, pp. 336–340, 2004.

[25]  Q. Guo, J. P. Mather, P. Yang, M. Boden, and P. T. Mather, "Fabrication of Polymeric Coatings with Controlled Microtopographies Using an Electrospraying Technique.," *PLoS One*, vol. 10, no. 6, pp. 1–14, 2015.

[26]  A. A. van Zomeren, E. M. Kelder, J. C. M. Marijnissen, and J. Schoonman, "The Production of Thin Films of LiMn2O4 by Electrospraying," *J. Aerosol Sci.*, vol. 25, no. 6, pp. 407–410, 1994.

[27]  S. Maheshwari, N. Chetwani, and C. Hsueh-Chia, "Alternating current electrospraying," *Industrial and Engineering Chemistry Research*. pp. 9358–9368, 2009.

[28]  E. Burkarter, C. K. Saul, F. Thomazi, N. C. Cruz, L. S. Roman, and W. H. Schreiner, "Superhydrophobic electrosprayed PTFE," *Surf. Coatings Technol.*, vol. 202, no. 1, pp. 194–198, 2007.

[29]  D. An, A. Warning, K. G. Yancey, C.-T. Chang, V. R. Kern, A. K. Datta, P. H. Steen, D. Luo, and M. Ma, "Mass production of shaped particles through vortex ring freezing," *Nat. Commun.*, vol. 7, p. 12401, 2016.

[30]  D. Duft, T. Achtzehn, R. Müller, B. a Huber, and T. Leisner, "Coulomb fission: Rayleigh jets from levitated microdroplets.," *Nature*, vol. 421, no. 6919, p. 128, 2003.

[31]  A. Jaworek, "Electrospray droplet sources for thin film deposition," *J. Mater. Sci.*, vol. 42, no. August 2004, pp. 266–297, 2007.

[32]  N. V. N. Jyothi, P. M. Prasanna, S. N. Sakarkar, K. S. Prabha, P. S. Ramaiah, and G. Y. Srawan, "Microencapsulation techniques, factors influencing encapsulation efficiency.," *J. Microencapsul.*, vol. 27, no. 3, pp. 187–197, 2010.

[33]  Y. Zhmayev, S. Pinge, G. Shoorideh, G. L. Shebert, P. Kaur, H. Liu, and Y. L. Joo, "Controlling the Placement of Spherical Nanoparticles in Electrically Driven Polymer Jets

and its Application to Li-Ion Battery Anodes," *Small*, pp. 1–11, 2016.

[34] D. H. Reneker, A. L. Yarin, H. Fong, and S. Koombhongse, "Bending instability of electrically charged liquid jets of polymer solutions in electrospinning," *J. Appl. Phys.*, vol. 87, no. 9, p. 4531, 2000.

[35] A. L. Yarin, S. Koombhongse, and D. H. Reneker, "Bending instability in electrospinning of nanofibers," *J. Appl. Phys.*, vol. 89, no. 5, p. 3018, 2001.

[36] J. Xie and C. H. Wang, "Electrospray in the dripping mode for cell microencapsulation," *J. Colloid Interface Sci.*, vol. 312, no. 2, pp. 247–255, 2007.

[37] M. D. Paine, M. S. Alexander, and J. P. W. Stark, "Nozzle and liquid effects on the spray modes in nanoelectrospray," *J. Colloid Interface Sci.*, vol. 305, no. 1, pp. 111–123, 2007.

# CHAPTER 6

# THE JETTING BEHAVIOR OF VISCOELASTIC BOGER FLUIDS DURING CENTRIFUGAL SPINNING

## 6.1. Introduction

Fibers of different polymers have been produced for almost a century using different spinning processes, such as wet spinning, dry spinning and melt spinning. In these processes the pressure driven extrusion of a viscous polymer fluid is used to produce fibers in the range from 10 to 500μm in diameter. [1] Electrospinning and fiber blowing methods are more recent, and used for submicron fiber production. [2–7] Centrifugal spinning is a novel process for producing nanoscale or submicron fibers, where the centrifugal force is utilized to accelerate and elongate a fluid jet. [8–10] The resulting fibers have a myriad of modern and potential applications in such areas as advanced electronics, composite materials, filtration, and biomedical engineering, due to their high surface area to mass ratios. [11–14]

Similarly to electrospinning process, which uses electric force to spin the fluid jet, centrifugal spinning has two main phases. [15, 16] The first stage (the "stable jet" stage) starts when the fiber leaves the edge of the rotating disk, follows a spiral motion, and ends at the onset of non-spiral motion. The second stage is the instability region, where the polymer jet undergoes a bending instability, which is commonly referred to as a "whipping motion" in electrospinning. [16–18] The bending instability in centrifugal spinning is an aerodynamically driven non-spiral motion, which occurs when the polymer jet is light enough to be affected by the air drag. The bending/whipping instability is accompanied by rapid solvent evaporation and solidification of the polymer jet. After solidification, fibers are collected on the collector plate. The distance between

collector and rotating disk does not affect any body forces, and can be chosen based on the extensibility of fibers and time it takes to evaporate the solvent.

The main advantage of the centrifugal spinning process is the high production rate and low process cost, which gives a potential for future industrial utilization. Productivity has been an issue for well-established spinning process for nanofibers, such as electrospinning (0.01-0.1 mL/min per nozzle), however centrifugal spinning can offer a much higher production rate (10-20 mL/min per nozzle in the current study). It has been shown that crystallinity and polymer chain alignment in fibers can be improved, especially in cases when the electric force is effectively utilized near the spinline in electrospinning processes. [9, 19] Centrifugal spinning would also provide an increase in crystallinity and chain orientation without the implications of the electrohydrodynamic quenching by the electric field. [20]

In this paper, we focus on the experimental visualization of the fluid flow and examine the effects of viscoelasticity, driving force and flow rate on the initial thinning of the polymer jet and the contour shapes and radii. The initial thinning behavior can elucidate the interaction between forces acting on the polymer jet, and it is a good starting point for the comparison with simulation, due to the absence of instability. The effect of the fluid properties and experimental conditions on the maximum contour radii is beneficial for the optimization of fiber collection. The most optimal collection region can be predicted for a specific fluid based on experimental conditions. A thorough physical explanation is provided to explain the behavior observed in experiments.

We perform centrifugal spinning experiments using both Newtonian and non-Newtonian viscoelastic fluids. Polyisobutylene (PIB)-based Boger fluids are used to examine the effect of viscoelasticity, and this system has a multitude of advantages for the current study. This Boger fluid was extensively used in viscoelastic fluid flow studies. [16, 21–26] The test fluid has a

143

constant viscosity over a wide range of shear rates, which allows one to not consider shear thinning behavior. However, at the same time it exhibits strong elasticity, which makes it advantages for current study, regarding the fact that most of the fluids used in spinning processes are highly viscoelastic. One can tailor the fluid properties and elasticity by changing the composition of the fluid. The solvent is nonvolatile, which eliminates the need to consider mass transfer effects.

Experimental results from centrifugal spinning experiments of Boger fluids are compared with simulation results predicted by the discretized modeling [27] which was successfully applied to the modeling of the electrospinning process. [17,18,22] The simulation prediction is in good agreement with the experimental results. The model is sensitive to driving force and the prediction is generally better for the higher values of angular velocity. The effect of viscoelasticity, driving force and flow rate on the initial thinning behavior are then compared to the results from electrospinning process, which was rigorously studied by Carroll *et al.* [16], and repeated in this work.

**6.2. Experimental Procedure**

*6.2.1. Test Fluids*

The fluids used in the current study are viscoelastic PIB/PB Boger fluids with different compositions, and a low molecular weight polybutene (PB) which was used to examine the effects of driving force and flow rate on the Newtonian fluid. High molecular weight PIB (Aldrich, MW=$10^6$) was dissolved in a small amount of trichloroethylene (TCE) and after dissolution had occurred, the solutions were diluted to desired concentrations by adding PB (Sigma, MW=320) as a solvent. The resulting solutions were stirred overnight and left under vacuum for weeks to

evaporate TCE and obtain the desired rheological properties. [16, 21] In this manner 2000ppm, 4000ppm and 8000ppm Boger fluid solutions were prepared.

The viscosity and relaxation time of Boger fluids were measured as described in previous work, and density and surface tension for simulation purposes were taken from the literature [16] and are summarized in Table 6.1. The properties of Newtonian PB solution are listed for comparison, and the rheological properties of Boger fluids can be found in the Supporting Information.

Table 6.1. Key properties of test fluids [16]

| Concentration of PIB in PB solvent | Density, [kg m$^{-3}$] | Viscosity, [Pa s] | Surface tension, [N m$^{-1}$] | Relaxation time, [s] |
|---|---|---|---|---|
| 2000ppm | 850 | 0.072 | 1.46 x 10$^{-2}$ | 2.50 x 10$^{-3}$ |
| 4000ppm | 850 | 0.102 | 1.46 x 10$^{-2}$ | 3.11 x 10$^{-3}$ |
| 8000ppm | 850 | 0.175 | 1.46 x 10$^{-2}$ | 6.25 x 10$^{-3}$ |
| Newtonian (PB) | 850 | 0.02805 | 1.46 x 10$^{-2}$ | - |

*6.2.2.  Centrifugal Spinning Setup*
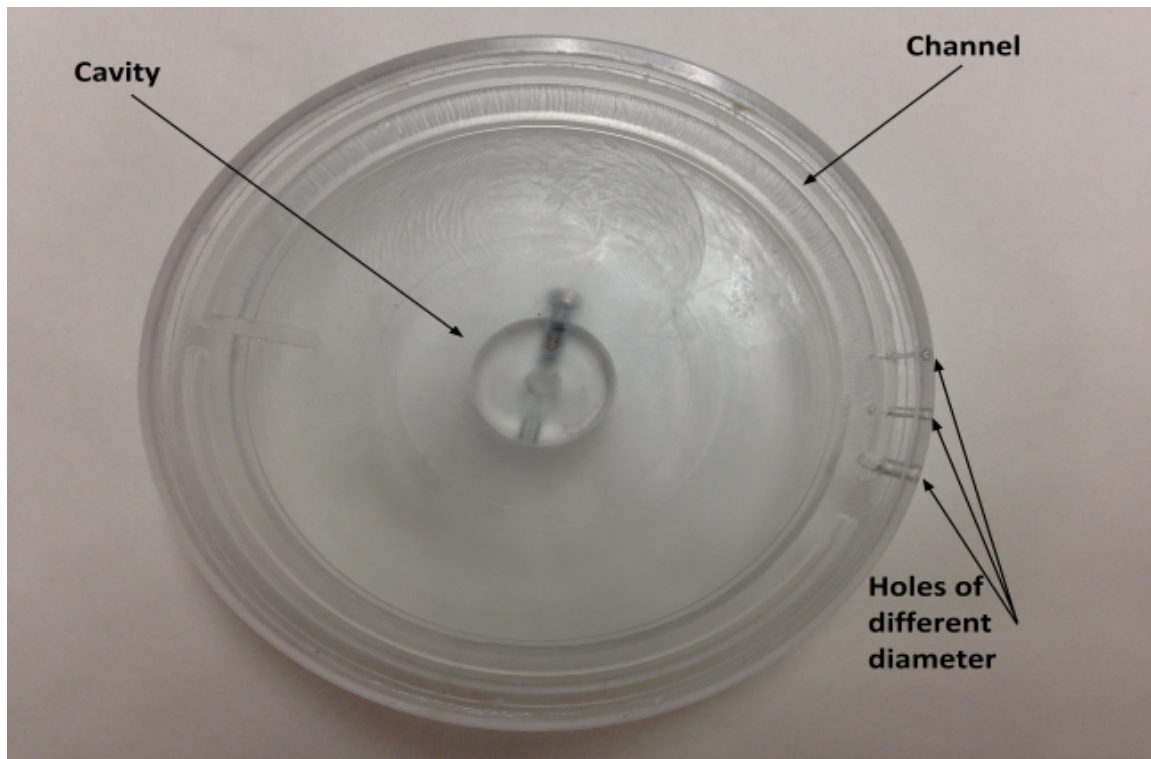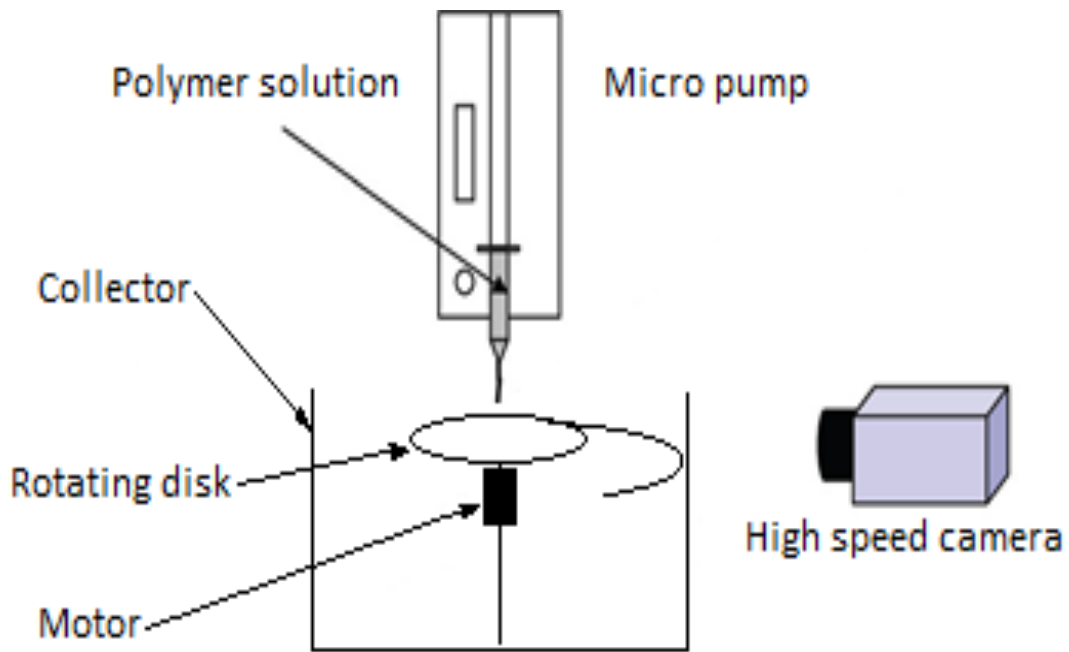


Figure 6.1. Centrifugal spinning setup and custom made disk.

The centrifugal spinning setup is depicted in Figure 6.1. The system consists of a custom made disk with perforations of different diameters, and it is attached to a motor which is mounted on a laboratory stand. The stand is firmly attached to a table to prevent any oscillations and fluctuations during spinning. The setup is isolated in a plastic container to prevent spilling and reduce the effect of air drag from external sources. The walls of container are covered with aluminum foil which serves as a collector. A digitally controlled syringe pump (Harvard Apparatus, PHD 2000) is used to pump fluid out of a syringe nozzle onto a rotating disk at a set rate (10-15 ml/min in current study). The fiber spinning occurs in the gap between the disk and the collector and the distance can be adjusted based on the jet extensibility and solvent evaporation rate.

The custom made disk is depicted in Figure 6.1. The fluid is pumped to a cavity inside of the disk, it travels radially outward to a thin circular channel to prevent die swell and then on to the orifice of a certain diameter. The disk is sealed with a transparent cover from the top to prevent spilling and provide a possibility to observe the flow in the channel. The regular centrifugal spinning setup utilizes a flat disk, but the custom made version is required to visualize a single jet behavior.

To visualize and examine different regions of the flow, a high speed camera was used (RedLake MotionPro HS-3 with Nikon MICRO NIKORR 60mm 1:2:8 lens). Intensive illumination was provided by a 500 W lamp, which was covered with wax paper to disperse light. The camera operated at 1000 frames per second, 30 μs exposure time and the aperture varied from $f/2.8$ to $f/5.6$. The obtained images were digitized using MotionStudio x64 software and analyzed using ImageJ.

*6.2.3. Experimental Conditions*

PIB/PB Boger fluids were spun in the centrifugal setup under the following conditions: disk rotation speed = 1300 – 3750 RPM; flow rate = 10 – 15 mL/min; nozzle radius = 0.5 mm; channel width = 1.5 mm; disk radius = 32.5 mm. The dimensions of the disk were held constant, and the feeding rate and rotation speed were changed in order to test the effect of fluid flow rate and centrifugal force on the polymer jet. The custom made disk has perforations of different diameters, but the 0.5 mm nozzle radius was found to be the most suitable one for high speed camera visualization.

**6.3. Results and Discussions**

Among various fluid properties and spinning conditions, we selected the viscoelasticity, flow rate and rotation speed as the key parameters in the present study, and their effects on the jetting behavior during the centrifugal spinning have been investigated.

*6.3.1. The effect of viscoelasticity*

The effect of viscoelasticity was probed by changing the polymer relaxation time through the concentration of the Boger fluid. The effect of relaxation time is investigated through its dimensionless counterpart – Deborah number ($De$), obtained by utilizing the characteristic scales, which along with other parameters are summarized in Table 6.2. The parameters are as follows: $a_0$ is the radius of the orifice (nozzle), $R_{disk}$ is the disk radius, $\lambda$ is the relaxation time, $t_0$ is the characteristic time (defined in Table 6.2), $\rho$ is the density, $\mu$ is the viscosity, $\Omega$ is the angular velocity, $\varepsilon_D$ is the permittivity of the free space, $E_0$ is the electric field strength and $U_0$ is the initial velocity (at the orifice outlet). The relative importance of centrifugal force is represented by $Rb$, Rossby number, which is inversely proportional to centrifugal force. High-speed camera images

were used to calculate the evolution of the jet radius along the contour length for centrifugal spinning, and shown in Figure 6.2.

Table 6.2. Characteristic scales and dimensionless groups

| Characteristic scales | | | Dimensionless groups |
|---|---|---|---|
| Radius | Time | Length | $\mathrm{De} = \lambda U_0 / a_0$ ; $\mathrm{Re} = \rho U_0 a_0 / \mu$ ; $\mathrm{Rb} = 1 / \Omega t_0$ ; |
| $a_0$ | $t_0 = a_0 / U_0$ | $R_{disk}$ | $\varepsilon_E = \overline{\varepsilon_D} E_0^2 / \rho U_0^2$ |
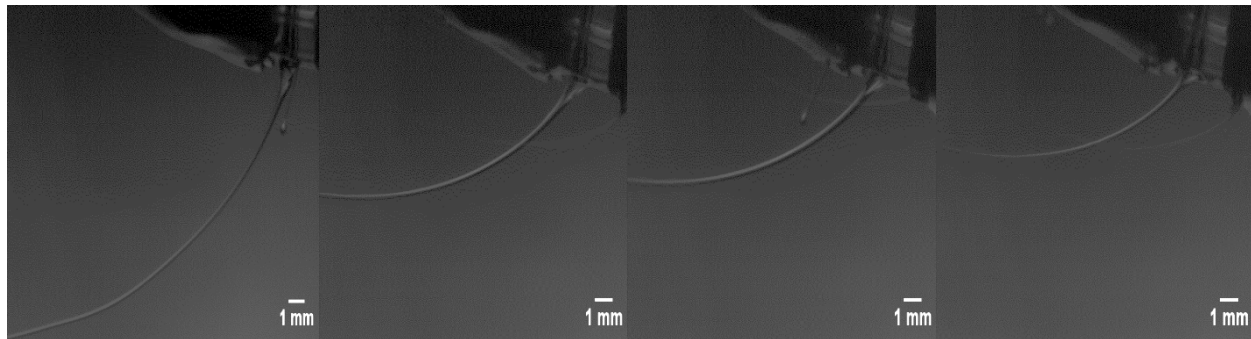


Figure 6.2. The effect of viscoelasticity on the initial thinning behavior of Boger fluids. Centrifugal spinning at 12.5 ml/min and 1770 RPM of Newtonian PB, 2000ppm, 4000ppm and 8000ppm from left to right respectively.

It can be seen from Figure 6.3, that increasing the degree of viscoelasticity will result in faster thinning of the polymer jet in the early stage of spinning, and it is expected that thinning will slow down as the jet moves farther from the spinneret, resulting in thicker fibers for more viscoelastic fluids in the end. The behavior can be better comprehended by studying the stress

within the jet. When the jet is under strain of centrifugal and viscoelastic forces, the stress will be observed to have an inward radial component and an axial component, which will result in thinning and stretching respectively. The radial component of the stress is a compressive force, which develops instantly and becomes dominant in the initial stage, and results in faster thinning for more viscoelastic fluids. However, a more rapid increase in extensional viscosity will result in thicker jets for high *De* fluids in the final stage of spinning as observed in Figure 6.3 (b). [16] The similar viscoelastic effect of initial rapid thinning, followed by retardation of thinning was observed in other spinning processes including electrospinning. [16] Newtonian PB was centrifugally spun and the slowest initial thinning was observed, which supports the reasoning used in this section. We note that *Re* decreases for more viscoelastic fluids, due to the increase in the fluid viscosity (Figure 6.3). In the previous modeling studies for electrospinning it has been shown that the thinning of the jet slows down when *Re* decreases. [16, 28] If *Re* was constant for different concentrations of test fluids (similar viscosity), the fiber would thin even faster at the initial stage, which means that elasticity (*De*) has a substantial effect on the initial jet thinning.

As seen in Figure 6.4, the fluid viscoelasticity has a significant effect on the jet contour radius, which is the distance from the disk to the polymer jet. It is observed that the maximum radius of the contour for the same angular velocity, will decrease with increasing *De*. This behavior can be explained by the elastic hoop stress, which arises from the curvilinear trajectory and non-Newtonian behavior of the fluid. The hoop stress ($\tau_{hoop} = \dfrac{\tau_{zz} - \tau_{rr}}{R/d}$, where $\tau_{zz}$ and $\tau_{rr}$ are the axial and radial stresses, respectively, and $R/d$ is the ratio of the contour radius to the jet diameter) is more significant for higher De, due to the increase in the axial stress. The decrease in *Re* by the increase of viscosity for higher concentrations of Boger fluids, when combined with the hoop stress results in smaller values of contour radii. The effect of the air drag, which is triggered by a fast rotation and the appearance

150

of the air vortex, supplements the effect of viscoelasticity and causes the jet to move closer to the spinneret.
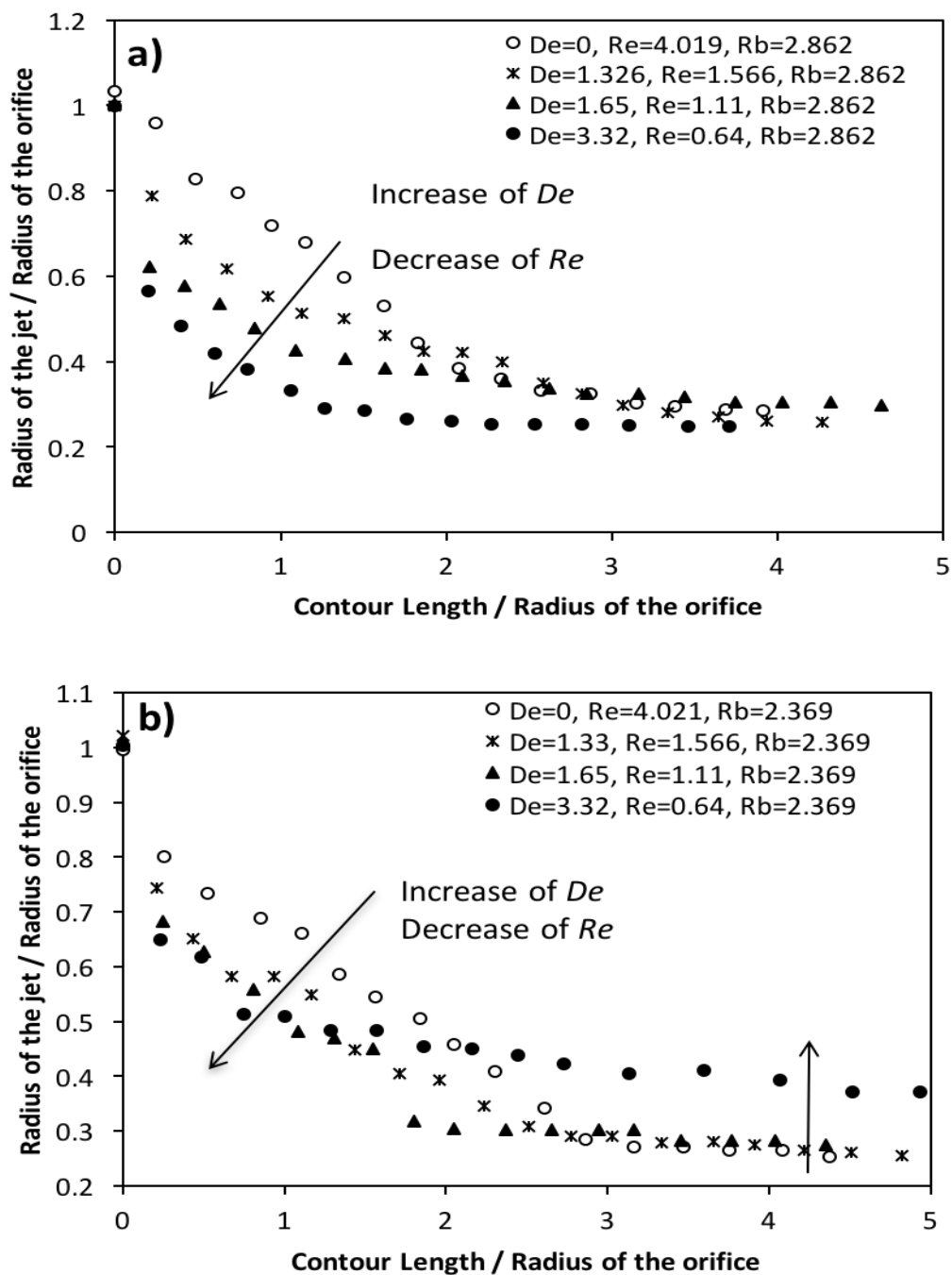


Figure 6.3. The evolution of the radius of the polymer jet during centrifugal spinning for different *De:* a) 12.5 ml/min, 1770 RPM and b) 12.5 mL/min, 2140 RPM.
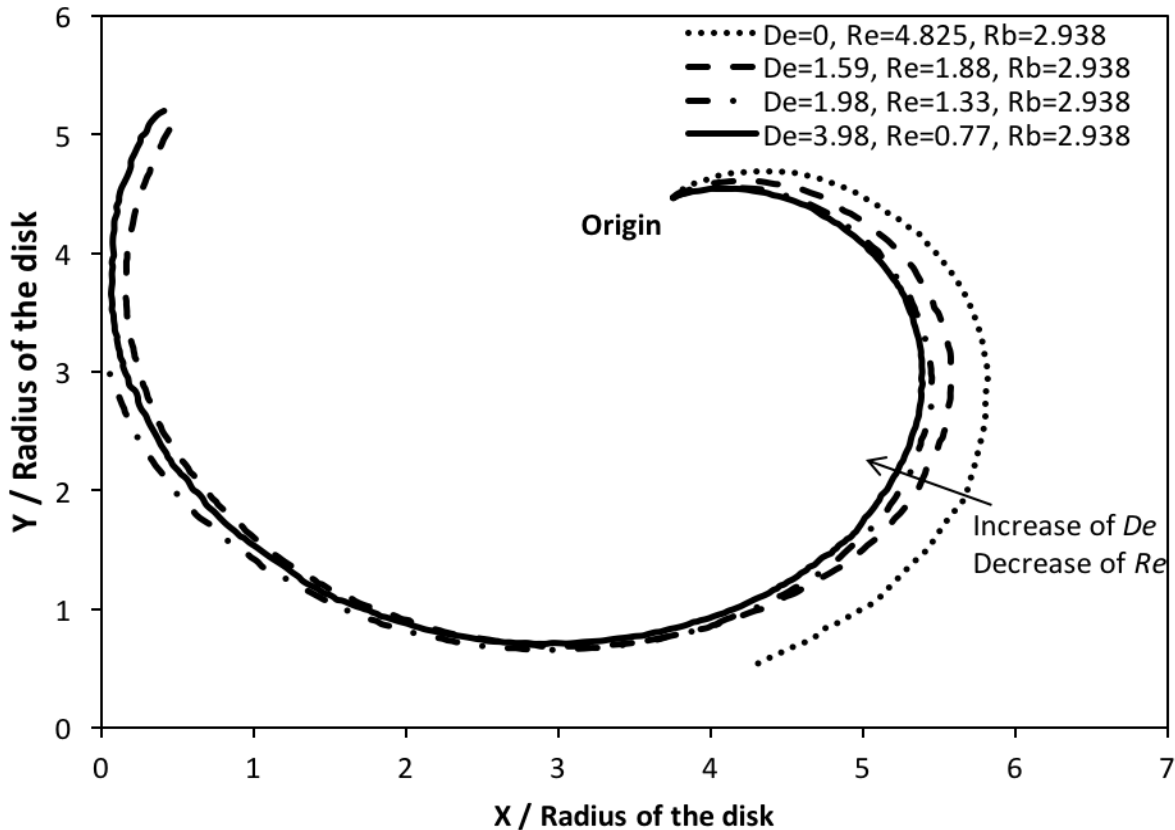
Figure 6.4. Trajectories of contour radii during centrifugal spinning (15 mL/min, 2070 RPM) of Newtonian PB, 2000ppm, 4000ppm and 8000ppm Boger Fluids.

### 6.3.2. *The effect of the flow rate*

The effect of the flow rate was probed by changing the pumping rate in centrifugal spinning. The concentrations and angular velocities were kept constant for the current set of experiments. It can be seen from Figure 6.5 that the initial thinning is faster for slower flow rates (small $Re$), which matches the earlier observations from electrospinning studies. [16] The effect of the flow rate is coupled with the effects of the viscoelasticity and driving force, which can be observed from the change of $De$ and $Rb$, which is inversely proportional to centrifugal force, with the change of the flow rate. The relation is through the initial velocity of the polymer jet, which is

proportional to the change of the flow rate. It has been noticed that the initial thinning for 10 mL/min and 12.5 mL/min is very similar, which may be explained by compensation between centrifugal and viscoelastic forces acting on the polymer jet at the initial stage of thinning.

It should be noted that the flow rate did not affect the trajectory of the jet at the initial stage of centrifugal spinning (Figure 6.6). We would expect a higher value of contour radius for 15 mL/min, because the initial velocity is higher than for 10 or 12.5 mL/min at the same nozzle size. However, as observed in Figure 6.5, the initial thinning is faster at a lower flow rate, which leads to the decrease of the cross-sectional area of the jet and thus the increase in jet velocity. The resulting jet trajectories are very similar at three different flow rates. Nonetheless, there is a deviation in the contour radius down the stream, which can be observed from the 15 mL/min case.
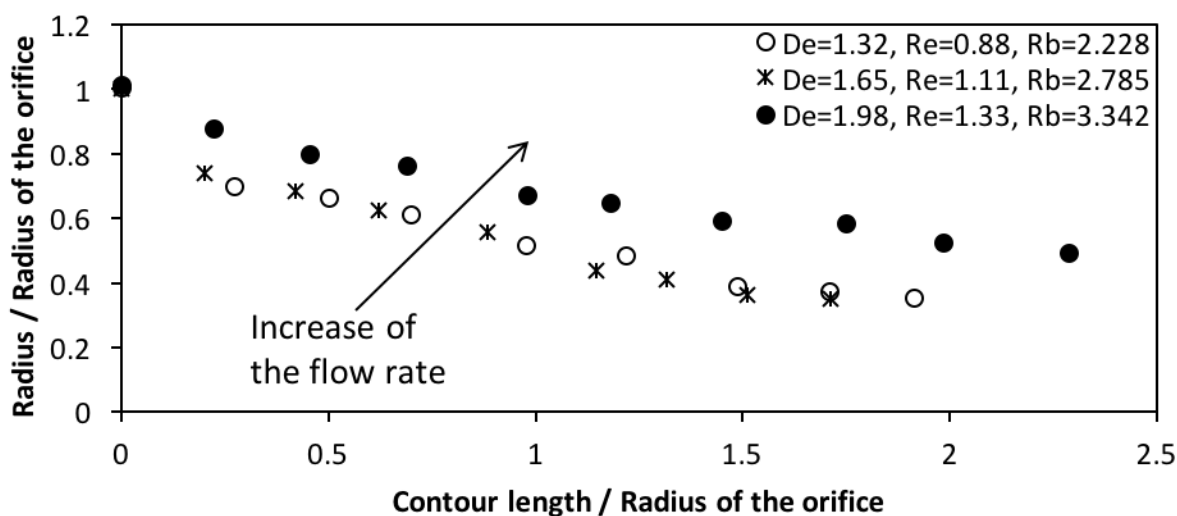


Figure 6.5. The effect of the flow rate on the initial thinning behavior during Centrifugal spinning of the 4000ppm Boger fluid at 1820 RPM (10, 12.5, 15 mL/min).
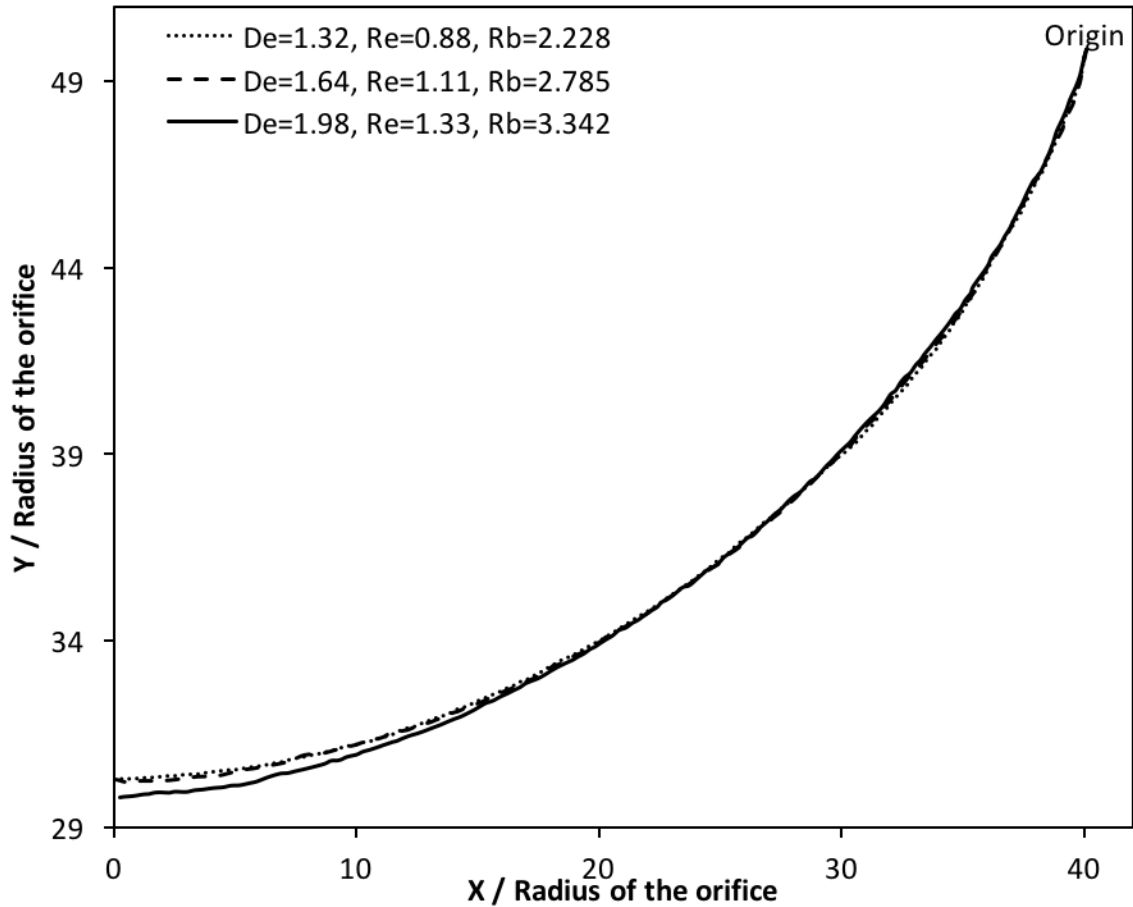
Figure 6.6. The effect of the flow rate on the initial contour radii during the Centrifugal spinning process of 4000ppm Boger fluid at 1820 RPM.

### 6.3.3. The effect of driving force

The next parameter we examine is the influence of the driving force, *i.e.* centrifugal force, on the initial thinning and contour trajectories and radii. The rotation speed of the disk was changed in order to examine the effect of the centrifugal force. Newtonian PB, 2000ppm, 4000ppm and 8000ppm Boger fluids were centrifugally spun at the flow rate of 12.5 mL/min at two different rotation speeds (1770 RPM and 2140 RPM) (Figure 6.2), and at 15 mL/min at three different rotation speeds (1300, 1540 and 1740 RPM) to examine the effect of driving force on the contour

of the polymer jet. Rossby number (*Rb*), is the dimensionless equivalent of the inverse of centrifugal force.

One would expect the jet to thin faster with the increase of the driving force, and it is observed that more rapid thinning occurs at higher rotation speed (i.e. low *Rb* number) for Newtonian fluid. However, as the concentration of PIB in Boger fluid (and thus the viscoelasticity) is increased, the strain hardening due to a rapid increase in the extensional viscosity becomes significant. Hence, it is observed that the thinning becomes slower down the stream with increasing the viscoelasticity (see Figure 6.7). [7, 16] As a result, for highly viscoelastic 8000ppm Boger fluid the strain hardening becomes significant almost instantly. The final fiber dimensions would be still smaller for higher rotation speeds, but the initial thinning exhibits the opposite trend especially for highly viscoelastic fluid jet. It can be seen that for Newtonian fluid the effect of the extensional viscosity is negligible, whereas for highly viscoelastic 8000ppm Boger fluid the strain hardening becomes significant almost instantly. This behavior can be explained by the axial stress evolution in the extensional flow of Boger fluids, which is slower and less in magnitude for smaller De, resulting in slower strain hardening initially. [16]

Analogously to the jet thinning observations, the centrifugal force has a significant effect on contour radii during centrifugal spinning process. As we increase the rotation speed during the spinning of viscoelastic Boger fluid – the jet tends to move closer to the disk (Figure 6.8). The behavior can be well explained by the increase in the extensional viscosity and therefore in axial stress, which is the response to stretching. The hoop stress becomes more pronounced with the increase in axial component of stress and pulls the polymer jet closer to the disk, which results in smaller contour radii for higher rotation speeds. It can be observed that there is a range of parameters for which hoop stresses can be counterbalanced by stresses and radii for different

rotational speeds, resulting in similar trajectory profiles. Due to a convoluted nature of interactions between forces acting on the jet, therefore different rates of thinning and axial stress evolution for De=1.98 (Figure 6.8), there is a similarity in jet trajectory profiles. The air drag effect becomes more pronounced when the rotation speed is increased. The air vortex is stronger and pulls the jet towards the disk, which was observed even in the case of Newtonian fluid. [27] When rotation speed is significantly increased – the polymer jet can straighten and break up, which means that viscoelastic force was not significant enough to oppose centrifugal force. This behavior was noticed for both Newtonian and viscoelastic fluids, and the critical rotation speed strongly depends on viscoelasticity. Similar increase of the contour radii with the increase of the rotation speed during the forced spinning of PEO was reported by Padron *et al*. [8], but the range of the rotation speeds in their study was much higher.
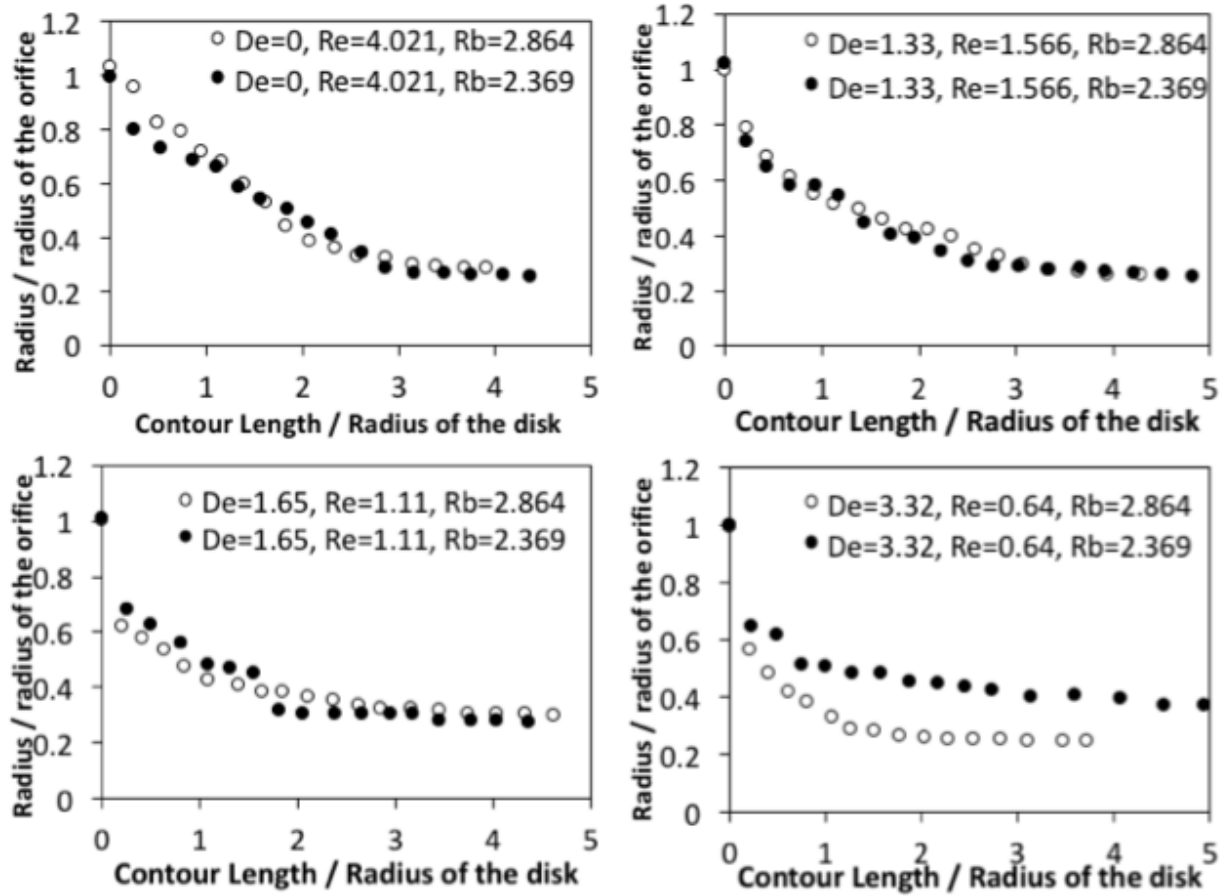
Figure 6.7. Influence of the rotation speed on the thinning behavior during centrifugal spinning of Newtonian PB and three viscoelastic Boger fluids (12.5 mL/min flow rate and 1770 and 2140 RPM).
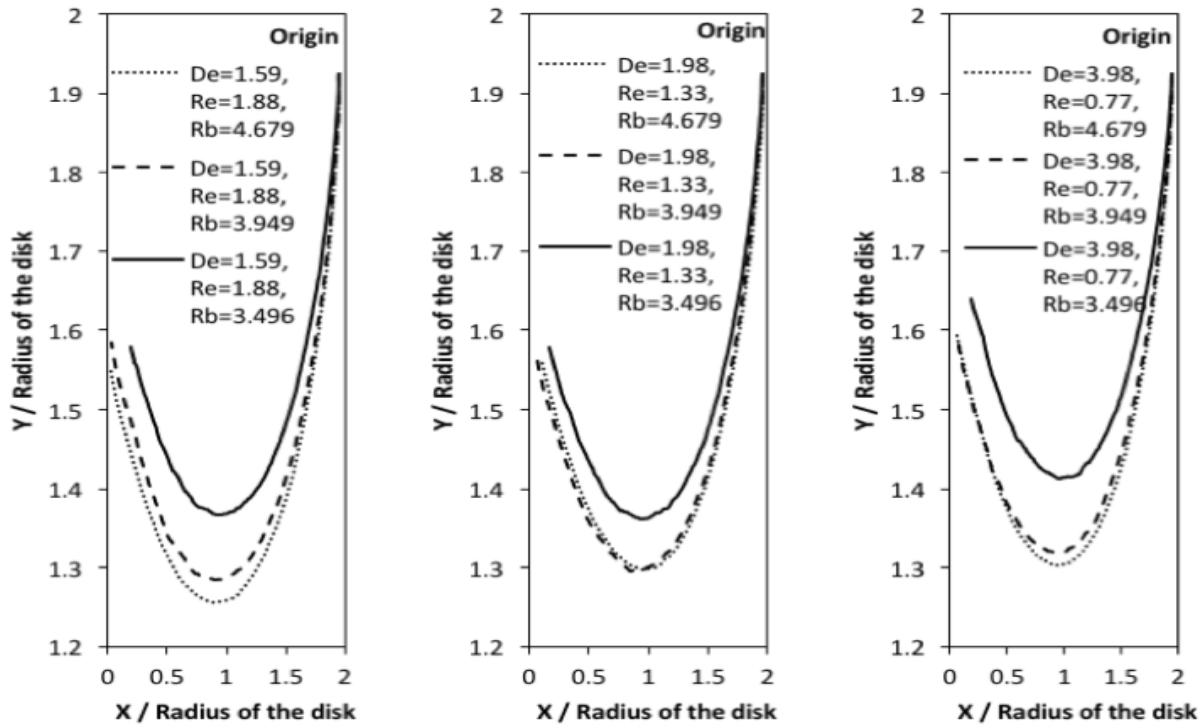
Figure 6.8. The effect of rotation speed on the contour trajectory during centrifugal spinning of three viscoelastic Boger fluids (15 mL/min flow rate at 1300, 1540 and 1740 RPM).

## 6.4. Comparison of Experiments and Simulations

The discretized modeling based on the bead-spring approach was applied to simulate the three-dimensional curvilinear motion of the polymeric jet in centrifugal spinning process. First proposed by Reneker *et al*., [17] and further studied by Carroll and Joo [22], it proved to be a feasible approach for the simulation of the rapid whipping motion as well as the initial thinning behavior during electrospinning. The main difference in this model for centrifugal spinning system compared to electrospinning is the incorporation of rotational motion of the fiber due to the rotating disk. Also, there is no electric force or charge conservation involved for centrifugal spinning but instead centrifugal force is applied. Moreover, another change in this model is simulating the polymer flow in the nozzle to measure the initial stress acting on the the fiber due to shear stress

in the nozzle. This was not present in the previous model for electrospinning but can be applied to it to get a better prediction. In discretized modeling, the jet is considered to be a series of discrete beads connected by viscoelastic springs. Each bead is pulled by its neighboring connector elements and a smooth trajectory can be formed. By solving Newton's second law of motion for each bead, it is possible to trace a curvilinear path of the polymeric jet.

In the discretized simulation, the beads are introduced at a small distance near the exit in the nozzle to analyze the viscoelastic flow of the polymer jet before it is ejected from the rotating disk. The motion of these beads in the nozzle is due to viscoelastic, capillary and centrifugal forces. We have the shear stress acting on the polymer jet due to the no slip condition near the walls of the nozzle. Along with the shear, the polymer also experiences the extensional deformation due to the centrifugal force. The tension developed due to this extension of the polymer persists even after the jet is ejected from the exit.

Although the simulation is sensitive to the force balance among centrifugal, capillary and viscoelastic forces near the nozzle, it overcomes some difficulties encountered in continuum modeling, such as stiffness due to the nonlinearity of the differential equations and complexity in describing three dimensional jet behavior. [29–34] The detailed modeling procedure and preliminary comparison with experimental results for Newtonian fluids and asymptotic theory are provided in a recent publication by Divvela, *et al*. [27]

The initial jet thinning behavior predicted by the discretized modeling with the FENE-P model is compared with experimental observations in Figure 6.9. It is shown that the modeling prediction of the jet thinning is generally in good agreement with experimental observations, and can correctly predict faster initial thinning for more viscoelastic fluids (higher *De*). The discretized simulation shows better prediction for higher angular velocities. The effect of flow rate on initial

thinning is compared in Figure 6.10. Although there is a good agreement between simulation and experiments for the initial thinning behavior, the simulation predicts faster initial thinning compared to the experimental results especially at the high flow rate of 15 mL/min.
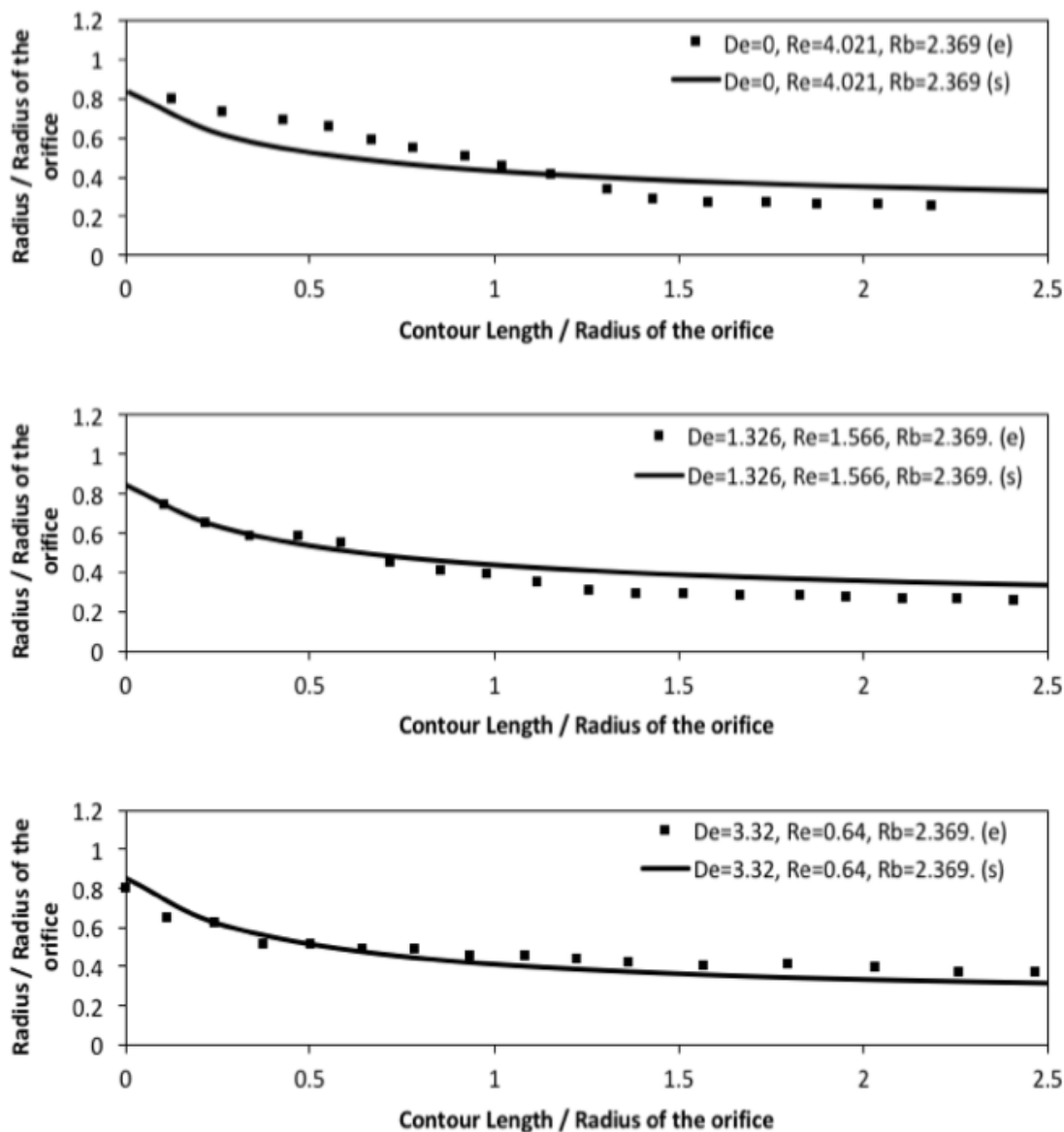


Figure 6.9. Comparison between the simulation prediction with the FENE-P model ("s") and experiments ("e") for the initial thinning of test fluids during centrifugal spinning (2140 RPM, 12.5 mL/min) at different concentrations a) Newtonian b) 2000 ppm c) 8000 ppm. $b_{max}$ = 20 and 80 in the FENE-P model were used for 2000ppm and 8000 ppm fluids.
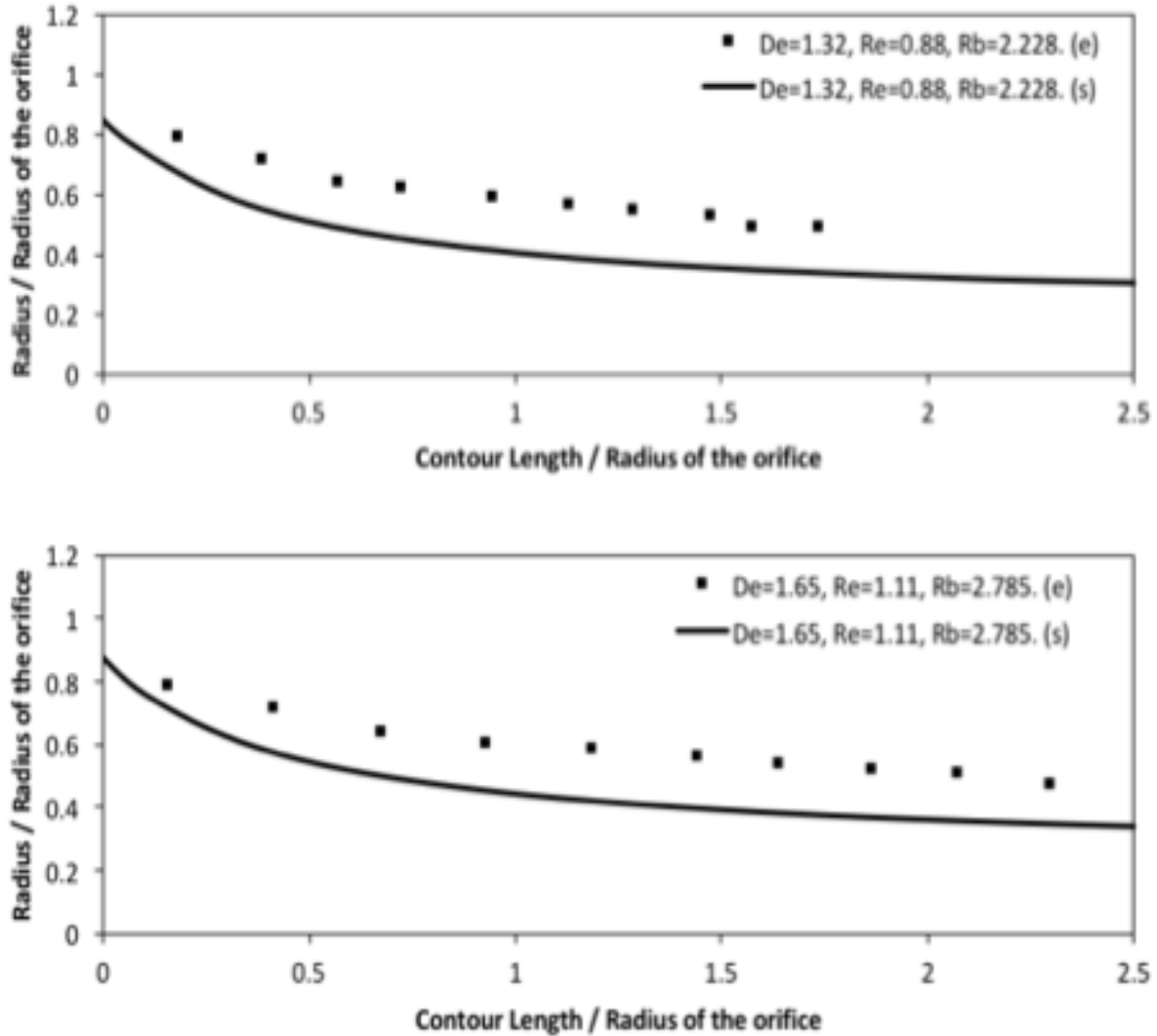
Figure 6.10. Comparison between the simulation prediction with the FENE-P model ("s") and experiments ("e") for the effect of the flow rate on the initial thinning of 4000ppm Boger fluid at 1820 RPM at flowrates a) 10 ml/min b) 12.5 ml/min $b_{max} = 40$ in the FENE-P model was used for the 4000 ppm fluid.

The effect of viscoelasticity on the evoltuion of the contour radius predicted by the discretized modeling is depicted in Figure 6.11. As shown in the Figure 6.11, increasing the viscoelasticity leads to smaller contour radius due to the increase in the hoop stress, which qualitatively matches the experimental observations discussed in the previous section. Although

we can see that the contour profiles are similar for both simulation and experimental observations in Figure 6.12, by using FENE-P model for viscoelastic stress, the simulation correctly predicts the contour profile even for highly viscoelastic polymer. From the same Figure 6.13, it can be seen that increasing the flow rate for the same rotation speed results in bigger contour radius down the stream, but the initial contours almost match. This prediction is similar to experimental observation as seen from Figure 6.14.
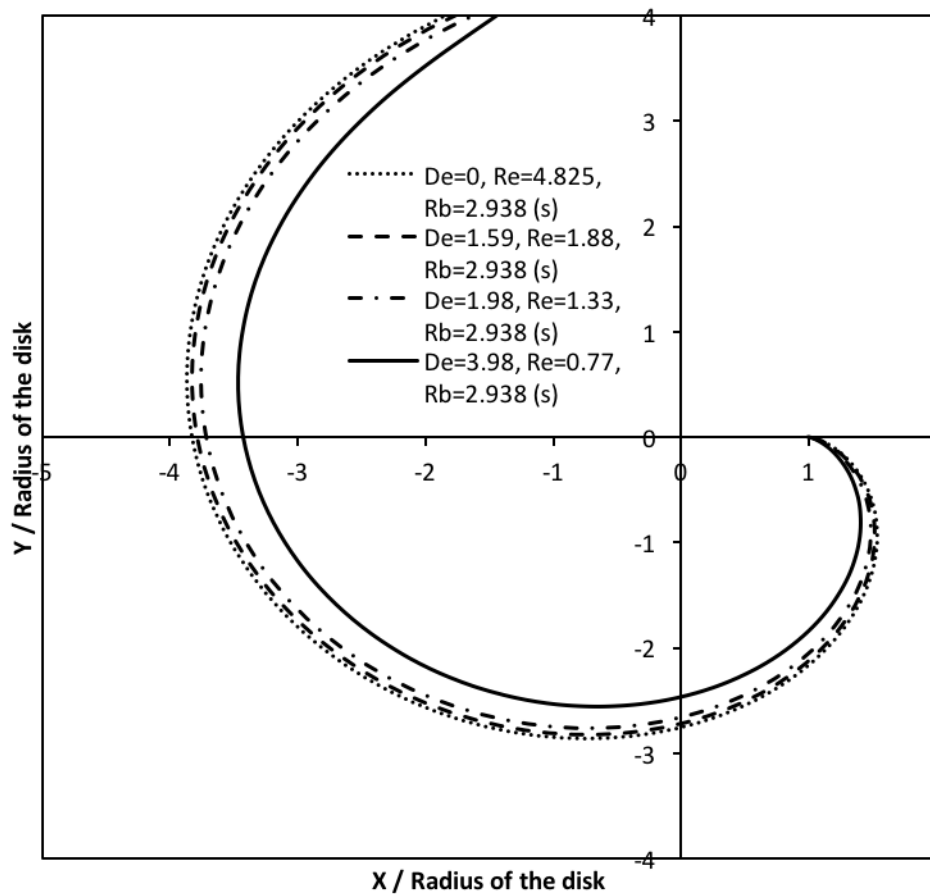


Figure 6.11. Simulation prediction with the FENE-P model ("s") of a) the effect of viscoelasticity on the contour radii during centrifugal spinning at 2070 RPM and 15 mL/min. $b_{max}$ = 20, 40, and 80 in the FENE-P model were used for 2000 ppm, 4000 ppm and 8000 ppm fluids, respectively.
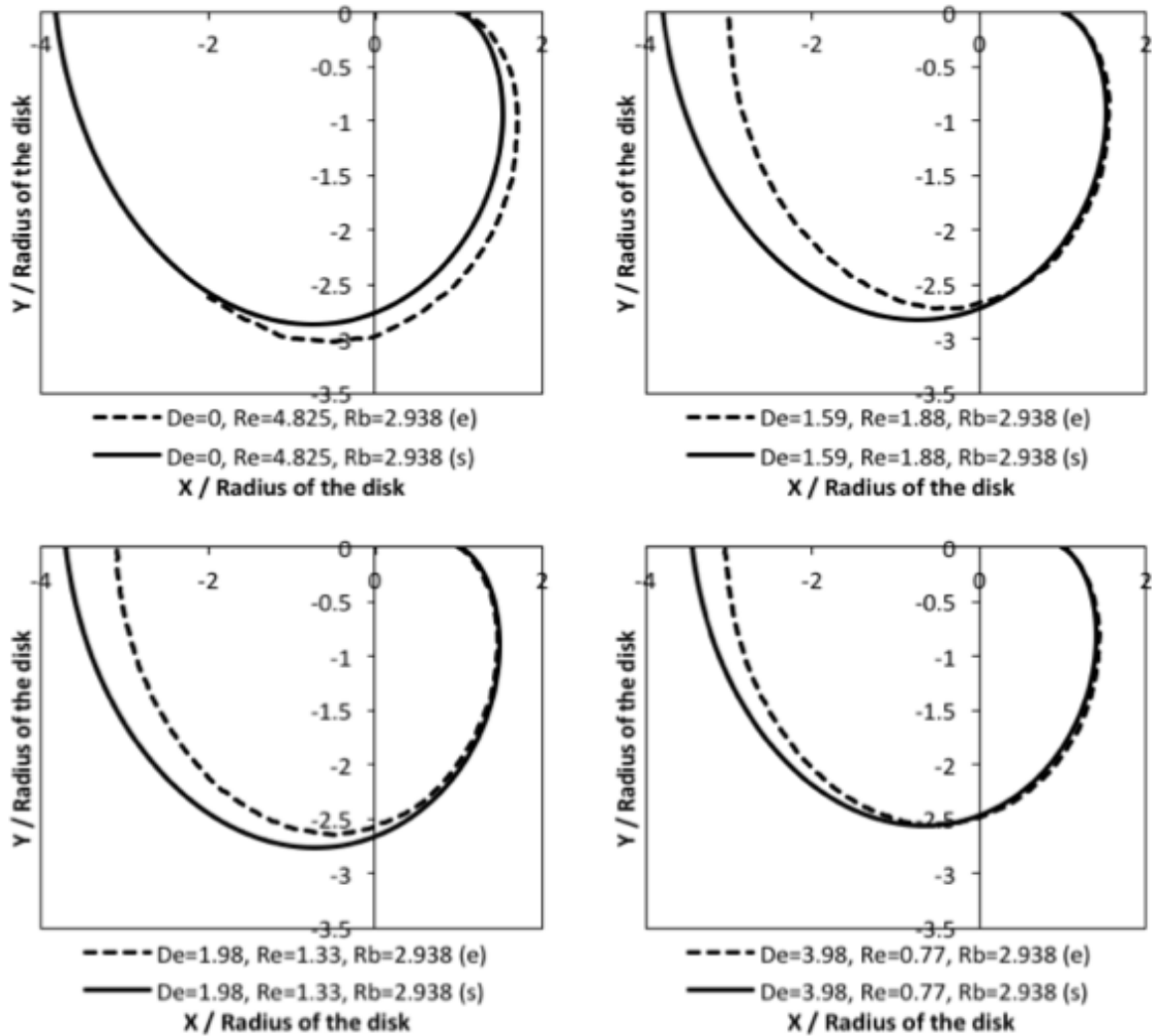
Figure 6.12. Comparison between the simulation prediction with the FENE-P model ("s") and experiments ("e") the effect of viscoelasticity on contour radii at 2070 RPM, 15 mL/min and concentrations at a) Newtonian b) 2000 ppm c) 4000 ppm and d) 8000 ppm.
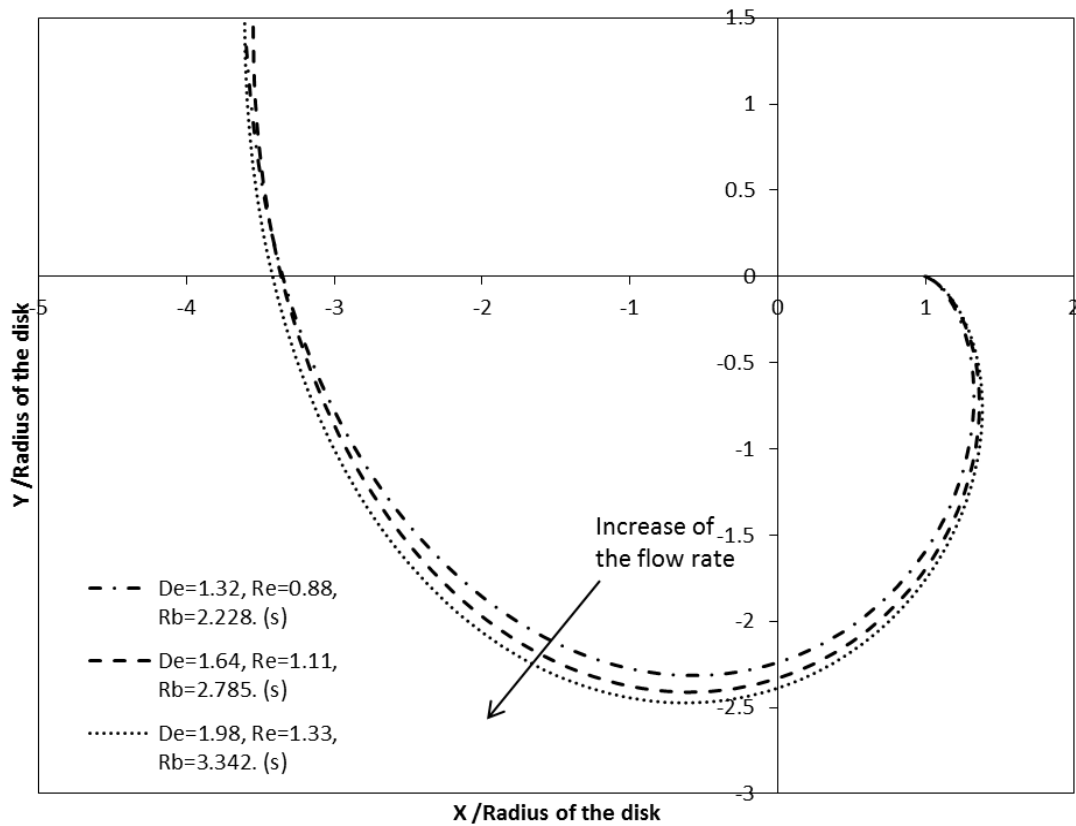
Figure 6.13. Simulation prediction ("s") of the effect of the flow rate during centrifugal spinning of 4000ppm Boger fluid at 1820 RPM.
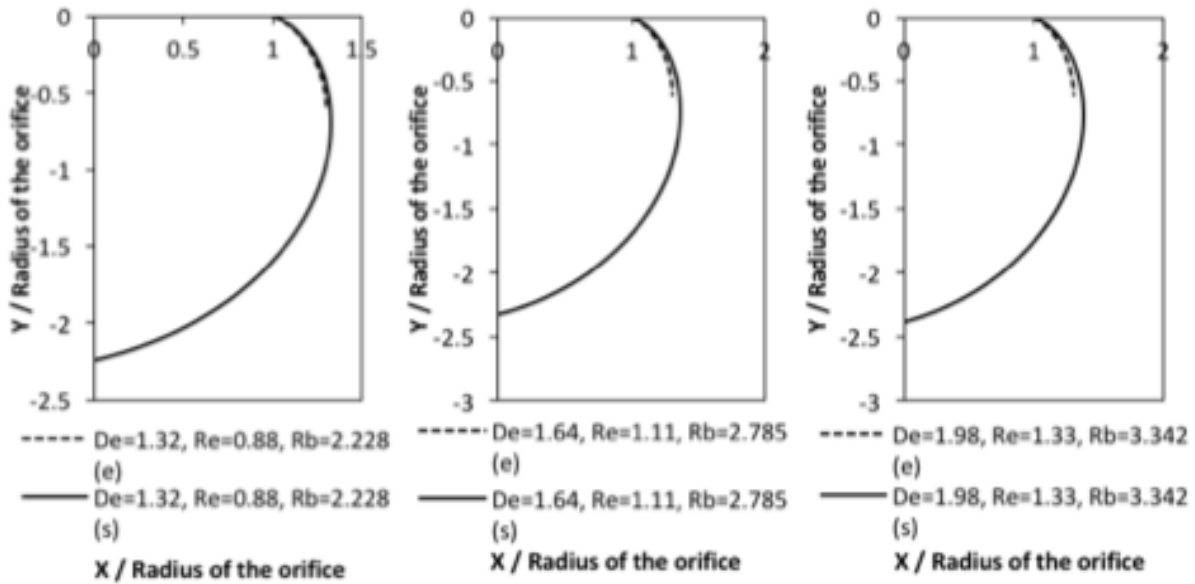
Figure 6.14. Comparison between the simulation prediction ("s") and experiments ("e") the effect of the flow rate during centrifugal spinning of 4000ppm Boger fluid at 1820 RPM for flowrates a) 10 ml/min b) 12.5 ml/min c) 15 ml/min.

Finally, the effect of the centrifugal force on the contour radius of the viscoelastic jet is illustrated in Figure 6.15, 6.17 and 6.19. From Figure 6.16, 6.18 and 6.20 it is seen that simulations also capture the same trends as observed experimentally for the effect of the rotation speed on contour radii. A slight variation in simulation and experiments is observed for the contour profiles, this may be due to variation in the rotational speed of the disk. The amount of the polymer on the disk is not always constant and due this small fluctuation in the weight on the disk it is difficult to maintain constant rotational speed. The jet travels closer to the spinneret for higher rotation speeds, in a certain range of angular velocities, as a result of strain hardening and the development of the hoop stress. Although for 2000 ppm polymer solution, the simulation is not sensitive in the initial region, it correctly captures the effect down the stream as shown in Figure 6.15. For higher viscoelastic jets, the effect of rotation speed and thus centrifugal force is more evident (see Figure

6.17 and 6.19). When the predicted contour radius is compared to experiments for three different Boger fluids, it is observed that the simulation underpredicts the curvature of the contour radius for the 2000 ppm Boger fluid, and the difference becomes smaller for the 4000 ppm Boger fluid, and evalually overpredicts the contour radius for the 8000 ppm Boger fluid especially at high rotation speeds.
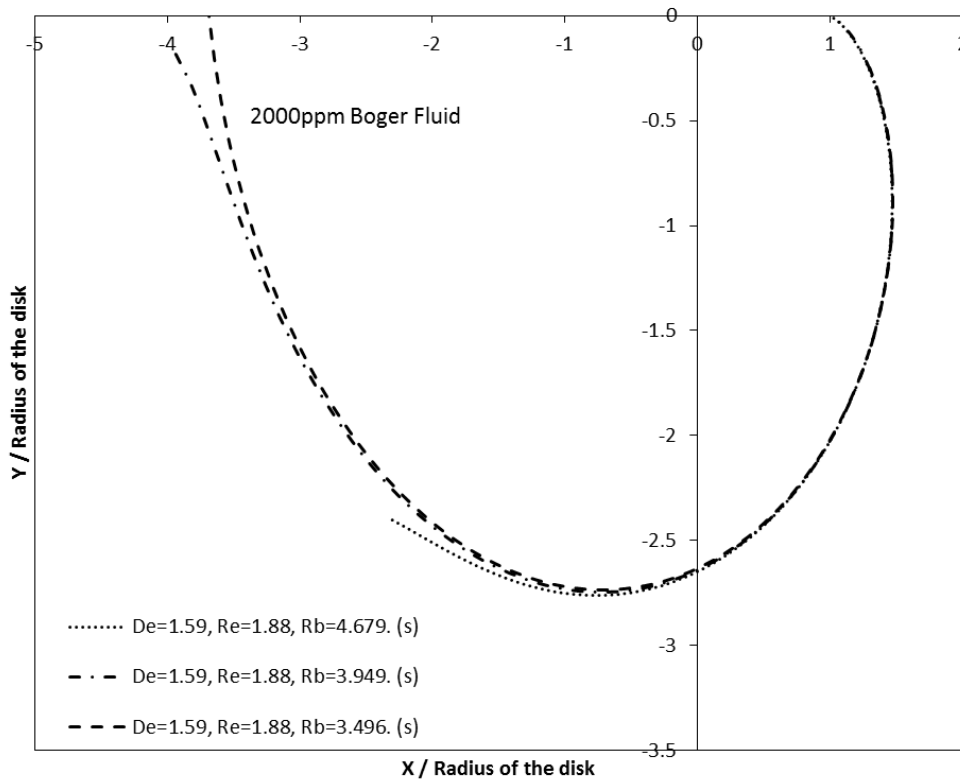


Figure 6.15. Simulation prediction ("s") of the effect of rotation speed on the contour radii during the centrifugal spinning of 2000ppm Boger fluid.
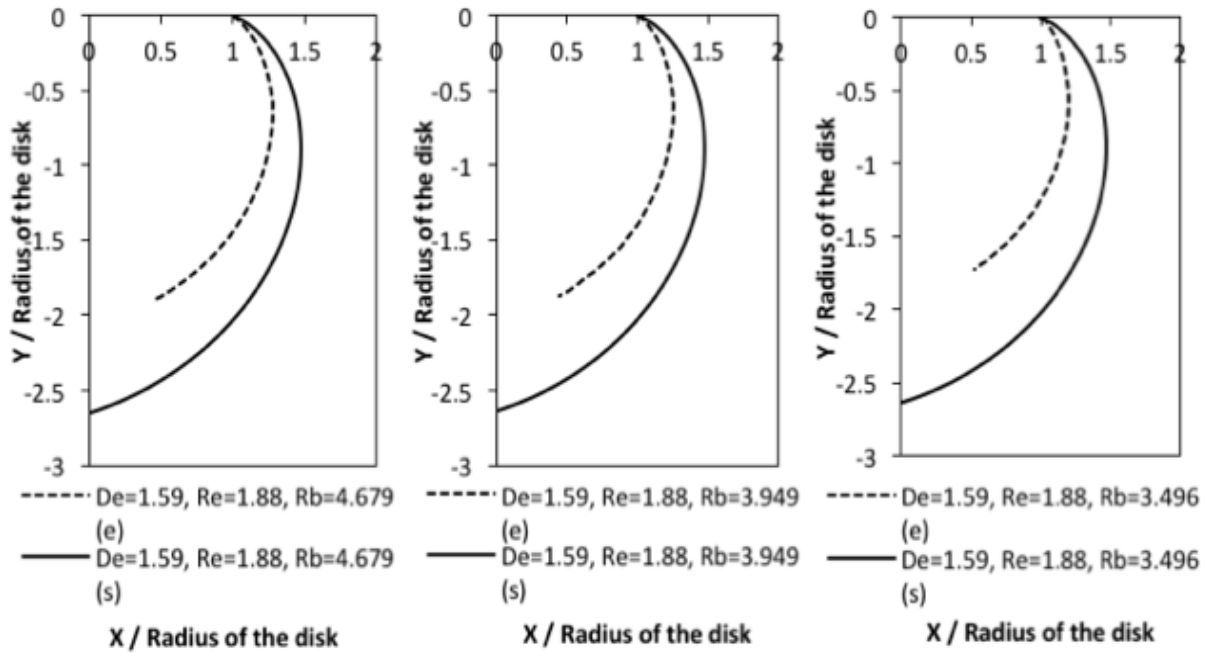
Figure 6.16. Comparison between the simulation prediction ("s") and experiments ("e") the effect of rotation speed on the contour radii on 2000 ppm Boger fluid at a) 1300 RPM b) 1540 RPM c) 1740 RPM.
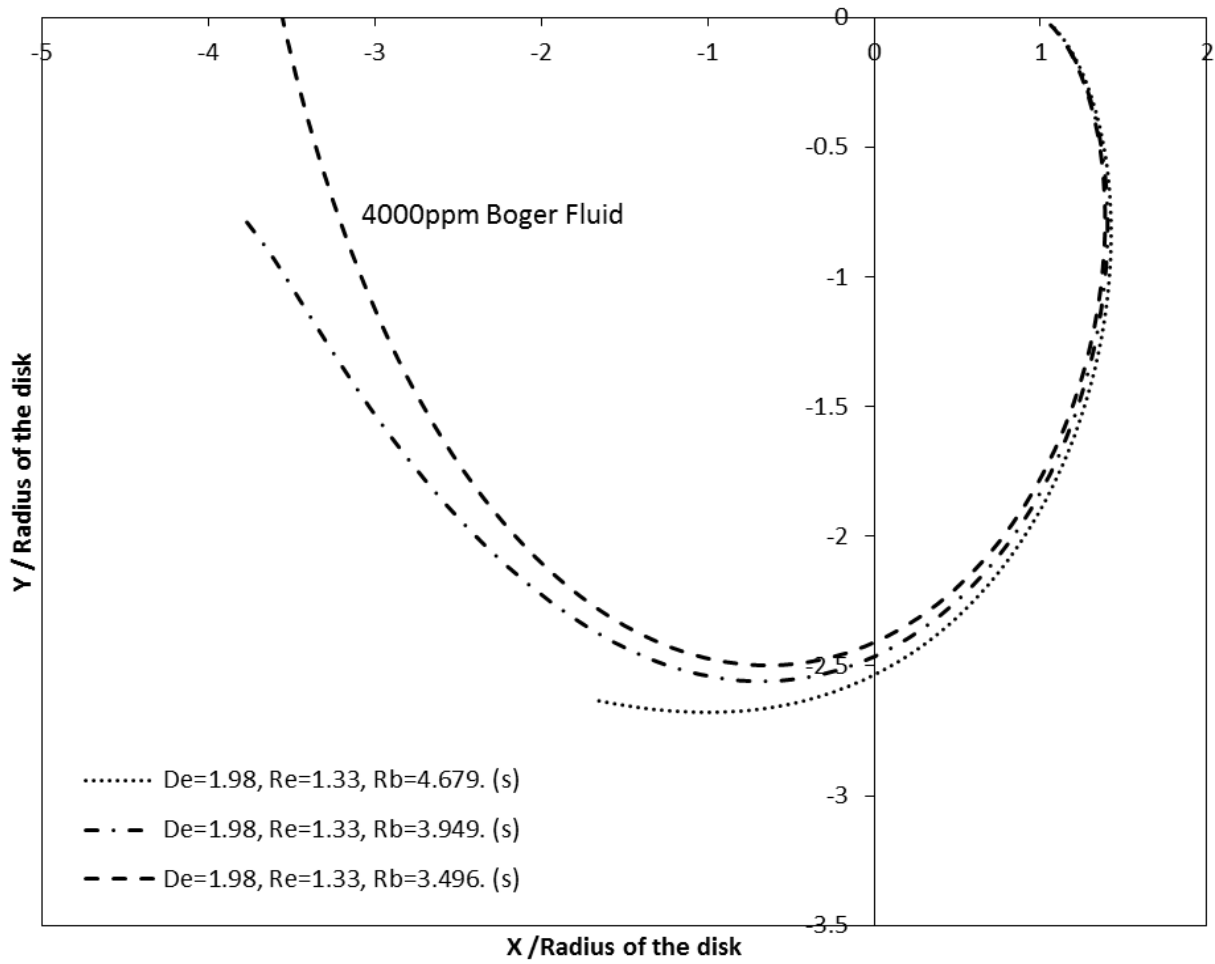
Figure 6.17. Simulation prediction ("s") of the effect of rotation speed on the contour radii during the centrifugal spinning of 4000ppm Boger fluid.
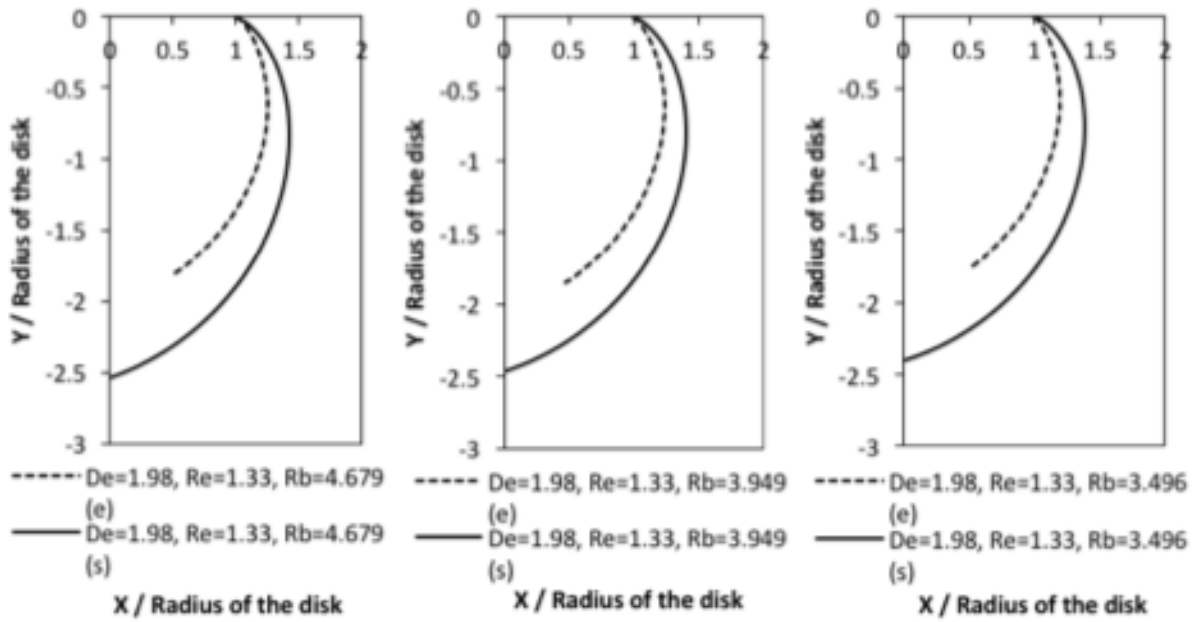
Figure 6.18. Comparison between the simulation prediction ("s") and experiments ("e") the effect of rotation speed on the contour radii on 4000 ppm Boger fluid at a) 1300 RPM b) 1540 RPM c) 1740 RPM.
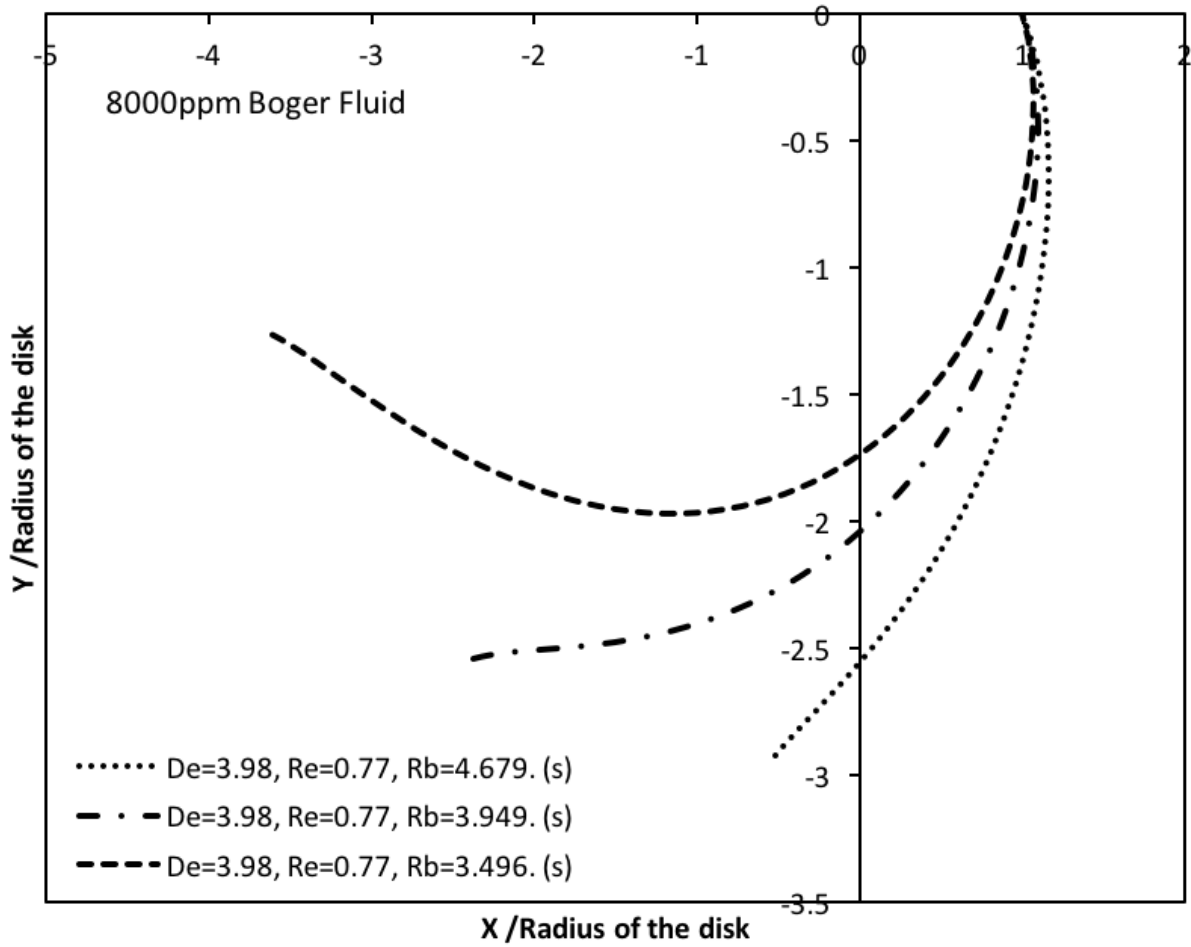
Figure 6.19. Simulation prediction ("s") of the effect of rotation speed on the contour radii during the centrifugal spinning of 8000ppm Boger fluid.
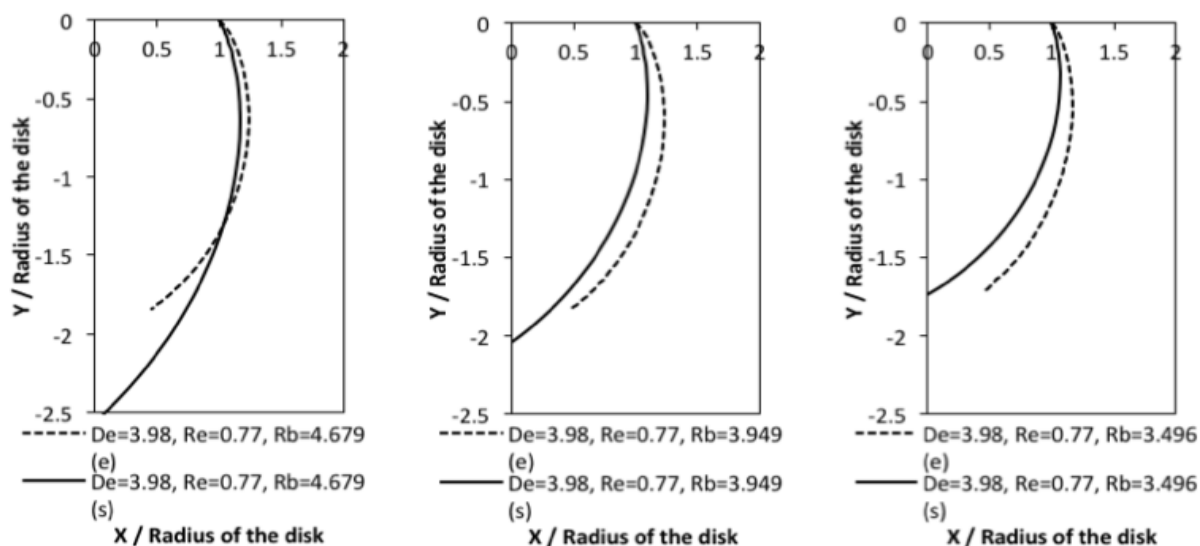
Figure 6.20. Comparison between the simulation prediction ("s") and experiments ("e") the effect of rotation speed on the contour radii on 8000 ppm Boger fluid at a) 1300 RPM b) 1540 RPM c) 1740 RPM.

## 6.5. Qualitative Comparison with Electrospinning

Electrospinning is a process for producing nanofibers, where an electric field of high voltage is applied to draw a polymer jet. A polymer solution or melt is pumped through the needle into the electric field, where the spinning occurs. There are typically two stages, the first is the acceleration of the jet in a straight line, and the second is the region of bending instability (often referred to as a "whipping motion"). The fibers are collected on the grounded collector plate in a form of non-woven mat. [2–7, 16, 19, 21, 22] Electrospinning experiments were reproduced for the same PIB/PB Boger fluid system in the literature, [10] but slightly different experimental conditions were used in some cases. The analysis procedure and the instruments were the same as for centrifugal spinning.

Due to a difference in the magnitude and nature of driving forces for two processes, it is possible to provide only a qualitative comparison of the effects of the viscoelasticity, driving force

171

and the flow rate. While electrospinning is driven by electrostatic force, centrifugal spinning is driven by a convoluted combination of centrifugal and Coriolis forces with a significant effect of air drag.

From Figure 6.21 it can be seen that the effects of the viscoelasticity, flow rate and driving force on the initial jetting behavior are qualitatively almost the same for electrospinning as they were shown for centrifugal spinning. The main difference is the effect of the driving force on the initial thinning behavior. While the retarded thinning was observed with increasing the driving force, *i.e.* rotation speed, in the centrifugal spinning process of highly viscoelastic Boger Fluids (see Figure 6.7), the initial thinning increased with increasing the driving force (applied voltage, and thus electric field) in electrospinning experiments (see Figure 6.21 (b)). This may be attributed to a larger magnitude of the compressive force involved in electrically charged jet, whereas the hoop stress develops much faster in centrifugal spinning process due to the development of the contour with curvature from the nozzle exit.
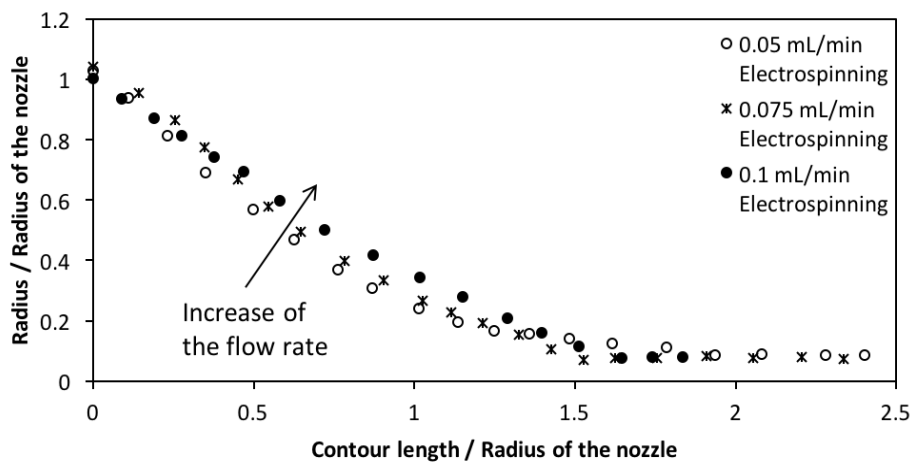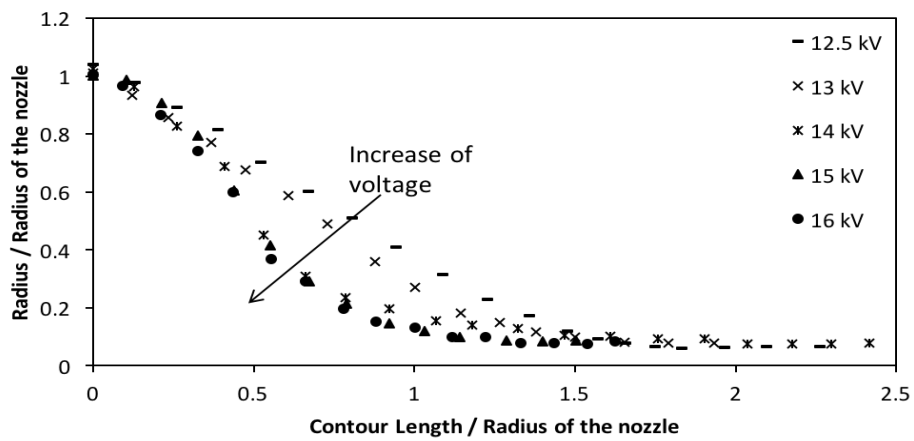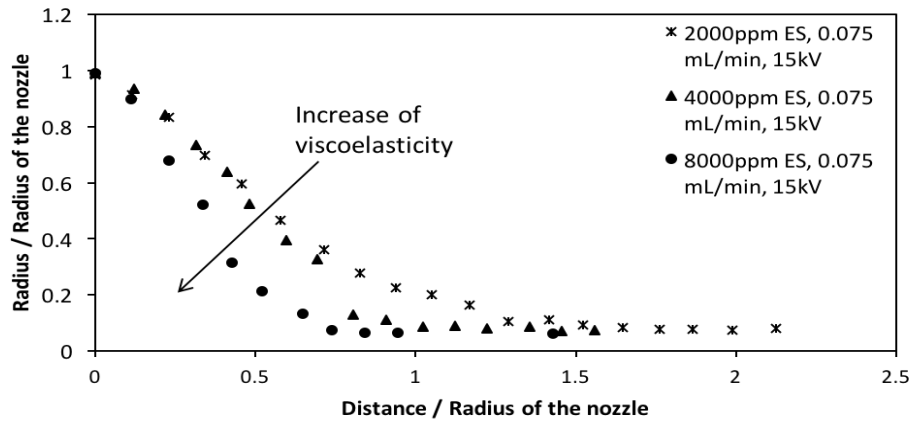
Figure 6.21. The effect of viscoelasticity, driving force and flow rate on the initial thinning during electrospinning of viscoelastic Boger fluids (from top to bottom respectively).

## 6.6. Summary

We have demonstrated that viscoelasticity, flow rate and rotation speed have significant effects on the initial jet thinning and contour profiles during the centrifugal spinning process. The polymer jet tends to thin faster for more viscoelastic fluid in the initial region and the significant hoop stress results in a smaller contour radius. The increase in the rotation speed will lead to faster strain hardening for more viscoelastic fluids, which hinders thinning. However, for Newtonian and low viscoelasticity cases the initial thinning was observed to be faster for higher angular velocities. The increase of the rotation speed in a certain range will reduce the contour radius for viscoelastic fluids due to a drastic increase of the hoop stress. Experimental results are generally in good agreement with the discretized simulation, however, some refining is required. The initial thinning behavior is generally in a good qualitative agreement for both electrospinning and centrifugal spinning, which allows to use the same reasoning for two processes. These results will be used as a basis for the experimental and theoretical analysis of more concentrated polymer solutions and polymer melts in future centrifugal spinning studies.

# REFERENCES

[1]   A. Ziabicki, "Fundamentals of Fibre Formation: The Science of Fiber Spinning and Drawing," *New York Wiley*, 1976.

[2]   E. Zhmayev, D. Cho, and Y. L. Joo, "Nanofibers from gas-assisted polymer melt electrospinning," *Polymer*, vol. 51, no. 18, pp. 4140–4144, Aug. 2010.

[3]   A. Formhals, "US Patent 1-975-504." 1934.

[4]   A. E. Spivak, Y. A. I. Dzenis, and D. H. Reneker, "A model of steady state jet in the electrospinning process," *Mech. Res. Commun.*, vol. 27, no. 1, pp. 37–42, 2000.

[5]   M. M. Hohman, M. Shin, G. Rutledge, and M. P. Brenner, "Electrospinning and electrically forced jets. I. Stability theory," *Phys. Fluids*, vol. 13, no. 8, p. 2201, 2001.

[6]   M. M. Hohman, M. Shin, G. Rutledge, and M. P. Brenner, "Electrospinning and electrically forced jets. II. Applications," *Phys. Fluids*, vol. 13, no. 8, p. 2221, 2001.

[7]   J. J. Feng, "The stretching of an electrified non-Newtonian jet: A model for electrospinning," *Phys. Fluids*, vol. 14, no. 11, p. 3912, 2002.

[8]   S. Padron, A. Fuentes, D. Caruntu, and K. Lozano, "Experimental study of nanofiber production through forcespinning Experimental study of nanofiber production through forcespinning," *J. Appl. Phys.*, vol. 24318, 2013.

[9]   D. Edmondson, A. Cooper, S. Jana, D. Wood, and M. Zhang, "Centrifugal electrospinning of highly aligned polymer nanofibers over a large area," *J. Mater. Chem.*, vol. 22, no. 35, p. 18646, 2012.

[10]  M. R. Badrossamay, H. A. McIlwee, J. a Goss, and K. K. Parker, "Nanofiber assembly by rotary jet-spinning.," *Nano Lett.*, vol. 10, no. 6, pp. 2257–61, Jun. 2010.

[11]   A. Arinstein, M. Burman, O. Gendelman, and E. Zussman, "Effect of supramolecular structure on polymer nanofibre elasticity.," *Nat. Nanotechnol.*, vol. 2, no. 1, pp. 59–62, Jan. 2007.

[12]   S. Mitragotri and J. Lahann, "Physical approaches to biomaterial design.," *Nat. Mater.*, vol. 8, no. 1, pp. 15–23, Jan. 2009.

[13]   V. Thavasi, G. Singh, and S. Ramakrishna, "Electrospun nanofibers in energy and environmental applications," *Energy Environ. Sci.*, vol. 1, no. 2, p. 205, 2008.

[14]   J. Yu, R. Feng, and W. She, "Low-power all-optical switch based on the bend effect of a nm fiber taper driven by outgoing light.," *Opt. Express*, vol. 17, no. 6, pp. 4640–5, Mar. 2009.

[15]   Y. M. Shin, M. M. Hohman, M. P. Brenner, and G. C. Rutledge, "Experimental characterization of electrospinning: the electrically forced jet and instabilities," *Polymer*, vol. 42, no. 25, pp. 09955–09967, Dec. 2001.

[16]   C. P. Carroll and Y. L. Joo, "Electrospinning of viscoelastic Boger fluids: Modeling and experiments," *Phys. Fluids*, vol. 18, no. 5, p. 53102, 2006.

[17]   D. H. Reneker, A. L. Yarin, H. Fong, and S. Koombhongse, "Bending instability of electrically charged liquid jets of polymer solutions in electrospinning," *J. Appl. Phys.*, vol. 87, no. 9, p. 4531, 2000.

[18]   A. L. Yarin, S. Koombhongse, and D. H. Reneker, "Bending instability in electrospinning of nanofibers," *J. Appl. Phys.*, vol. 89, no. 5, p. 3018, 2001.

[19]   E. Zhmayev, D. Cho, and Y. L. Joo, "Modeling of melt electrospinning for semi-crystalline polymers," *Polymer*, vol. 51, no. 1, pp. 274–290, Jan. 2010.

[20]    E. Zhmayev, D. Cho, and Y. Lak Joo, "Electrohydrodynamic quenching in polymer melt electrospinning," *Phys. Fluids*, vol. 23, no. 7, p. 73102, 2011.

[21]    C. P. Carroll and Y. L. Joo, "Axisymmetric instabilities of electrically driven viscoelastic jets," *J. Nonnewton. Fluid Mech.*, vol. 153, no. 2–3, pp. 130–148, Aug. 2008.

[22]    C. P. Carroll and Y. L. Joo, "Discretized modeling of electrically driven viscoelastic jets in the initial stage of electrospinning," *J. Appl. Phys.*, vol. 109, no. 9, p. 94315, 2011.

[23]    Y. L. Joo and E. S. G. Shaqfeh, "Observations of purely elastic instabilities in the Taylor-Dean flow of a Boger fluid," *J. Fluid Mech.*, vol. 262, no. 1923, 1994.

[24]    G. Prilutski, R. K. Gupta, T. Sridhar, and M. E. Ryan, "Model Viscoelastic Liquids," *J. Nonnewton. Fluid Mech.*, vol. 12, pp. 233–241, 1983.

[25]    D. F. James, "Boger Fluids," *Annu. Rev. Fluid Mech.*, vol. 41, no. 1, pp. 129–142, Jan. 2009.

[26]    M. E. Mackay and D. V Boger, "An explanation of the rheological properties of Boger Fluids," *J. Nonnewton. Fluid Mech.*, vol. 22, pp. 235–243, 1987.

[27]    A. C. Ruo, Y. Zhmayev, and Y. Lak, "Discretized Modeling for Jetting Behavior during Centrifugal Spinning," pp. 1–25.

[28]    E. Zhmayev, H. Zhou, and Y. L. Joo, "Modeling of non-isothermal polymer jets in melt electrospinning," *J. Nonnewton. Fluid Mech.*, vol. 153, no. 2–3, pp. 95–108, Aug. 2008.

[29]    I. M. Wallwork, S. P. Decent, A. C. King, and R. M. S. M. Schulkes, "The trajectory and stability of a spiralling liquid jet. Part 1. Inviscid theory," *J. Fluid Mech.*, vol. 459, pp. 43–65, 2002.

[30]    J. Uddin, S. P. Decent, and M. J. H. Simmons, "Non-linear waves along a rotating non-

Newtonian liquid jet," *Int. J. Eng. Sci.*, vol. 46, no. 12, pp. 1253–1265, Dec. 2008.

[31]   S. P. Decent,  a. C. King, M. J. H. Simmons, E. I. Părău, I. M. Wallwork, C. J. Gurney, and J. Uddin, "The trajectory and stability of a spiralling liquid jet: Viscous theory," *Appl. Math. Model.*, vol. 33, no. 12, pp. 4283–4302, Dec. 2009.

[32]   S. Panda, N. Marheineke, and R. Wegener, "Systematic derivation of an asymptotic model for the dynamics of curved viscous fibers," *Math. Methods Appl. Sci.*, no. November 2006, pp. 1153–1173, 2008.

[33]   N. Marheineke and R. Wegener, "Asymptotic model for the dynamics of curved viscous fibres with surface tension," *J. Fluid Mech.*, vol. 622, p. 345, Feb. 2009.

[34]   T. Gotz, A. Klar, and A. Unterreiter, "Numerical evidence for the non-existence of stationary solutions of the equations describing rotational fiber spinning ∗," *Math. Model. Methods Appl. Sci.*, vol. 18, no. 10, pp. 1829–1844, 2008.

[35] M.R.J. Verhoef, B.H.A.A. van den Brule, M.A. Hulsen, *J. Non-Newtonian Fluid Mech.* vol. 80**,** pp. 155, 1999.

# CHAPTER 7

# FUTURE WORK

## 7.1 Gas-assisted Electrospinning

A new fiber spinning process that utilizes both high electric field and controlled air flow employed circumferentially through the sheath layer of the concentric coaxial nozzle, referred to as gas-assisted electrospinning, has been utilized to upscale the production and to tailor the distribution of various nanofillers in a polyvinyl alcohol jet. As the novel electrospinning procedure develops, it is useful to perform a rigorous empirical visualization study to determine the effect of the key environmental and experimental conditions on the emanation, bending instability and collection of the polymer jet. The precise control of these three regimes determines morphological, topological and inner/outer-dispersion characteristics of the resulting nanofiber.

The driving force effect is essential, especially for the nanofiller dispersion control. It would be useful to visually examine the interaction between the electric potential and different air flow rates, since the conjunction of two is a complex driving force that is essential for all stages of the spinning process. The precise understanding can be achieved by deconvolution, looking at the effects associated with 1) the gas stream, such as the flow rate, humidity, temperature, and gas composition, and 2) electric field, such as potential difference, electric current (AC or DC) and electric field distortions, separately.

Additional attention may be directed to the shape and geometry of the nozzle, since changing the exit area to aerodynamically clean shapes may result in further air-drag reduction, jet acceleration and control of solvent evaporation. It is also possible to perform a macro-visualization of the vortex flow in the Taylor cone region, to further study the effect of additional air stream on

nanoparticle agglomerate rupture. The experimental procedure is tedious, but can be performed via inclusion of various tracer particles in polymer solutions and further high-speed camera recording. The study should focus on the effect of experimental and rheological characteristics, which may require the use of different polymers, *i.e.* polyvinylidene fluoride, polyacrylonitrile or cellulose acetate.

The ability to control the dispersion of spherical ($SiO_2$ and Si) and anisotropic (CNT and GNR) nanoparticles is demonstrated in Chapter 2 and Chapter 3, respectively, by varying airflow rates in GAES. The spatial distribution is measured from transmission electron microscopy and is analyzed using an image processing technique to perform the dispersion area analysis, to obtain the most probable separation between nanoparticles using fast Fourier transform, and to determine the orientation relative to the flow axis utilizing alignment analysis. Further investigation is needed to measure and control the dispersion of different geometries of functional nanoinclusions, such as 2-D sheets of graphene oxide, that received a lot of attention in Li-ion battery applications. It is important to investigate the in-fiber folding behavior, the effect of the sheet size and loading, as well as the spatial distribution and orientation of 2-D nanoparticles, as a response to additional extensional deformation supplied by the sheath layer air flow. It is also desirable to measure the dispersion of polydisperse particle systems and multi-component particle systems. The later will address the experimental verification of theoretical predictions that conclude the possibility of a spherical inorganic particle acting as a dispersant to its anisotropic counterpart, homogenizing the polymer-NP system solely via effective enthalpic interactions between the two.

The experiments in this study are in good agreement with a coarse-grained MD simulation prediction for a polymer nanocomposite system subjected to extensional deformation. The theoretical investigation can be extended to the DEM simulation to account for the sheath-layer

air flow in gas-assisted electrospinning process. Further modifications should be done by revising the components associated with the force due to the air drag, and the mass transport due to solvent evaporation. These adjustments will enable a more accurate prediction of the in-flight jet path elongation as well as instability behaviors, and a rigorous comparison with experimental observations will produce a robust predictive tool.

Utilizing the sheath layer air flow in production of Li-battery anode material, we delivered a 680 mAh $g^{-1}$ capacity improvement, which is associated with better dispersion of electrochemically active nanoparticles. In Chapter 2, we proposed a use of Si nanoparticles as an active material, and CNTs to increase the electronic conductivity in PVA matrix. Future directions involve the utilization of different geometries of carbon nanoinclusions, and the effect of enhanced dispersion on their electrochemical performance.

The new gas-assisted electrospinning process has shown a great potential in controlling the dispersion and spatial orientation of various nanofillers in polymer jets, as well as addressed the industrial challenge for the high productivity. It has also introduced new potential applications that have been partially addressed in this thesis. There are many ongoing projects in our research group, that aim to undertake some of the proposed future directions, which may require dedicated attention of several Ph.D. students.

## 7.2 Air-controlled Electrospray

A novel spraying technique has been proposed to precisely control the morphological and topological characteristics of polymer coatings at nanoscale, by applying a controlled sheath layer air flow through a coaxial spinneret during air-controlled electrospraying. The new methodology provides a facile way to control the atomization behavior, by triggering bending instability due to

additional Taylor cone thinning, polymeric jet acceleration and air drag reduction, which was not previously observed in conventional electrospray methods. This additional detail allows to decrease and homogenize the average droplet size diameter, which promotes the uniformity and efficiency of polymer coating deposition. Further experimental visualization agenda can be inherited from gas-assisted electrospinning, and should be carried out to study the effect of experimental parameters on the fluid atomization and deposition. The focus of the future study may be on the effect of additional air flow and the interplay between viscoelasticity, surface tension and the driving force, which are the components that tailor the atomization mechanism, and their control is essential for instability driven processes. The effect of viscoelasticity can be effectively investigated by changing the fluid composition, exploring a wide range of polymers and concentrations, and it is expected that the droplet dimensions can be further decreased by increasing the relaxation time.

Furthermore, to alleviate scalability constraints and smoothen coating irregularities due to the surface charge build-up on the substrate during the DC electrospray, we developed the alternating current air-controlled ($AC^2$) electrospray process. Very little is known about the AC-induced instabilities in spinning and spraying processes, and our study is an ideal frame-work for the investigation of this phenomena. By changing the electric potential, frequency and the waveform, we can gain further insight into the more effective charge accumulation on the fluid surface in the Taylor cone region (multi-jet mode), improve efficiency, and achieve additional control of fluid atomization.

The proposed empirical visualization study is beneficial for the validation of our novel DEM simulation procedure, which must be modified to account for the sheath layer air flow, alternating current and additional atomization effect due to Coulomb fission. There may be a need

to implement several fitting parameters to generate a reliable predictive tool, which may be provided independently by carefully designed experiments. This could be a challenging, but extremely inspiring high-impact project.

Our results, presented in Chapter 4, demonstrate that with the increase of the air flow in air-controlled electrospray, there is a significant improvement in spatial distribution of spherical (carbon black) and anisotropic (CNT) nanoparticles in deposited PVA coatings. It is suggested that the enhancement is due to a synergistic effect of the droplet size reduction, and strain-induced agglomerate rupture, that occurs when extensional forces overcome cohesive forces between particles in a vigorously bending polymer jet. This behavior can be utilized to control the functionality of resulting coatings, *i.e.* ultrahydrophobicity in transparent coatings, by uniformly dispersing nanoscale particles on the surface to create even topological irregularities; or electrochemical performance in electrode coatings, by homogenizing the active material. Future directions on the dispersion side would involve the utilization of different types and geometries of nanoinclusions, with a particular focus on 2-D graphene oxide structures, which can effectively envelope Si-based active material in Li-battery anodes, yielding superior performance.

Finally, the new air-controlled electrospray can be utilized to overcome scalability and control constraints in the mass-production of micron/nano-scale capsules. It has been shown in Chapter 5, that capsule dimensions and morphologies can be precisely controlled by tuning the air flow rate, in addition to conventional electrospraying parameters, as well as increasing the throughput 10-fold. This discovery opens a lot of opportunities for further investigation of the encapsulation effectiveness, which may be carried out by changing various experimental conditions, as well as solution compositions, and can be validated by a rigorous confocal microscopy study. By incorporating a gelation bath as a collector in electrospraying setup, it would

be possible to create different shapes of capsules, *i.e.* donut, teardrop, jellyfish, cap, which has a high demand in bioencapsulation. We also demonstrated an industrial potential of the encapsulation technique by fabricating stress-indicating patches, which provide a clear mechanochromic response to compressive deformation. In the next stage of this project, different substrates should be tested to ensure a more homogeneous response to deformation, and the novel encapsulation procedure will be implemented in the injection-molding scheme for a single-step manufacturing of the stress-indicating polymer composites.

The development and investigation of AC and $AC^2$ electrospray processes undeniably deserve more attention in energy storage and encapsulation applications. Therefore, we have proposed a number of future avenues of research, which should result in significant results.


**7.3 Centrifugal spinning**

We have concluded that to ensure the viability for industrial utilization, manufacturing processes must be adequately scaled-up. Therefore, in Chapter 6 of this thesis we present an experimental visualization study of centrifugal spinning, which is a novel process for producing nanoscale or submicron fibers, where the centrifugal force is utilized to elongate and accelerate a fluid jet, and the production rate can be increased by three orders of magnitude compared to conventional techniques. The investigation was conducted using Newtonian and viscoelastic fluids to study the effect of viscoelasticity, driving force and the flow rate on the initial thinning behavior, jet contour shapes and radii. Boger fluids based on Newtonian polybutene (PB) and viscoelastic polyisobutylene (PIB) were utilized as test fluids in the current study, to eliminate the complexities associated with shear thinning and mass transport due to solvent evaporation. Future directions on this project would involve an extension of previous experiments to shear-thinning solutions with

volatile solvents, to further investigate the effect of viscoelasticity, mass transport and non-isothermal nature of the system, which would more realistically address real applications.

The fiber collection in the novel process does not require a collector, and can be further optimized by utilizing the controlled stream of air from the top, which will direct solidified fibers to the bottom of the setup, creating a uniform nonwoven mat. This can be beneficial for all the applications where a uniform deposition on the substrate is required. Further modification of the disk-shaped spinneret may be done to utilize a sheath layer air flow, which may further scale-up the production and provide additional control of aerodynamically-driven bending instability. These modifications open future avenues for the incorporation of various functional nanoinclusions with the precise control of their dispersion in highly-aligned polymer fibers, as well as potential utilization of centrifugal force in spraying methods.

The comparison of experiments with the discretized element modeling with the FENE-P model confirms the model predictive potential for the jet thinning behavior. However, to take full advantage of the simulation, refinement must be done to account for mass transport in solvent-polymer systems, and non-isothermal nature for polymer melts.

Analogously to the previously discussed projects, this study revealed numerous potential research directions to efficiently manufacture various functional polymer nanocomposites with a precise control of their inherent material properties.